DETECTION AND QUANTIFICATION OF DELAMINATION IN CONCRETE VIA TIME-LAPSE THERMOGRAPHY WITH MACHINE LEARNING

A Dissertation

presented to

the Faculty of the Graduate School

at the University of Missouri-Columbia

In Partial Fulfillment

of the Requirements for the Degree

Doctor of Philosophy

---

by

Mohanned Al Gharawi

Dr. Glenn Washer, Dissertation Supervisor

Dr. Yaw Adu-Gyamfi, Dissertation Co-advisor

July 2021

The undersigned, appointed by the dean of the Graduate School, have examined the dissertation entitled

DETECTION AND QUANTIFICATION OF DELAMINATION IN CONCRETE VIA TIME-LAPSE THERMOGRAPHY WITH MACHINE LEARNING

presented by **Mohanned Al Gharawi,**

a candidate for the degree of **Doctor of Philosophy of Civil Engineering,**

and hereby certify that, in their opinion, it is worthy of acceptance.

Dr. Glenn Washer

Dr. Hani Salim

Dr. Yaw Adu-Gyamfi

Dr. Mahmoud Almasri

DEDICATION

This dissertation is proudly dedicated ……

To my Beloved Parents,

To my Wife Who Supports me all the Time,

To my Lovely Three Kids,

To my Sisters and Brothers,

To my all Friends,

Thanks for your Endless Love, Sacrifices, Prayers, Support and Guidance.

ACKNOWLEDGEMENTS

First, praise to Allah for giving me the strength to complete this work at the University of Missouri-Columbia.

I would like to express my deepest gratitude to my advisor, Dr. Glenn Washer, for his valuable guidance, encouragement, constructive suggestions, and his assistance throughout the final preparation of this work. I really appreciate him for granting me especially during the year of the pandemic. I would also like to thank my co-advisor Dr. Yaw Adu-Gyamfi for all his assistance, useful discussions and especially during the difficult stages of doing this study. I am truly grateful particularly throughout writing this dissertation. It was a great honor for me to work with my both supervisors; the work would not have been finished without their support.

Also, many thanks go to the rest of my committee members: Dr. Hani Salim and Dr. Mahmoud Almasri for their valuable feedback on the dissertation.

My sincere thanks to my friend Ahmed Qasim for his assistance in explaining to me the MATLAB software and developing some necessary MATLAB script for the analysis of IRT data.

Special thanks go to Toby Washer, Dr. Washer's son, who was a very helper in building the mold of the reinforced specimen. The experimental work would not be finished without his assistance. I am Also thankful for all who had helped me in finishing the work in the RTF, especially Aaron Suacier.

Special thanks go to my friends, Ahmed, Laith, Safa, Kamal, Ali, Mohammed, and Fahad, who participated in constructing the concrete specimen.

In the loving memory of my parents; especially to my mother who passed away last year. I just wished to make her see me when I graduate and feel proud of me. I wish they were here to share my happiness while writing these words.

I would like to thank my entire family, my sisters, my brothers, my nieces, and nephews for their support, prayers, and words of love during the difficult times that I had.

Finally, distinctive gratitude goes to my soulmate, my wife, Ruwayda Ahmed, who has been inspired and supported me during this journey. She has sacrificed and walked next to me throughout the entire way especially the last year, when the pandemic started and then later when my mother passed away.

Definitely, I would not be able to finish this work without her encouragement and support until the end. You have been always in my heart and will always be!

TABLE OF CONTENTS

LIST OF FIGURES

LIST OF TABLES

DETECTION AND QUANTIFICATION OF DELAMINATION IN CONCRETE VIA TIME-LAPSE THERMOGRAPHY WITH MACHINE LEARNING

Mohanned Al Gharawi

Dr. Glenn Washer, Dissertation Supervisor

Dr. Yaw Adu-Gyamfi, Dissertation Co-advisor

Abstract

This study developed a framework to automatically extract sub-surface defects from time-lapse thermography (TLT) images of reinforced concrete bridge components. Traditional approaches for processing TLT data typically require manual interventions that are not easily scaled to a large network of concrete bridges. A backbone of robust algorithms for detecting and analyzing deep sub-surface defects in concrete is needed to support condition assessment of concrete structures such as bridges. The current study leverages advances in adaptive signal and image processing to develop a fully automated TLT data processing pipeline that is capable of efficiently detecting defects at different depths in concrete. The methodology decomposes raw TLT datasets into narrow band time-frequency domains via a multiscale data analysis approach called a Wavelet Transform. The resulting decomposed modes are mined to extract defect information using thermal contrast enhancement routines. An objective measure of effectiveness based

on signal-to-noise ratio was developed and used to compare the current framework with traditional approaches for processing TLT data. Active contour models were also designed to automatically extract the boundary location and geometric properties of the sub-surface defects. The results of this study show that the detection of deeper defects (3 in. and beyond) can be improved by analyzing the time-frequency response of surface temperature variations over a period of time. Compared to traditional lock-in algorithms and conventional infrared thermography images, the proposed framework is more effective at removing noisy information and produces images with greater contrast between intact and defective areas of concrete.

Furthermore, a new process has been established to predict depths of delamination in reinforced concrete bridge components. For previous works, traditional approaches were adopted to quantify depths in active thermography, which mainly depend on estimated models as a function of time, frequency, phase contrast, material properties of specimens. This work deals with the passive thermography that is affected by several environmental parameters such as solar heating, daytime or nighttime, wind speed, clouds, shadow. The current work has employed the Machine Learning (ML) technology to estimate defect depths in concrete block. Features, such as phases, amplitudes, frequencies, have been extracted by utilizing the Fast

Fourier Transform (FFT) in a stage of analysis. Furthermore, additional sub-features, minor features, have been added to the ML analysis, for instance average and/or subtraction values between the maxima and minima features, to attain an acceptable learning performance. Support vector machine (SVM) and k-Nearest Neighbor (KNN) classifiers have been trained by using cross-validation with different folds and hold validations. The predicted models have achieved an improved accuracy in estimating delamination depths in the concrete specimens with a good agreement.

CHAPTER ONE

1- INTRODUCTION

1-1 Background

Generally, the material of reinforced concrete is considered as an essential part of constructing the highway bridges. Several significant mechanisms lead to the deterioration in the reinforced concrete deck slabs, such as the corrosion of reinforcement steel, traffic loading, producing of unsound concrete and cycles of freezing-thawing, etc. However, the corrosion of the embedded reinforcement steel is considered as the major factor of deterioration in the reinforced concrete deck slabs. The corrosion in steel causes a substantial increasing in volume of rust which produces internal stresses on the surrounding concrete material [2]. These tensile stresses generate cracks or fracture planes at the levels of the reinforcement steel layers or between them. These fracture planes are indicated as delamination. Consequently, the delamination expands and a separate piece of the reinforced concrete deck slab is split off which is referred as spalling [3, 4].

The damage of spalling has a potential impact on the reinforcement concrete deck slabs. This sort of deterioration issue affects the serviceability,

maintenance, repairing and replacement in the reinforced concrete deck slabs. In addition, the spalling launches as a delamination might have an influence on the traffic flow by speeding up the overall deterioration in the concrete decks or by shutting down the traffic lanes because of renovation process [5, 6]. Furthermore, in the overpass bridges, the spalling in the soffit portion of the deck slabs has critical trouble on the traffic flow underneath the bridges [7]. For these mentioned reasons, it is fundamental to locate and specify the spreading of such damages, delamination, and spalling, which will provide significant information for the existing situation of deck slabs and maintenance necessity in the future.

Several nondestructive evaluation (NDE) technologies have been potentially utilized to detect subsurface defects, such as delamination, that is resulted from deterioration of decks. The most technologies that are widely spread and used are the sounding with hammers and chain dragging, the impact echo (IE), the ground penetrating radar (GPR) and the infrared thermography (IRT) technology [4, 6, 8-11]. However, the sounding with hammers, chain dragging, and the impact echo (IE) demand a direct access to the surface of deck slabs being inspected. On the other hand, the sounding methods could not be precise in their testing [4, 12] and in the situation of chain dragging, it is only limited to the horizontal surface and deck slabs. For

that purpose, the sounding methods and IE are preferred for assessing delamination in deck slabs because of the straightforward use in the inspection and also the low expenses.

On the contrary, the ground penetrating radar (GPR) requires a little traffic control by blocking a partial lane to implement the test on the concrete deck slabs. Furthermore, the GPR technology can become a contactless method by employing air-coupled antennae mounted on a vehicle. In the case of the IRT technology, subsurface defects, such as delamination, can be detected by interpreting the heat energy interrupted by a subsurface delamination which affects the rate of heat transfer through the concrete deck slabs. The results are in hot spots (daytime) when the temperature variations are increasing and cold spots when temperature variations are decreasing (nighttime). Furthermore, the IRT has the ability to capture thermal images for deck slabs being inspected from a distance around 100 feet (30 meters) by mounting the IR camera on a post [1]. The IRT method is a noncontact tool and does not require a direct access to concrete deck slabs.

1-2 Problem Statement

In the United States of America, there are over than 600,000 bridges and around 24% of them are structurally defective or no longer in service [13]. Bridges are considered as one of the most significant components of transportation institutions. Therefore, it is essential to identify damages and maintain an efficient infrastructure since the substantial number of defects and deteriorated bridges in the USA.

Nondestructive testing (NDT) technologies have the possibility and the ability to detect the subsurface defects in the concrete deck slabs. As aforementioned, the most common approaches for evaluating the conditions in concrete deck slabs are the sounding devices (chain drag and hammer sounding), impact echo (IE), ground penetrating radar (GPR) and infrared thermography (IRT). However, the sounding devices and the IE demand blocking the traffic lanes for assessing subsurface defects in the concrete deck slabs. Furthermore, these lane closures rise the cost of assessment and as well decrease the safety of workers and vehicles. On the other hand, the GPR technology is a contactless tool for implementing the evaluation of the concrete deck slabs and requires a partial or no lane closure since it is performed by a vehicle-mounted platform. Yet, this method is not utilized for

detecting defects directly since it is affected by moisture and corrosion in reinforcement steel [14].

Conventional IRT technology provides a very workable tool for remotely capturing thermal images without any direct access to the surface of concrete deck slabs. However, the IRT takes one single snapshot for a specific area of the deck slab at a specific time. Furthermore, for larger deck slab, a number of thermal images are needed to cover the whole entire decks. The conventional IRT technology is a very serviceable tool for detecting shallow delamination in the concrete deck slabs up to 2-inches or less depth.

For all the mentioned reasons, the time-lapse thermography (TLT) method has been adopted in the current study. The concept is by collecting several thermal images for the same area of the deck slab over a period of time. This process takes into consideration the thermal behavior of the same location being inspected at different points of time. This methodology provides an increased detectability of defects with depths greater than 2-inches. Moreover, advanced tools in signal and image processing have been adopted to mine sub-surface defect information from the time-lapse thermography (TLT) images. The thermal images captured over a time are affected by several mechanism factors, for example variations of

temperatures, rain, wind, clouds, fogs, and shadows, ...etc. Consequentially, a multiscale data approach called a Wavelet Transform (WT) was utilized to decompose the TLT images into narrow band time-frequency modes. The purpose of using the WT method is to correlate all the driving mechanisms with the datasets of time-frequency distributions. Further, each decomposed mode has a distinctive information that is in consistence with each separated delamination depending on their depths.

The other problem in the current research was predicting the depths of these delamination in the concrete deck slabs. There are two main approaches adopted by the infrared thermography (IRT): the active and the passive thermography. All previous researches have employed the active thermography for estimating the depths in defects of different material; for example, metal, plastic, composite material and even in reinforced concrete material. However, the active thermography technology has been recently used to estimate depths in delamination in the reinforced concrete specimens. The procedure needs to be performed under controlled circumstances such as excitation of heating, frequency of a test and heating source, …etc. On the contrary, the passive thermography technology is supposed to be held in the fields. The concrete deck slabs are exposed to a direct solar source, the sun, in addition to the changes of ambient temperature. Other parameters affect

this process like daytime, nighttime, wind, clouds, and shadows. For these combined grounds, the active thermography models are not reliable with the passive thermography. Accordingly, the Machine Learning (ML) principle has been proposed as an alternative technique for estimating the depths in the delamination in the reinforced concrete members. The concept of the ML depends on training features that are extracted from a concrete specimen being inspected. Another concept called the Fast Fourier Transform (FFT) has been utilized for aiding of excerpting features like phases, amplitudes, and frequencies. The methodology has adopted two classifiers which are the support vector machine (SVM) and the k-nearest neighbor (KNN) to train and build accurate models. the built compact models are used for testing a group of new thermal images to estimate depths in subsurface defects of deck slabs. The research has illustrated the description and development of the methodology for predicting depths in delamination.

1-3 Goals and Objectives

The most important goals of the current study are to improve the quality on condition assessment tools for highway bridges and develop calibration

standards for the Infrared Thermography. The main objectives of the current study could be outlined in the following steps:

- Developing a framework of fully automatic time-lapse data processing.
- Investigating IR camera sampling rates and sampling interval necessary for carrying out the time-lapse thermography (TLT).
- Performing a comparative analysis of the framework developed with traditional IRT approaches such as lock-in thermography.
- Developing an algorithm to fully calculate phases, amplitudes and frequencies and extracting features from the delaminated and non-delaminated areas.
- Proposing classifier learners such as SVM and KNN to build predictive models to estimate depths in delamination.
- Conducting a comparative analysis of different Machine Learning models for depth prediction.

1-4 Research Approach

The current research comprises of four well-defined phases as illustrated in Figure (1-1). Phase one of this study provides a review of

literature that encompasses the deterioration mechanisms in concrete deck slabs, the very common technologies that have been used for detecting defects in reinforced concrete components, theoretical principles, and the mechanism of transfer heat.

- Reviewing the deterioration mechanisms in concrete deck slabs.
- Reviewing the IR technologies for detecting defects in reinforced concrete components.
- Illustrate the theoretical principles and the mechanism of transfer heat.

- Transforming the 2D IR images into 1D signals.
- Detrending and denoising the 1D signals.
- Decomposing the detrended signals into sets of modes by using a multiscale approach, Wavelet Transform (WT).
- Constructing new 2D high contrast thermal images by isolating and removing the noisy combinations.
- Determining the boundaries of the subsurface defects by adopting an Active Counter.
- Comparing the new obtained results with traditional approaches, such as the lock-in thermography (LIT), based on the signal-to-noise ratio (SNR) approach.

- Fabricating a full-scaled reinforced concrete slab with dimensions (14.5 ft × 10.5 ft × 8 in.) including six embedded targets with depths 2-in., 4-in., and 6-in.
- Testing the concrete specimen with 1-minute interval for more than five weeks.

- Transforming the 2D IR images into 1D signals.
- Detrending and denoising the 1D signals.
- Applying the Fast Fourier Transform (FFT) to create phases, amplitudes, and frequencies.
- Extracting major features from the defects and non-defect areas.
- Extracting minor features from the major features.
- Training the major and minor features by employing the (SVM) and (KNN).
- Testing the compact models on other IR datasets to estimate the depths.

Figure 1-1: Summary of research approach.

In the second phase, an algorithm of a framework for automated time-lapse thermography (TLT) has been adopted and built. The algorithm was developed for detecting and analyzing deep subsurface delamination, such as 3-in and 5-in, in the reinforced concrete components to assist the evaluation in concrete bridges. The current analysis utilized a previous experimental work, a concrete specimen with four embedded targets of defects [15, 16]. First step was transforming the acquired 2D IR images into a 1D time series. Next, a detrend temperature variation is obtained by using the maximum and minimum envelope. However, these temperature variations (the detrend signals) are decomposed in combinations of time-frequency by means of a multiscale approach called a Wavelet Transform (WT). 2D high contrast thermal images are constructed by isolating and removing the noisy modes from the previous step. Once this process is completed, the subsurface delamination can be mined to detect their positions. An Active Counter is adopted to automatically determine the geometry and location of the subsurface defects which is first introduced by Kass et al [17]. The obtained results have been compared with traditional approaches, such as the lock-in thermography (LIT), by proposing and modifying a measure tool based on the thermal contrast called signal-to-noise ratio (SNR). The developed framework has shown an effective outcome of removing noise and producing thermal

images with more contrast between the defect and non-defect areas in the concrete.

Phase three focuses on building and fabricating a full-scaled reinforced concrete slab. The dimensions of the concrete slab are (14.5 ft × 10.5 ft × 8 in.). Two mats of reinforcement steel (top and bottom) in both directions were used with a concrete cover of 2.5 inches. The design of reinforcement concrete slab has been selected to fulfill the minimum requirement of Missouri Department of Transformation (MoDOT). Six targets of open-celled Styrofoam material, with 0.22 inch thick, have been embedded inside the concrete specimen to simulate the real delamination. Three depths of delamination, 2 defects for each depth, have been chosen: 2-in., 4-in., and 6-in. Several tests on the concrete specimen have been completed by capturing thermal images with 1-minute interval. The camera system has been set up in two locations, one is on the north side of the specimen and the other one is on the west side. More than five weeks of testing has been collected for the concrete specimen.

The last phase of this research revolves around developing a methodology to estimate the depths in delamination in the concrete specimen. The work employs the Machine Learning (ML) method to detect the depths.

First, features have been extracted from the embedded defects and the intact (sound) areas by using the Fast Fourier Transform (FFT) approach. Each defect area has been divided into four separated portions. Features have been excerpted such as phases, amplitudes, and frequencies for each portion. Moreover, minor features have been calculated from the major features which gives a boost in building models. The next step is by training the obtained features by employing two classifiers, the support vector machine (SVM) and the k-nearest neighbor (KNN). These classifier learners are available in software such as the MATLAB package. The role of these classifiers was to build compact models then test them on new IR datasets with their features to estimate the depths in delamination. Several training cases have been completed for example a three-week training model on a three-day testing dataset. The obtain results are in good agreement with real delamination depths.

1-5 Contributions

The current study addresses two main contributions which are the detection of deep delamination, especially defects greater than 2-in deep, and

the depth estimation of the delamination since the process completed via passive thermography.

Conventional infrared thermography commonly collects a single thermal image of a region of a deck slab at a given point in time. This process may or may not stand for optimum time for examining the deck slab. However, the time-lapse thermography collects several thermal images of the same spot of the deck slab over a course of a long time period, such as hours, days or weeks. This process allows to analyze the transient thermal of the deck slab to identify anomalies that stem from subsurface defects in deck slabs. Moreover, the study utilizes the Wavelet Transform approach for analyzing signals excerpted from the thermal images at different frequency scales. The process showed that the detection of delamination with depths more than 3-in deep can be improved by adopting the time-frequency response of surface temperature variations over a course of time. Figure (1-2) illustrates in sequence the methodology of the first contribution.

Several researches have previously adopted the process of active thermography to predict depths of defects in concrete deck slabs. Active thermography utilizes objects simulated by external heating or cooling sources such as halogen lamps. Tests like that, are implemented inside

laboratories with controlled environmental conditions. In contrary, the passive thermography tests are held in the fields, for example concrete deck slabs, which are exposed to direct solar and affected by several factors such as wind, shadow, rain, and fog. Eventually, the models adopted by active thermography are not consistent with the passive thermography. That is why the machine learning concept has been used with Fast Fourier Transform to estimate the depths of delamination in reinforced concrete decks. Figure (1-3) depicts all the steps performed to achieve this contribution.

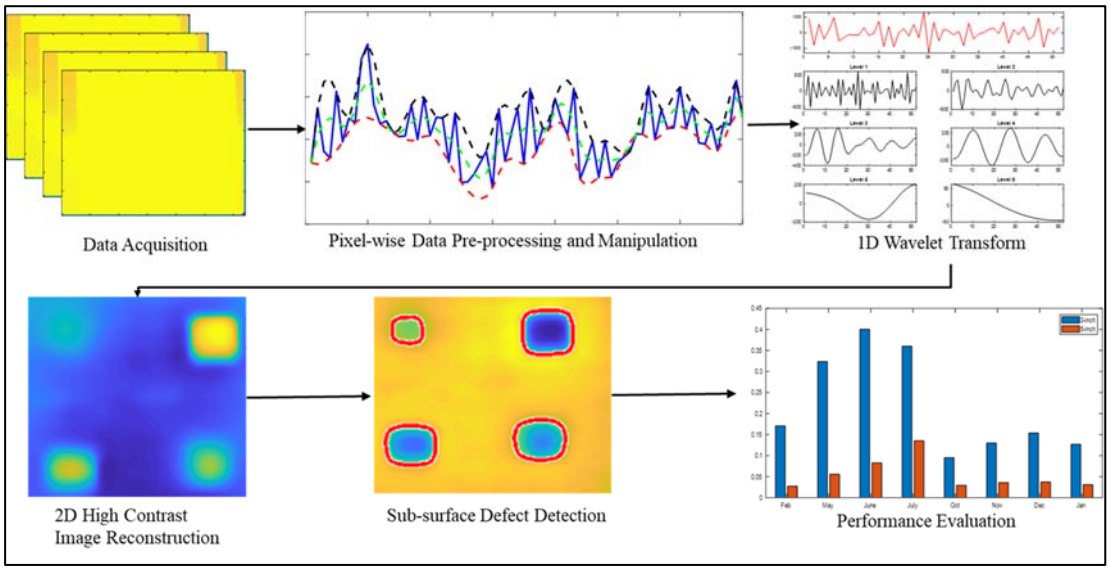

Figure 1-2: A schematic showing the steps to achieve the first contribution (detection of deep depths).

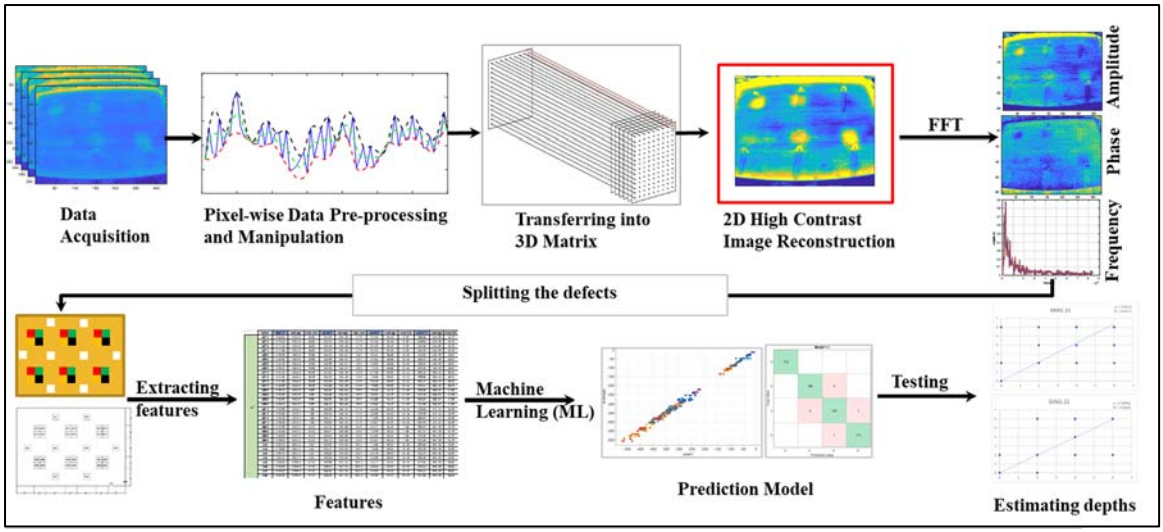

Figure 1-3: A schematic illustrating the steps to achieve the second contribution (estimation depths).

1-6 Outlines of the Dissertation

This dissertation is made up of five chapters. Chapter one concisely introduces some nondestructive evaluation (NDE) technologies and their applications. In addition, it discusses the background, problem statement, goals, and objectives of the current research, research approach and finally the outlines of the dissertation.

The mechanism of delamination in the concrete deck slabs is described in details in chapter two. Moreover, the most technologies of the nondestructive evaluation (NDE) for detecting defects in concrete bridges are discussed with their applications, for example the sounding methods, impact

echo (IE), ground penetrating radar (GPR), and infrared thermography (IRT). In addition, a brief review of heat transfer is summarized in this chapter.

Chapter three introduces a framework of automated time-lapse thermography (TLT) data processing. This chapter provides an algorithm to decompose raw thermal images into narrow band time-frequency domains via an approach called Wavelet Transform (WT). in addition, an active counter model has been included in the analysis to automatically detect the boundaries of delamination. The results have been compared with conventional infrared thermography images. The evaluation shows that the proposed framework is more effective tool.

The determination of depths in delamination in concrete deck slabs by using the concept of machine learning (ML) has been illustrated in chapter four. Furthermore, an experimental work is described in details, in both the laboratory work and the field tests. As well in this chapter, the concept of the Fast Fourier Transform (FFT) is employed to extract the major and the minor features from the thermal images. In addition, classifiers such as the Support Vector Machine (SVM) and the k-Nearest Neighbor (KNN) have been used to create models for predicting depths in the concrete specimen being inspected.

Finally, chapter five is devoted to summarizing the overall conclusions and the recommendations for the future works that are stemmed from the current study.

CHAPTER TWO

2- LITERATURE REVIEW

2-1 Introduction

Reinforced concrete is considered as heterogeneous material and it consists of several various components such as gravels, cement, sand, additives, …etc, which make the reinforced concrete to be more exposed to different types of deterioration [18]. This chapter utilizes the review of literature that is relevant to detecting and quantification of delamination measurements for characterizing damage in concrete bridge components.

The first part in this chapter deals with the mechanism of reinforced concrete bridge deterioration which will be mainly devoted to corrosion in reinforced concrete, reasons, and their process. Moreover, details about delamination, its causes and operation are discussed in the coming section since it is deemed as one of the most subsurface deterioration in deck slabs [19]. In addition, technologies of subsurface delamination detection are displayed. Moreover, theoretical relevant studies of conventional and nondestructive (NDT) methods for the purpose of detecting defects and flaws

in concrete bridges will be presented. Furthermore, apparatus, their procedures and limitations will be presented in details for each technology.

2-2 Deterioration in Concrete Bridges

2-2-1 Corrosion in Steel Rebars

Generally, concrete contributes to an exceptional protecting for steel rebars from corrosion. The environmental of high-alkaline (pH level is around 12.5) in concrete generates a passive film that acts as a barrier to additional chemical reactions, and it is advantageous in mitigating corrosion damage. Reinforced concrete has the features of porosity and has surface microcracks which comes from several effects such as expansion, shrinkage, freezing and thaw, overloading and improper concrete manufacture [18, 20]. All of these factors pave the way to two types of corrosions: Corrosion by carbonation and corrosion by penetration of chloride ions in steel rebars.

Nonetheless, corrosion by carbonation in steel occurs during the ingress of oxygen and moisture in concrete that leads to an interaction between the carbon dioxide with the calcium hydroxide, which exists in cement paste, which leads to form calcium carbonate and reduces the pH level to less than 9.0 [18, 21]. Furthermore, this process will demolish or dissolve the passivity

of steel. The equations of chemical reactions of this process are illustrated below [21]:

$$Ca(OH)_2 + CO_2 \longrightarrow CaCO_3 + H_2O$$

$$2NaOH + CO_2 \longrightarrow Na_2CO_3 + H_2O$$

Usually, the rate of carbonation process moves slowly in concrete especially with low water-cement ratio (w/c). For that reason, carbonation that stimulates corrosion has not been taken into consideration as major issues in reinforced concrete structures as compared with corrosion induced by chloride ions [7].

One of the major reasons of corrosions in steel rebars is the existence of chloride ions in the reinforced concrete. On the other hand, in some circumstances, the lack of chloride ions can cause the corrosion. For instance, carbonation of concrete is a chemical reaction that takes place between carbonation (CO_2) and other available gases and cement paste components.

The breakdown of passive cover in steel rebars by the penetration of chloride ions is one of the most factors that cause corrosion in steel. When the corrosion initiates, steel bars become vulnerable due to the increasing of the level of chloride concentration which is also increased by the numbers of cycles of wetting and drying [7]. Moreover, other factors have an impact on

corrosion such as: the level and standard of concrete made, pH value of pore water, humidity, and temperature of the concrete. in addition, chloride ions are often available in cement paste, aggregate, water that would accelerate admixture, or structures that exposure seawater such as marine or that comes from additive chemicals to use for deicing [7].

Other considerations might affect the corrosion size which is related to construction practice such as concrete cover, crack-control measures and corrosion protection tools [7].

Deterioration of concrete that comes from corrosion in reinforced rebars causes a substantial increase in volume of rust products in around six times larger than in iron [22]. This increasing in volumes produces internal tensile stresses on the surrounding concrete. concurrently, the rust reduces the cross-sectional area of reinforced bars, and with time, a bond loss between reinforced bars and concrete happens and causes cracking or spalling [7]. Moreover, the load capacity of a structure member could be diminished because of the minimizing of the ductility of steel rebars due to corrosion. Furthermore, this issue, the corrosion in steel, might change the failure mode of a structure member from the ductile to brittle mode [23].

2-2-2 Cracking, Delamination and Spalling in Reinforced Concrete

The major cause of cracking inside concrete decks is when substantial expansive stresses on the surrounding area in concrete due to corrosion exceed the tensile strength of concrete [7].

This process of deterioration, the cracking, increases the rate of corrosion by providing more access of oxygen, moisture, and chlorides to the reinforced bars. As a result of that, a surface fracture plane that aligns to the surface of the concrete occurs and is known as delamination. The delamination commonly may happen at rebar depths. This delamination might expand in fundamental areas inside concrete deck slabs. Consequently of delamination expansion, a spall occurs in which a separated piece of concrete is split off from a deck slab [7]. This latter outcome can be an exceptional concern in reinforced concrete deck slab bridges.

The spalling in concrete decks is one of the major worldwide deterioration issues that has been attention and consequences for highway and transportation agencies due to potential serviceability, preventive maintenance, repair, and replacement in reinforced concrete bridges. Spalling launches as a delamination that comes from either in embedded steel rebars or stresses caused by external traffic loading. This process may speed up the

total deterioration in concrete components of the deck slabs. Moreover, the spalling in the soffit part of deck slab in overpass bridges can have critical issues on the safety of traffic loading beneath the bridges [24].

2-2-3 Production of Improper Concrete

During the production of concrete, delamination could be initiated inside deck slabs. In this situation, the main reason of creating such delamination is the bleeding. Drying the top surface of deck slabs prior to the ending of water bleeding and the first set of concrete commonly lead to entrap water and air beneath the densified surface of concrete. This process of the accumulation of water and air beneath the surface, creates a high water-cementation materials and is close to the surface of weakness planes, that are vulnerable to traffic load [25]. Moreover, this procedure causes a separation of about 3-6 mm (⅛ - ¼ inch) upper layer of mortar cement from the underlying concrete [26]. In other words, the concrete is poured and placed, the cement and aggregate settle inside the deck slab while the light materials (air and water) move to the top surface of deck slab [14].

2-2-4 Cycles of Freezing-thawing

Freezing-thawing in concrete is considered one of the frequent reasons of forming delamination in concrete deck slabs. It commonly happens in the deck slabs that have poorly air-entrained or not air-entrained concrete, which works as a treatment for delamination [25, 26]. When temperature drops down below zero degree 0°C, the existence of water inside the pores of concrete would be frozen and that leads to increase the water volume by 9% [26]. This process will create a pressure inside the concrete and the accumulation effect of the freeze-thaw cycles would definitively produce cracking, scaling and deterioration of concrete especially when the produced pressure inside the pores exceeds the tensile strength of concrete [26]. Unlike the indoor concrete deck slabs, the outdoor deck slabs that are exposed to cycles of freezing-thawing might have delamination at any depth or plane inside the deck slabs depending on several factors such as the winter hardness, level of water-saturated and pore size inside the concrete slabs [25].

2-3 Detecting Technologies of Defects in Concrete Decks

This section deals with and discusses the most common technologies for detecting subsurface delamination in concrete deck slab bridges. As

mentioned before, it is important to detect delamination in early stages since they affect the serviceability and integrity of the concrete bridges and to overcome further deterioration.

Two main technologies, conventional and nondestructive evaluation (NDE) methods are included in this chapter. Basic principles, advantages and limitations will be briefly described.

2-3-1 Conventional Methods

Two major methods are used to detect defects or delamination in concrete deck slab depending on sounding techniques: hammer sounding and chain dragging manners. The hammer sounding technique encompasses a tapping on the top surface of concrete deck slab at various locations and monitoring the received produced sounds. For non-defected area, a clear sound will be created while a dull or hollow sound will be heard for defected area.

In deck slab bridges that have considerable areas, a chain drag manner is a reasonable tool to be used to detect defects. The same concept is used as in the hammer sounding method. Non-delaminated area will make a clear sound. On the contrary, delaminated areas will produce dull sounds.

The procedure of the drag chain is mentioned in details in the ASTM D4580-03 [27]. Both methods, the chain dragging and hammer sounding have some advantages which are summarized in simple, portable and low cost operation [8].

The methods have some disadvantages and limitations, which could be summed up as their need to a direct access to a top surface of an inspected deck slab. Moreover, it requires a route closure for a bridge and special supplies and tools to reach bridge components. One of the most deficiency of this method is that it cannot be used for vertical components of bridges such as piers or columns. Furthermore, this method is used for qualitative inspection by tapping on the deck slab with hammer or a chain [28].

2-3-2 Nondestructive Evaluation (NDE) Technologies

Nondestructive test (NDT) methods are utilized to evaluate the properties conditions of materials, such as concrete steel, …etc. [29], in bridge components, buildings, pavements and other concrete structures [29]. It may refer to a nondestructive inspection (NDI) or nondestructive evaluation (NDE). The idiom (NDE) is expressed as a nondestructive considerable damage to concrete components.

Nondestructive evaluation (NDE) methods are used to assess concrete construction for several major reasons which could be briefly summarized as [29]:

- *Quality control of new construction.*
- *Examining and resolving issued inside new construction.*
- *Evaluating of old concrete construction.*
- *Assessment of repairs on concrete construction.*

In this section, the most widespread technologies or techniques are limited to three methods: Impact Echo (IE), Ground Penetrating Radar (GPR) and Infrared Thermography (IR).

The concepts, instrument tolls and limitations for each technology are detailed in the American Concrete Institute Report ACI-228-2R-98 [29].

2-3-2-1 Impact Echo (IE)

The impact-echo testing is a technique that is utilized for flow detection in concrete construction. It is a stress-wave method that is monitoring a sound wave resulting from a mechanical impact [30]. The main principle of this method is by introducing a stress pulse into an inspected object (the concrete)

by impacting it with an impactor and recording the response. Details of the method principles, apparatus and procedure are listed and summarized in the ASTM C1383-98 [31] and ACI 228-2R-98 [29].

P-waves (Primary waves) and S-waves (Secondary waves) are initiated by a stress pulse disseminate into the tested concrete object along hemispherical wave fronts. Throughout this process, the waves are reflected due to changes in the interface of the inspected object (such as delamination and flaws). The oncoming of these reflected waves at the surfaces where the action was originated produces displacements that are being measured by a receiving transducer and recorded using a data-acquisition system [29].

Since the time-consuming is used in such cases, the preferred approach is frequency analysis. The basics of this approach is that the generated stress pulse endures several reflections between the inspected surface and boundaries (such as delamination). The receiving transducer receives the frequency and reflects pulse which mainly depends on the wave speed and the distance between the inspected surface and flaws. This recorded frequency is named a thickness frequency and it relies on the inverse of the component concrete thickness [29].

The analysis of Fast Fourier Transform (FFT) is employed in such cases to transform signals from time-domain to frequency domain to obtain an amplitude spectrum [29, 31].

IE method has been considered as a successful method to detect defects such as voids and honeycomb in concrete members, delamination in deck slabs and voids in tendon ducts [30]. The implementation of IE method always requires an impact on inspected surface of concrete member. Moreover, the method is mainly relative to the experience of the operator [30] and it is not simple as the interpretation of the hammer and chain drag methods.

2-3-2-2 Ground Penetrating Radar (GPR)

The Ground Penetrating Radar (GPR) technique utilizes high frequency electromagnetic waves to evaluate the concrete deck slabs. Overlaid with asphaltic concrete wearing surfaces [32]. The typical length of waves is ranged from 1GHz to 2.5 GHz and is emitted via an antenna into the inspected concrete deck slabs. Due to interfaces between the concrete and steel rebars, a reflected energy is created in the electromagnetic properties of these materials and it is diagnosed and recorded by a receiver antenna for the study [32].

This procedure can be usually accomplished with air-coupled or ground-coupled horn antenna located from 0.3 m to 0.5 m the top surface of evaluated deck slab [32]. More details about the procedure and apparatus are listed in the ASTM D6087-08 [33].

The GPR has the ability to provide scanning information (i.e., detect corrosion damage in concrete decks) for situations of bridge decks without overlays and with portland cement concrete overlays [33]. Moreover, it is considered as a nondestructive method that can inspect concrete deck slabs in bridges with asphalt overlays [33].

The technique has capability to achieve the test with high-speed scanning on bridge decks without traffic closure or with partial lane closure depending on whether the test is air-coupled or ground-couple. For air-couple procedure, ASTM standard requires a transverse distance of less than 1.0 meter and a longitudinal distance of less than 0.15 meter to the inspected surface [33]. While for ground-couple test, the antennas are required to be directly drawn on the deck slabs which means a lane closure.

2-3-2-3 Infrared Thermography

Infrared thermography (IR) is one of the technologies that have been devoted to detecting subsurface delamination in concrete deck slabs without any contact with surface of inspected object on the contrary of the other nondestructive methods. The data collection with this technology is faster and simpler with almost no traffic closure for the inspected concrete deck slabs. In addition, the interpretation and analysis of IR images are also easy. Moreover, IR images could be obtained from a range of 30 meter (100 foot) or more during the test by using appropriate thermal camera [1]. This technology mainly depends on measuring the radiant energy emitted from the surface of inspected object. A thermal camera is employed to capture the emitted thermal radiation into IR images. Another concept for this technology is subsurface delamination inside the concrete object which interrupts heat flow [29]. A full details and description will be described in the next sections.

2-4 Theoretical Principle of IR Thermography

The purpose of this section is to describe the fundamental aspects behind the infrared thermography (IR). First, a brief review will describe the basic concepts of IR thermography and their instruments will also be included.

Moreover, a brief review of the heat will be discussed. Finally, the applications, advantages and limitations will be overviewed.

2-4-1 Fundamental Principles of IR Thermography

Thermography is a technique that utilizes infrared sensors to detect thermal radiation emitted from objects and produces a picture of a surface temperature based on that radiation [29]. Infrared radiation is emitted from any object exceeding absolute zero (0° Kelvin or -273 °C). the infrared radiation is an electromagnetic energy and it is defined within two spectrum windows: 3-5 μm and 8-14 μm [34]. Both the emissivity and temperature of substance are the rate at which the energy of an object is emitted [35]. Boltzmann's law describes the energy of relation, which states that the radiated power of a substance is equal to the total temperature of the 4th power as:

$$q_{rad} = \varepsilon \, \sigma \, T^4 \tag{2.1}$$

q_{rad} = emitted energy by a surface

Ɛ = material emissivity

σ = Stefan-Boltzmann constant (5.6×10^{-8} W. m^{-2}. K^{-4})

T = temperature (°Kelvin)

As shown in the previous equation, the released energy is mainly dependent on the fourth power of the temperature. In addition, emissivity is a unitless number and refers to the effectiveness of an object that transmits energy by radiation heat [36]. In other words, it is the relation of emitted energy to emitted radiation in a perfect circumstances or that comes from a blackbody [36].

Disturbances such as delamination inside a concrete deck slab disrupt heat transfer, causing localized surface temperature variations [4]. The localized surface temperature fluctuations influence on the amount of radiation released from the surface as illustrated in Figure (2-1).

On the day hours, as the concrete is warming up, the temperature of the surface above defective area, i.e., delamination, is greater than the temperature of the surface above the non-defective area, i.e., sound area, since the mass above the delamination is less than the mass above the sound area that observes the heat flow. In concrete, on the night hours, since the concrete is cooling off, the temperature of the surface above delamination might be lower than the temperature of the surface above the non-defective area [37]. The area of subsurface delamination could be distinguished by analyzing the

surface temperature varieties. These surface temperature varieties are inspected in terms of thermal contrast to implement quantitative examination of information in this consider. The thermal contrast is defined as:

$$\Delta T = T_{defect} - T_{sound} \tag{2.2}$$

where ΔT = thermal contrast

T_{defect} = surface temperature above a delamination

T_{sound} = surface temperature above a non-defect area

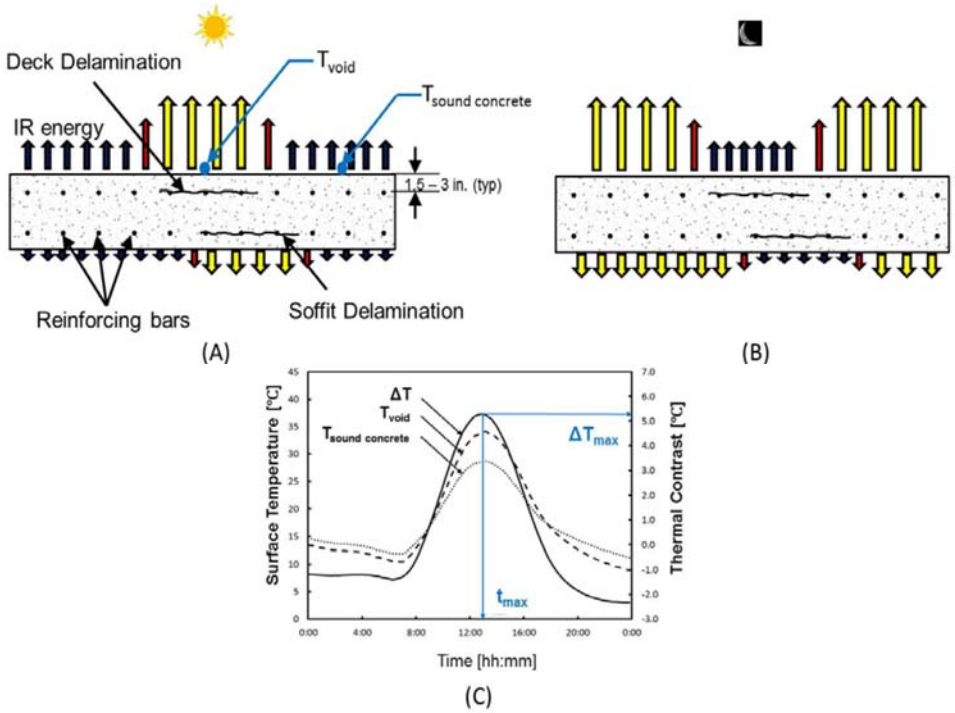

Figure 2-1: Thermal response of delamination in concrete: (A) daytime condition [1]; (B) nighttime condition; (C) surface temperature and thermal contrast as a function of time.

2-4-2 Overview of Heat Transfer

2-4-2-1 Mechanism of Heat Transfer

Heat can be transferred from one object to another object due to variations in temperatures. Generally, there are mechanisms of heat transfer known as: conduction, convection, and radiation. In concrete, the transfer of energy between a surface of an object and surrounding environmental occurs by the natural convection, the thermal radiation in the surface of the concrete, the conduction inside the concrete elements themselves, and the solar radiation [38] from the sun as illustrated in Figure (2-2).

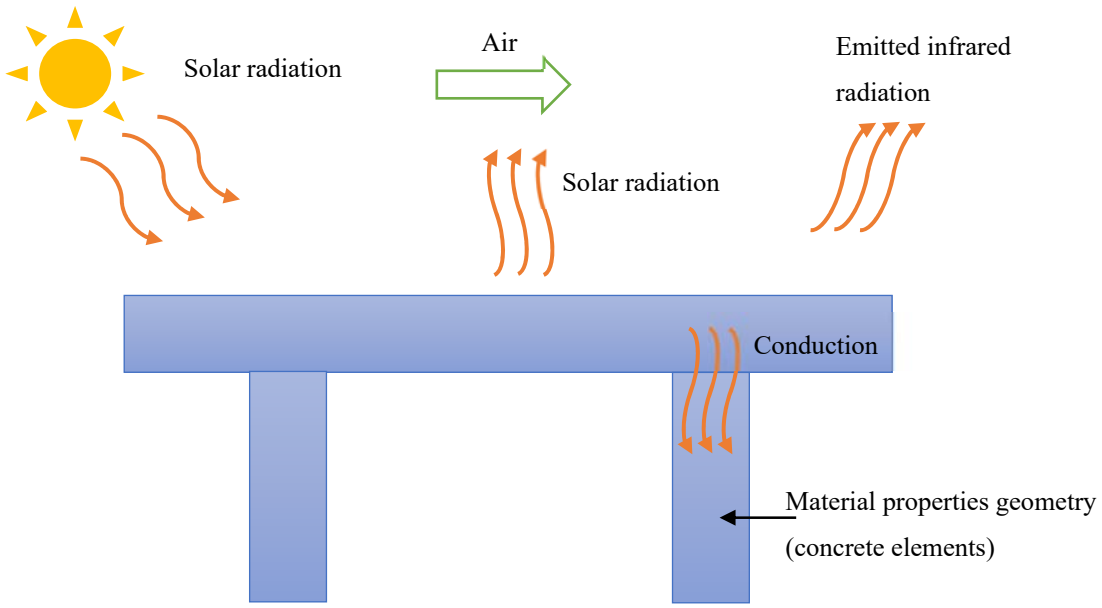

Figure 2-2: Illustration the mechanism of heat transfer from surrounding climate on concrete elements.

The thermal energy is, q_s, that is absorbed by the members of concrete bridges due to the solar radiation, the sun, can be obtained by:

$$q_s = \alpha_s I_s \tag{2.3}$$

where α_s = the absorptivity coefficient of concrete and ranges from (0 to 1.0).

I_s = the solar radiation on the concrete.

Several factors are affecting the solar radiation, I_s, for example the length of the day, the season of the year, the clouds, the elevation of the concrete bridge and the location on earth [38]. The absorptivity, α_s, refers to the adequacy of absorbing the radiation heat, for instance the value 1.0 of α_s marks to a material that absorbs all the heat and reflects none. The value of absorptivity is affected by several factors such as the texture and color of the materials.

The rate of heat energy transfer by the convection, q_c, is mainly related with some influences such as the variations of temperatures between the surface of concrete bridges and the air. The equation is approximately written according to Newton's convection law as follows:

$$q_c = h_c(T_s - T_{air}) \tag{2.4}$$

where h_c = the convection coefficient (W. m^{-2}. $°C^{-1}$)

T_s = the temperature of the concrete surface

T_{air} = the temperature of ambient

In this case, the convection coefficient can be expressed as a function of two factors, h_n and h_f, as follows [38]:

$$h_c = h_n + h_f \tag{2.5}$$

where h_n = a parameter for concrete bridges has an average value equal to 6 (W. m^{-2}. °C^{-1}).

h_f = a function of the wind speed υ (m. s^{-1}) and can be stated as $h_f \approx 3.7 \times \upsilon$.

It can be calculated from the equation (2.4) that if the temperature of concrete surface is more than the ambient temperature, for example the sun warms up the concrete above the ambient temperature, the convection heat is larger than zero. In this situation, the increasing of wind speed will increase the energy transfer from the concrete surface to ambient air, leading to reducing the thermal heat in the concrete [24]. On the contrary, if the concrete temperature is less than the ambient temperature, for instance shady situations, that will produce a negative convection heat. In this case, the thermal heat in concrete will increase since the wind will speed up the heat transfer to the concrete [24].

Equation (2.3), as illustrated in section (3-1), expresses the thermal energy of emitted radiation, q_{rad}. The equation is utilized to calculate the temperature of the concrete surface.

The last expression of the heat transfer is the thermal energy transfer by conduction, q_{cond}. In the concrete solid, a one-dimensional equation can be stated as:

$$q_{cond} = k\left(\frac{T_s - T_{air}}{L}\right) \tag{2.6}$$

where k = the thermal conductivity (W. m^{-2}. K^{-1})

L = the concrete thickness in the heat flow direction

T_s = the temperature of the concrete surface

T_{air} = the temperature of ambient

Thermal conductivity, k, refers to the rate of energy heat passing through a unit area of a material of a unit thickness for a variation of temperature of one degree.

2-4-2-2 Thermal Inertia

The thermal inertia can be expressed as a thermal mass, I. This expression refers to the ability of a material to conserve and conduct the heat energy. The term of thermal inertia can be written as follows:

$$I = \sqrt{k\ \rho\ C_p} \tag{2.7}$$

where k = thermal conductivity

ρ = the density of the material

C_p = the heat capacity (or the specific heat) of the material

The specific heat indicates the magnitude of heat energy that is utilized to increase the temperature of a unit mass of a material with one degree.

2-4-2-3 Heat Diffusion

The heat diffusion term can be given in the isotropic homogeneous materials according to the Fourier Transform concept [39]:

$$\frac{\partial T}{\partial t} = \alpha\ .\nabla^2_{x,y,z}\ T \tag{2.8}$$

where T = the temperature

t = the time

∇^2 = the Laplacian operator

α = thermal diffusivity of a material

the Laplacian term of the temperature in the Cartesian coordinate system can be expressed as:

$$\nabla^2 = \frac{\partial 2}{\partial x^2} + \frac{\partial 2}{\partial y^2} + \frac{\partial 2}{\partial z^2} \tag{2.9}$$

The expression, the thermal diffusivity, α, can be defined in the next equation which refers to temperature changes in a material:

$$\alpha = \frac{k}{C_p.\rho} \tag{2.10}$$

where k = thermal conductivity

C_p = heat capacity

ρ = density of the material

It can be seen from the equation (2.9) that a material with a high thermal diffusivity refers to a fast heat transfer, but the heat storage will be low. The feature of having a high thermal diffusivity in a material leads to high reaction in temperature changing. In contrast, having a low thermal diffusivity in a material marks to a low heat transfer but with a large heat storage, which indicates a low reacting in the temperature variations [36].

2-4-2-4 The Flow of Transient Heat

The knowledge of expression of the flow of transient heat is practically functional since it is demanded in detecting the defects in the concrete. the equation of the one-dimensional heat flow is possible to be solved by using the concept of diffusion as described in the previous section. Equation (2.8) could be written as follows [39]:

$$T_d = T_\infty + (T_i - T_\infty) erf\left(\frac{y}{2\sqrt{\alpha t}}\right) \quad (2.11)$$

where T_d = the temperature at any depth in the material

T_∞ = the applied constant temperature at the surface of the material

T_i = the initial temperature of the material

erf = Gaussian error function

y = depth into the material

α = thermal diffusivity of a material

It is clear that the equation (2.8) is not a linear throughout the calculating of surface temperature. Moreover, for complicated cases, such as heterogenous materials or/and having subsurface defects and complex boundary conditions, the solving of the transient heat transfer needs to be

performed by advanced techniques. Methods like the finite element (FEM), finite volume (FVM), and finite difference (FDM) could be employed to solve such a case like equation (2.8).

2-5 Instrument of IR Thermography

2-5-1 An Overview

An IR camera utilized the thermal radiation that is emitted from the surface of an object to produce images. In other words, the temperatures of the object being inspected are interpreted to images. These produce IR images could be filmed or shot from a distance reached to 100 feet (about 10 meters) depending on the IR camera's lens [40]. One of the most advantages of using IR thermography technology is the ability to improve the efficiency and safety of testing without traffic block or hands-on access. New technologies of IR thermography have been improved and adapted by researchers, which are the deck and soffit scanner and the ultra-time domain infrared. Each one of these technologies can be utilized with different environmental requirements. The following sections will describe three systems of infrared technologies that are used to inspect objects. The technologies are the hand-held camera system, the deck and soffit scanner (IR-DSS) and the ultra-time domain infrared (IR-

UTD). More details will be briefly explained essentially for the IR-UTD since it is corresponding to the principles of the time-lapse thermography (TLT).

2-5-2 Hand-held Camera Method

The hand-held camera technology is considered one of the common methods that is utilized to detect defects, for example defects in the concrete deck slab. A typical photo of a hand-held camera, the FLIR T620, is shown in Figure (2-3). This type of cameras is lightweight, built-in, and easy to use by inspectors. In this method, the hand-held camera can take images for both deck slab and the soffit of an inspected bridge with blocking the traffic flow.

It can be seen in Figure (2-4) that the produced IR image displays the subsurface defect inside the concrete deck slab as a thermal contrast. Several reasons are involved to cause subsurface defects, which are previously explained, such as corrosion in the reinforcement rebars which leads to increase the size of these rebars. More factors engaged in creating subsurface defects such as traffic loading. Figure (2-4) illustrates the photos that are taken to an inspected bridge in typical environmental conditions. Both images have been simultaneously taken at the same time by using the hand-held camera while the traffic flow is open. The image on the left is a photographic, while

the image on the right is the infrared image showing the bridge in a thermal distribution across the bridge. It is obviously that the image has a temperature scale that explains where the delamination is within the deck slab. Since the image is taken during the day hours, the delamination is appeared a higher temperature according to the thermal scale. It is important for inspectors to be closer to the existed delamination to obtain a good thermal contrast for them, to estimate their size, their area and even the depth by using the appropriate data analysis.

Figure 2-3: FLIR T620 hand-held infrared camera.

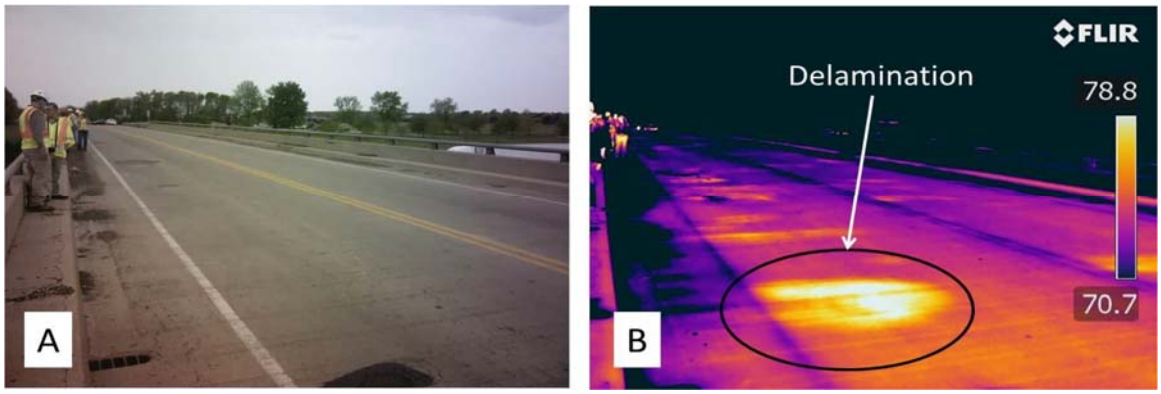

Figure 2-4: Image of a bridge deck (A) and an IR image (B) of the same bridge deck area showing a subsurface defect.

2-5-3 IR-Deck slab and soffit system (IR-DSS)

The main purpose of using the IR-DSS system is to reduce the testing time for an inspected deck slab especially when its area is massive. In this system, the camera is mounted on a vehicle while the system keeps capturing IR images. In other words, the IR-DSS captures individual IR images from one spot to another spot for the same objected being inspected, which is similar to the process that is held by the hand-held thermal camera [41].

It can be seen from Figure (2-5) that the IR-DSS system is attached with a linear encoding for observing the position of IR-camera amid information procurement. The encoding device is mounted on a fifth wheel that is connected to the vehicle. Moreover, the encoding is precisely used to track the position of each image being taken for the deck slab being inspected.

Visual as well as IR images are collected and spatially associated through the camera alignment and precision encoding wheel, trigging simultaneously data collection for each camera in the IR-DSS system [41]. Figure (2-5) states the whole details of the framework. It appears the camera mounted on a pole associated through a hitch in a truck. The IR camera is elevated around 10 feet (about 3 meters) above the ground level. The encoding is connected to the frame that is held the camera. Cables are linked to the camera and encoding device to the data acquisition device.

Additional advantage of the IR-DSS system that has a flexibility to be mounted to any car that has a hitch. This permits the framework to be utilized in small spaces which are nonaccess to conventional vehicles. In addition, the camera head can be oriented to any direction, such as upward viewing, where the soffit of a bridge could be scanned and inspected.

Finally, the collected data by the IR-DSS system are visual and thermal images. This feature gives a merit to the images being captured to be stitched together and give a plan of view, for instance a deck slab of a bridge. Figure (2-6) shows an example of a detached images of an inspected object.

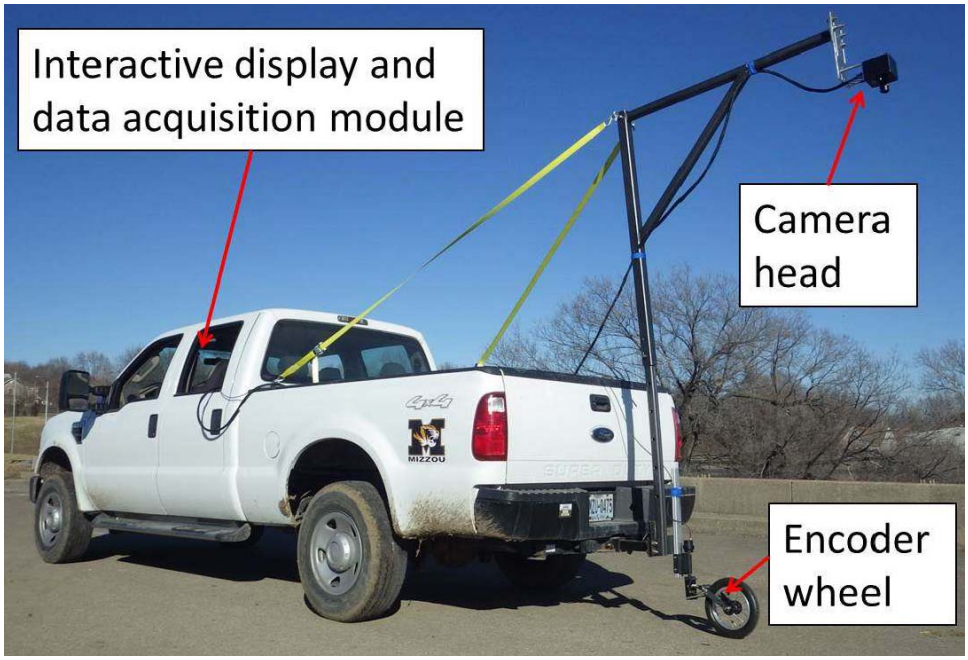

Figure 2-5: Setup of the IR-DSS system on a truck.

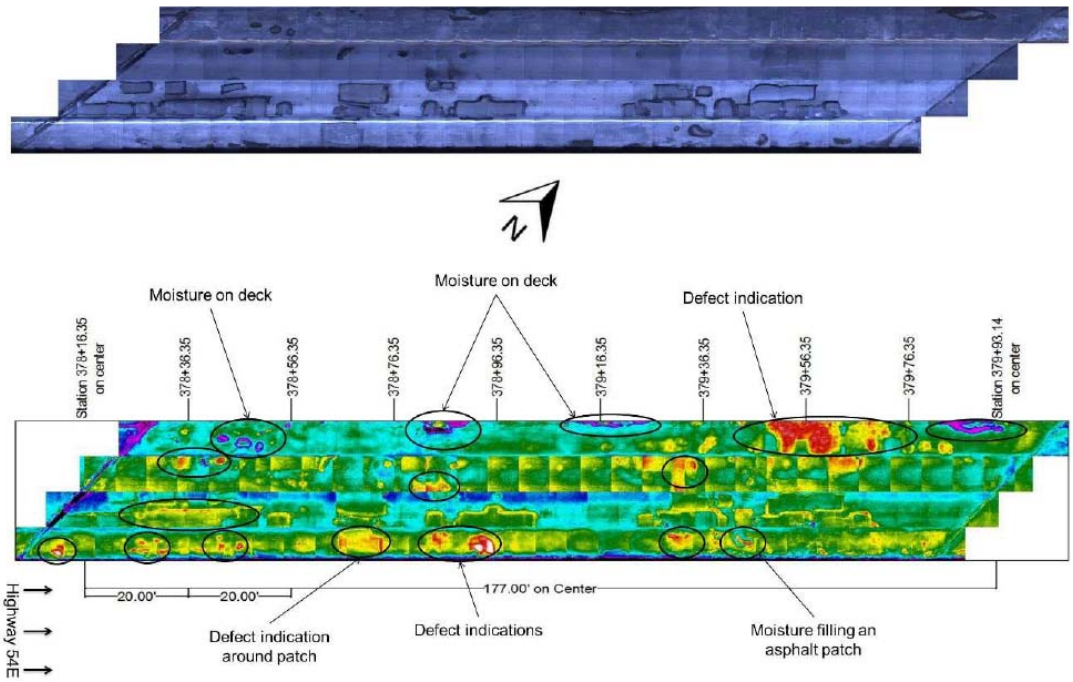

Figure 2-6: Detached Images by IR-DSS data.

2-5-4 The Ultra-Domain Infrared (IR-UTD)

The Infrared Ultra Time Domain (IR-UTD), Figure (2-7), is a transient imaging technology and considered one of the new methods that is explored to boost the reliability of IR images. This technology was originally adopted and developed by Fuchs Consulting Inc. (FCI) of Leesburg, VA [41] which utilized to asses bridge conditions. The IR-UTD system collects infrared images over a course of time, such as hours, days, weeks or months, for a specific specimen or object and takes into consideration the effect between ambient environment and thermal contrast inside delamination [41]. The approach has the same principle of the Time-Lapse Infrared Thermography (TLT) which films a video sequence of thermal contrast of an inspected surface instead of a snapshot over a course of time [42].

The IR-UTD system could be installed in the field to capture a series of thermal images which allows to consider temperature variations over time for an object. These captured IR-images are processed by an appropriate software or program, such as MATLAB, to detect delamination locations, their sizes and even depths could be precisely ascertained [41, 43]. Moreover, an analysis of time series of thermal images can be also used to create and reconstruct well-defined image into a high contrast composite image [41, 42] as shown in

Figure (2-8). The IR-UTD system could be installed, and the infrared camera can be mounted on a pole to cover a large area of a deck slab as shown in Figure (2-7).

It could be seen that many IR-images for the same area of the deck slab are taken over a course of heating and cooling cycles. The interval time between each is ranged from 1 second to several minutes or hours and the total time of the test could be over several hours, days, weeks, or months.

The IR-UTD system is mainly made up of three major components which are: a camera box, data acquisition and interactive display as shown in Figure (2-9). The camera box has both infrared and visual cameras, which simultaneously capture the same spot of an inspected object. The camera is attached to the data acquisition (DAQ) with a cable that transfers the collected data and powers the cameras. Moreover, DAQ has a battery, a computer for controlling the system and hard drive. The last part of the system is the interactive display that illustrates the visual and the thermal images.

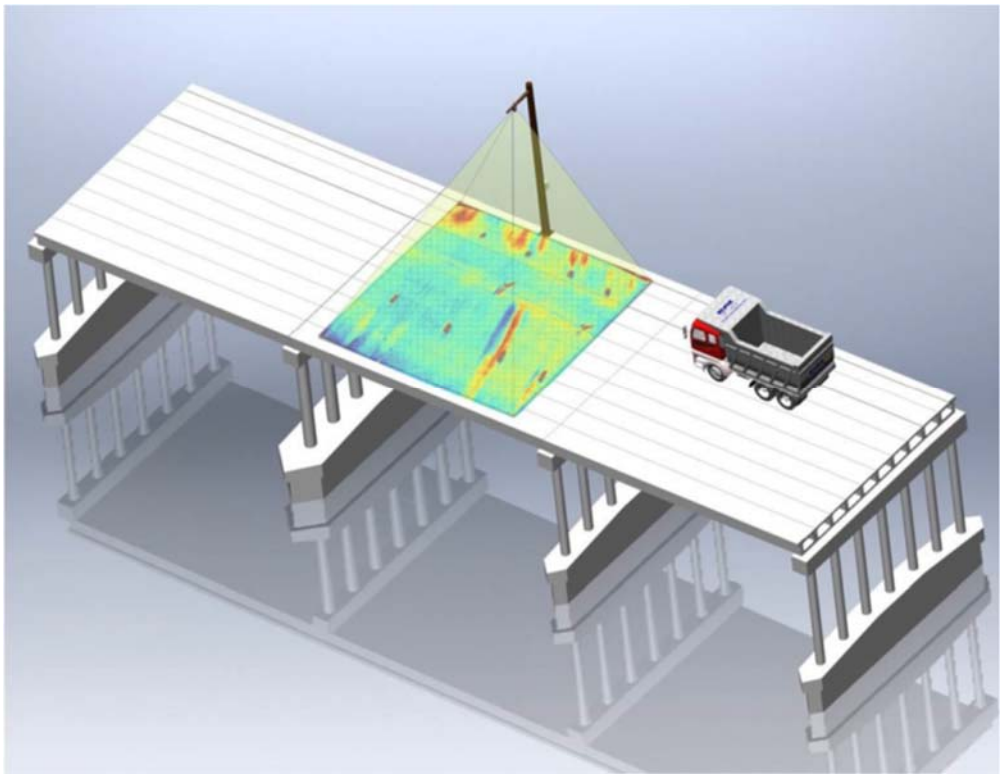

Figure 2-7: Illustration of the IR-UTD process for collecting data during temperature cycles to produce an image of damage in a bridge deck.

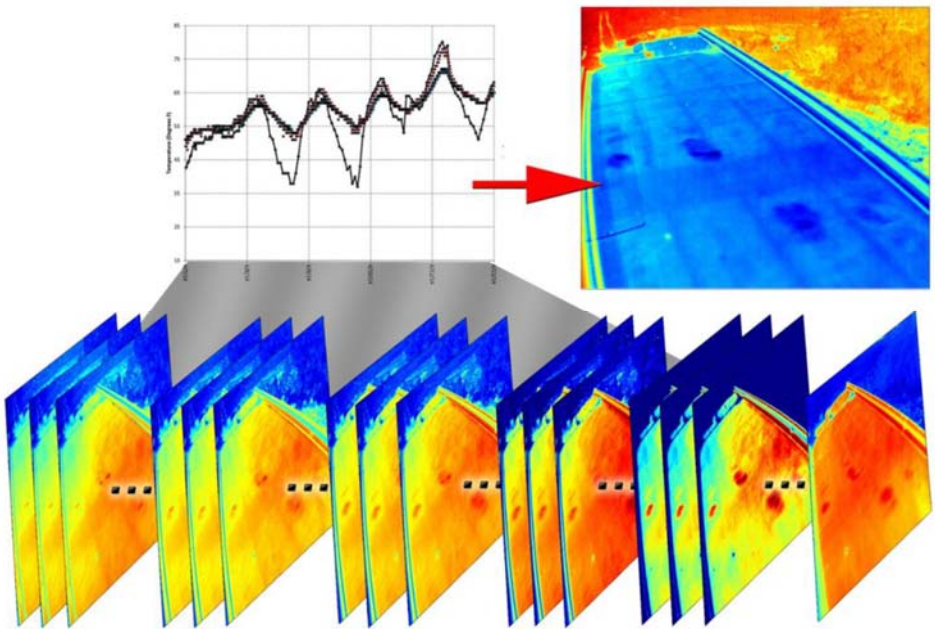

Figure 2-8: Schematic diagram of imaging a large area of bridge deck from a light pole or mast.

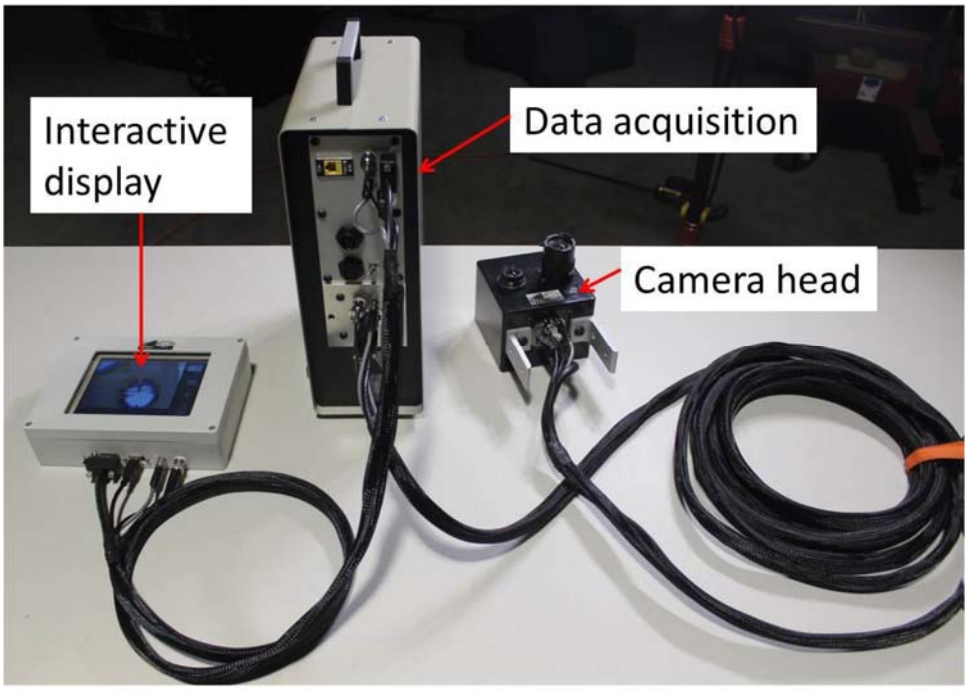

Figure 2-9: Photograph of the IR-UTD system components showing the camera head, the data acquisition module, and the touch-screen display.

The IR-UTD system includes a manual pan and tilt stage that allows the cameras to be angled and provides several field-of-view according to the locations of inspections. The IR-UTD system, the camera box, could be connected and mounted on a pole or mast which is attached to a bridge. The advantage of that is the system that collects IR data without blocking the traffic loading as shown in Figure (2-10).

Figure (2-11) states that the IR-UTD system can be set up into a portable mast which has the facilitation to be towed by a hitch and easily moved if needed.

After the setup is finished, IR-URD system starts collecting IR data, then specialized algorithms are used to process the thermal images of an inspected concrete specimen.

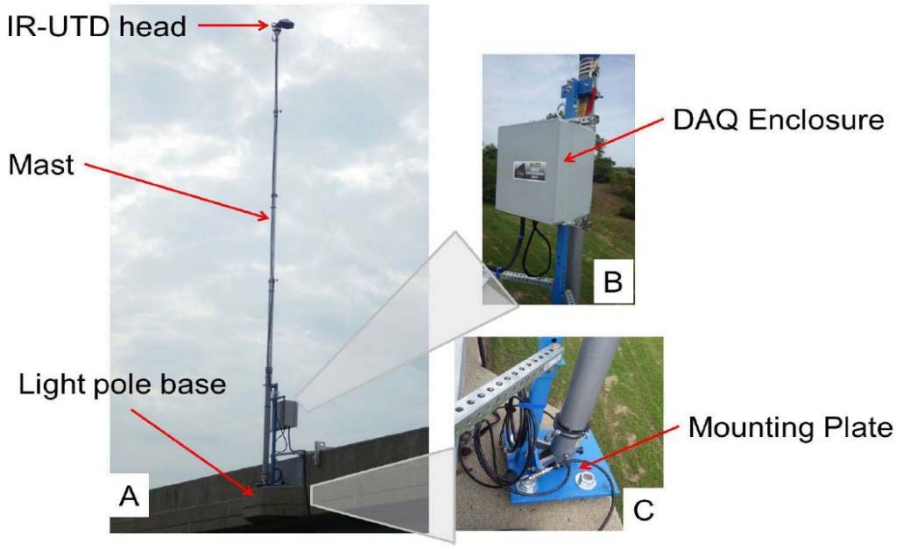

Figure (2-10). Image of the IR-UTD system mounted on a light pole base.

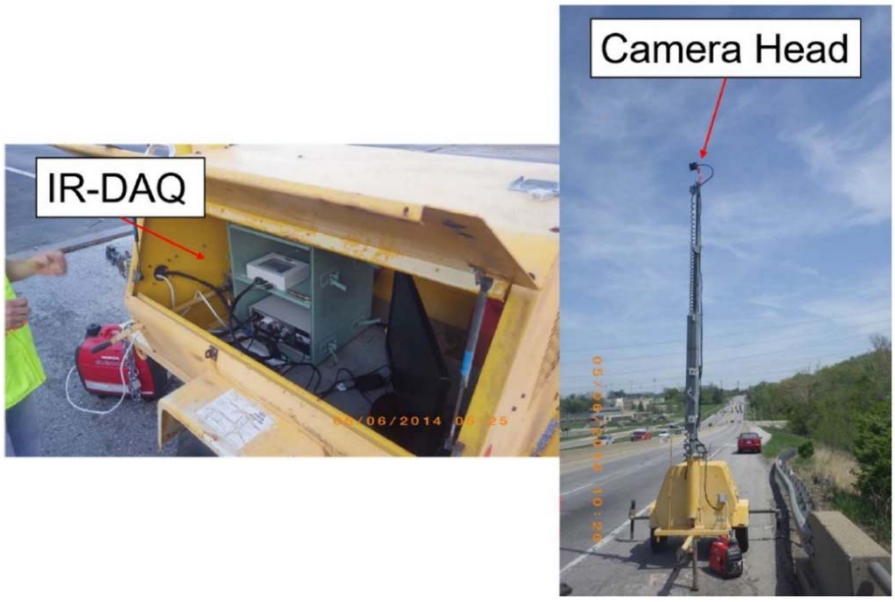

Figure (2-11): IR-UTD system set up in a portable DAQ system alongside the roadway.

CHAPTER THREE

3- A FRAMEWORK FOR AUTOMATED TIME-LAPSE THERMOGRAPHY DATA PROCESSING

3-1 Background

Highway agencies need to evaluate the condition of bridge decks to identify damage and optimize the timing and scope for preventive maintenance, repair, and replacement. Concrete bridge decks deteriorate due to traffic and environmental loading that causes cracking and spalling of the concrete. Spalling typically initiates as a subsurface delamination caused by corrosion of the steel reinforcing embedded in the deck or stresses caused by traffic. The subsurface deterioration is not apparent on the surface of the concrete and, therefore, cannot be evaluated by visual means [19].

Consequently, visual inspection of the deck surface may not characterize the condition of the deck adequately to support effective decision-making regarding preservation, repair, and replacement. Nondestructive testing (NDT) techniques have the potential to detect subsurface defects (i.e., areas of delamination) that result from the deterioration of the deck. The most commonly used NDT methods for the

assessment of concrete bridge decks are manual sounding (chain drag or hammer sounding), impact echo (IE), ground penetrating radar (GPR), and infrared thermography (IRT). Acoustic methods such as hammer sounding, chain drag, and IE are usually preferred for assessing sub-surface defects in the concrete due to the low cost and simplicity. However, these methods require traffic control to be implemented because they rely on surface impacts using a hammer, chain, or impactor at each test point on the deck. Lane closures increase the cost of the inspection and may present a safety hazard to workers and motorists. GPR methods are non-contact and may be implemented from vehicle-mounted platforms, requiring little or no traffic control. GPR is sensitive to moisture and corrosion-causing chlorides and provides a qualitative measure of deterioration; however, it does not detect subsurface defects directly [14].

Conventional IRT captures a single thermal image of an area of the deck at a given point in time. Several images of different areas of the deck may be required to capture the entire deck surface due to the size of the deck. Subsurface areas of delamination are detected by interpreting the thermal anomalies which appear in the IRT images. Areas of delamination interrupt thermal transfer through the deck during diurnal temperature variations of the ambient environment surrounding the concrete and heating caused by solar

loading (sunlight). The result is in ‘‘hot spots” when ambient temperature is increasing and ‘‘cold spots” when temperatures are decreasing (e.g., during nighttime). Conventional IRT methods are non-contact and can be implemented from vehicle mounted platforms that require little or no traffic control. Conventional IRT methods can typically detect areas of delamination that are 2 in. or less beneath the surface [44]; for this reason, conventional IRT is most useful for evaluating relatively shallow defects.

TLT consists of collecting multiple images of the same area of the deck at different points in time. Multiple images captured at different times can be processed to analyze characteristics of the thermal behavior of the material over time. For bridges, capturing TLT images typically includes mounting an IRT camera on a light pole, mast, or sign structure where large areas of deck can be captured in a single image. From this position, images are collected at a fixed sampling interval (e.g., every 10 min) for some data collection period of hours, days, or even weeks. The overall objective of this study was to develop improved methodologies for analyzing TLT data to provide increased detectability of defects with depths of greater than 2 in. Recent advances in signal and image processing are leveraged to mine sub-surface defect information from TLT images.

This study aims to develop a fully automated TLT (A-TLT) data processing pipeline that is capable of detecting defects at varying depths under different environmental conditions. The framework is based on the time-varying response of sub-surface defects at different depths under varying ambient temperature variations. Analyzing the time-frequency distribution of a sequence of IR images could be used to characterize defects at varying depths from the surface. In the current study, a multiscale data analyses approach based on wavelet transform (WT) is developed to decompose ATLT datasets into narrow band time-frequency modes. These modes contain unique information that is subsequently used to isolate defects based on their depths from the surface. The key objectives of the current study are as follows:

(a) Develop a framework to fully automate time-lapse thermography data processing.

(b) Investigate IR camera sampling rates and sampling intervals necessary for carrying out time-lapse thermography.

(c) Perform a comparative analysis of the framework developed with traditional IRT approaches.

3-2 Related Works

There are two main schemes by which IRT is performed on structures: active and passive. Active thermography stimulates objects using an external heating or cooling source that creates enhanced thermal contrast that can be used to localize subsurface defects [45-47]. Passive thermography does not use an external heating or cooling source and relies on either changing environmental conditions such as diurnal temperature variations or heat generated by the object being observed.

Active thermography methods can be grouped into two main types, pulse or lock-in thermography, each of which is a form of TLT. Pulse thermography heats up an object with a short-duration, high-powered pulse. A recording of the thermal response of the surface during the cooling process is captured using an IR camera. Weritz et al. [48] and Maierhofer et al. [49] showed that sub-surface defects at varying depths could be extracted by analyzing the phase of the response image over time. Lock-in thermography uses a sinusoidal, mono-frequency heat source to excite an object while an IR camera simultaneously captures a sequence of thermal images. The pattern of heat dissipation from the surface of the object correlates with that of the input source. This property of lock-in is useful for denoising the thermal response

and subsequently improving the contrast between defective and non-defective regions beneath the surface.

Among the different types of active thermography, lock-in is known to be less sensitive to surrounding conditions such as air turbulence, reflections, etc. [3]. Similar to pulse thermography, Sakagami et al. [50] and Ranjit et al. [51] also illustrated that the phase (instead of the amplitude) of the thermal response contains valuable information for detecting defects. In general, active thermography has been most successful when used to extract defects in metallic and composite specimens. The development of active IRT methods for concrete has seen very little progress over the years. This is primarily due to the low thermal conductivity of concrete materials and the typical large size of the test objects (e.g., large concrete components such as a bridge deck) that require significant amount of energy to manipulate temperature change. There has been breakthroughs such as in Milovanovic and Banjad Pecur [52] whose approach was able to detect 4 in. depth defect after applying 100 min of heating. Other developments [53-55] in active thermography have also improved the detectability of defects beyond 3 in. from the surface.

Passive IRT for large structures typically observes the thermal behavior of material that has resulted from surrounding environmental conditions [46,

47]. It has been successfully used to identify internal voids [56], delamination, and cracks in concrete structures such as bridge decks [57], highway pavements [58], and pipelines [59]. Passive IRT remains the most common and successful scheme for defect characterization in concrete structures [60]. This is due to the uniform heating and cooling that results from diurnal temperature variations which can produce measurable thermal response from subsurface defects. Suman et al. [61] observed that under ideal environmental conditions defects at depths of 2 in. in the concrete can be detected. Washer et al. [1, 35, 44, 62] documented various environmental conditions and their corresponding influence on passive IRT methods used for inspecting bridge decks and soffits.

The depth of defects affects the magnitude of the thermal contrast and the time required for the contrast to develop [52]. Under ideal conditions, deeper defects tend to appear later in time and with less contrast than shallow defects [62]. However, depending on the environmental conditions, the same defect might show up at different times of the day. Hence, the time at which inspection is conducted is an important factor to be considered during passive IRT. Washer et al. [62] made recommendations regarding the ‘‘preferred” time periods for conducting IRT; 4–7 h after sunrise for defects expected to be 2 in. deep. Hiasa et al. [63] on the other hand indicated that night-time

inspections are preferred because temperature differences are most stable and relatively less noisy. These observations are, however, suitable for inspecting shallow defects.

For deeper defects, the preferred time period may not be known ‘apriori’ and is a different time than for shallow defects. Consequently, conventional IRT that captures a single image at a certain time is unlikely to detect both shallow (2 in.) and deep defects (3 in.) in the same image.

To overcome this challenge, Washer and Fuchs [64], Washer et al. [41] and Chase et al. [42] proposed TLT as a new method for passive thermography based on continuous imaging of surface temperature variations for an extended period of time. This approach eliminates the need to carry out inspections only during ‘‘ideal” conditions and also ensures that temperature variation signatures from deeper defects are captured. In Chase et al. [42], it was illustrated that TLT is capable of detecting defects up to 4 in. beneath the surface. There remains, however, open questions regarding the practical implementation of TLT for field inspection. For example, how often should images be acquired for TLT, and for what time interval? At high sampling rates and longtime intervals for data collection, the thermographer will have to deal with a lot of noisy information and the burden of ‘‘big data”. At lower

sampling rates or shorter sampling intervals, certain defects may be missed. Second, which images are relevant for localizing defects at different depths? The process of isolating or discounting images which lower the contrast between defective and non-defective regions is a challenging task. The traditional approach involves pre-selecting images based on known ambient conditions, followed by time series analysis to reconstruct a composite image that delineates the boundaries of sub-surface defects. For a largescale implementation of TLT, this step will require automation and robust algorithms to mine information critical for improving the detection of deeper defects.

3-3 Research Methodology

Figure (3-1) illustrates the methodology used to achieve the main objectives of this study.

Acquire IR datasets: the study acquired thermal images from a previous research [15, 44] with a resolution of 320 × 240-pixel display for each image.

Pixel-wise data pre-processing and manipulating: The acquired IR datasets are passed through a pre-processing engine to de-trend, normalize, and denoise the data. Several steps are conducted by transferring 2D images

into 1D signals which lets to calculate the envelope of maxima and minima, and in addition, the average for each signal.

1D Wavelet Transform: The temperature variation of each pixel in the IR image is decomposed into time-frequency modes which are subsequently mined to generate a single composite image using a series of image enhancement techniques. The purpose of using this approach is to remove the noise affecting the modes with high frequency. There are several driving mechanisms, such as wind, rain, fog, and shadow, that are impacting the high constructed thermal images. By decomposing these signals into their modes that correlate with all mentioned mechanisms, the noise will be removed, and defects will be mined to disclose their positions.

Reconstructing 2D high contrast images: The high thermal images are reconstructed by dividing the modes decomposed from each pixel in the IR images into three groups: high frequency component (MFC), medium frequency component (HFC), and low frequency component (LFC). Most of the information are stored in the MFC and LFC. The process removes the components under the HFC since it has the noisiest data. The final reconstructed thermal images for a specific course of time include only the MFC plus the LFC.

Sub-surface defect detection: A delamination localization (segmentation) engine based on active contour models was developed and used to automatically detect the boundary location of defects in the composite image. The model is also called Snake and it is basically represented by a chain of points wiggles through the image looking for high gradient of grey value of each pixel.

Performance analysis: The concept of signal-to-noise ratio has been adopted to evaluate the results with the traditional and conventional IR thermography. A modification has been done on the general equation by taking the ratio between the calculated and real areas of defects. Moreover, the TLT method has been compared to other method such as the 4-point thermography. The results showed that the TLT has more improved results.

The following sections provide a detailed explanation of the methodology.

3-4 Data Acquisition and Pre-processing

The data utilized in developing the methodology described herein consisted of IRT images collected during a previous study [15, 44]. A concrete block with 8 ft × 8 ft × 3 ft (2.4 m × 2.4 m × 0.9 m) dimensions was constructed

as shown in Figure (3-2). One face of the block was oriented toward the southern sky (‘‘sunny side”), representing a bridge deck or other component exposed to direct solar loading (i.e., sunlight). The other face of the block was oriented toward the northern sky where solar loading was never applied (“shady side”), which simulates the soffit area of a bridge deck. Four Styrofoam targets with dimensions 12 in. × 12 in. × 0.5 in. (305 mm × 305 mm × 13 mm) were embedded at depths of 1, 2, 3 and 5 in. (25, 51, 76 and 127 mm) from each face of the block.

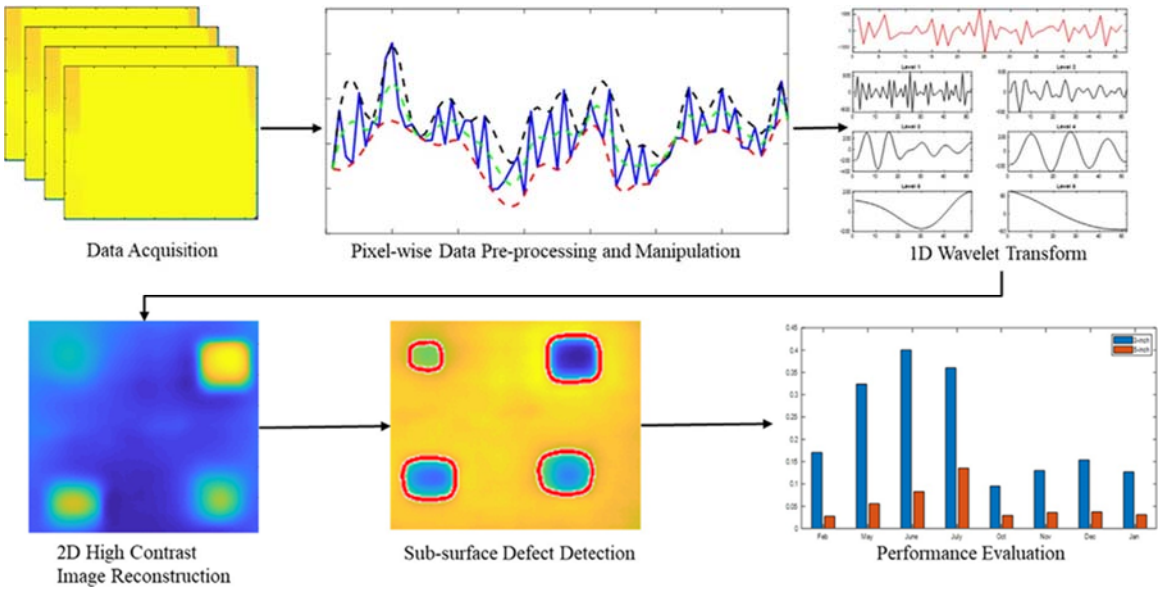

Figure 3-1: Schematic representation of the data processing methodology used in the research.

IRT images were captured using an uncooled microbolometer IR camera (ThermaCam Flir S65). The thermal camera has a thermal sensitivity of 0.08 °C at 30 °C and captured images using a 320 × 240-pixel sensor. Software (Therma Researcher Professional 2.8) was used to remotely control data acquisition parameters such as data sampling rate (1 snapshot every 10 min, 24 hrs a day), the duration of data collection, and to store the data on a computer hard drive. Data was collected over more than three months on both the sunny side and shady side of the block. Thermocouples embedded in the concrete were used to monitor the thermal gradient in the concrete and study variations in the internal temperature of the concrete block. Cables connecting the thermocouple to the data collection system can be seen in images from the sunny side of the block (see Figure 3-2). A weather station was positioned adjacent to the block and used to measure solar loading, wind speed, and temperature during data collection. The IR camera acquired data from the sunny side for months October, November, December into January, and moved to the shady side for months of May, June and July.

Examples of typical IRT images acquired during data collection are shown in Figure (3-2a). These data illustrate the contrast of conventional IRT images showing the simulated defects at depths of 1, 2, 3, and 4 in. in depth in the block. As shown in the figure, not all simulated defects can be observed

in the figures at all times of day. More shallow features have greater contrast and more well-defined shape than features at greater depths.

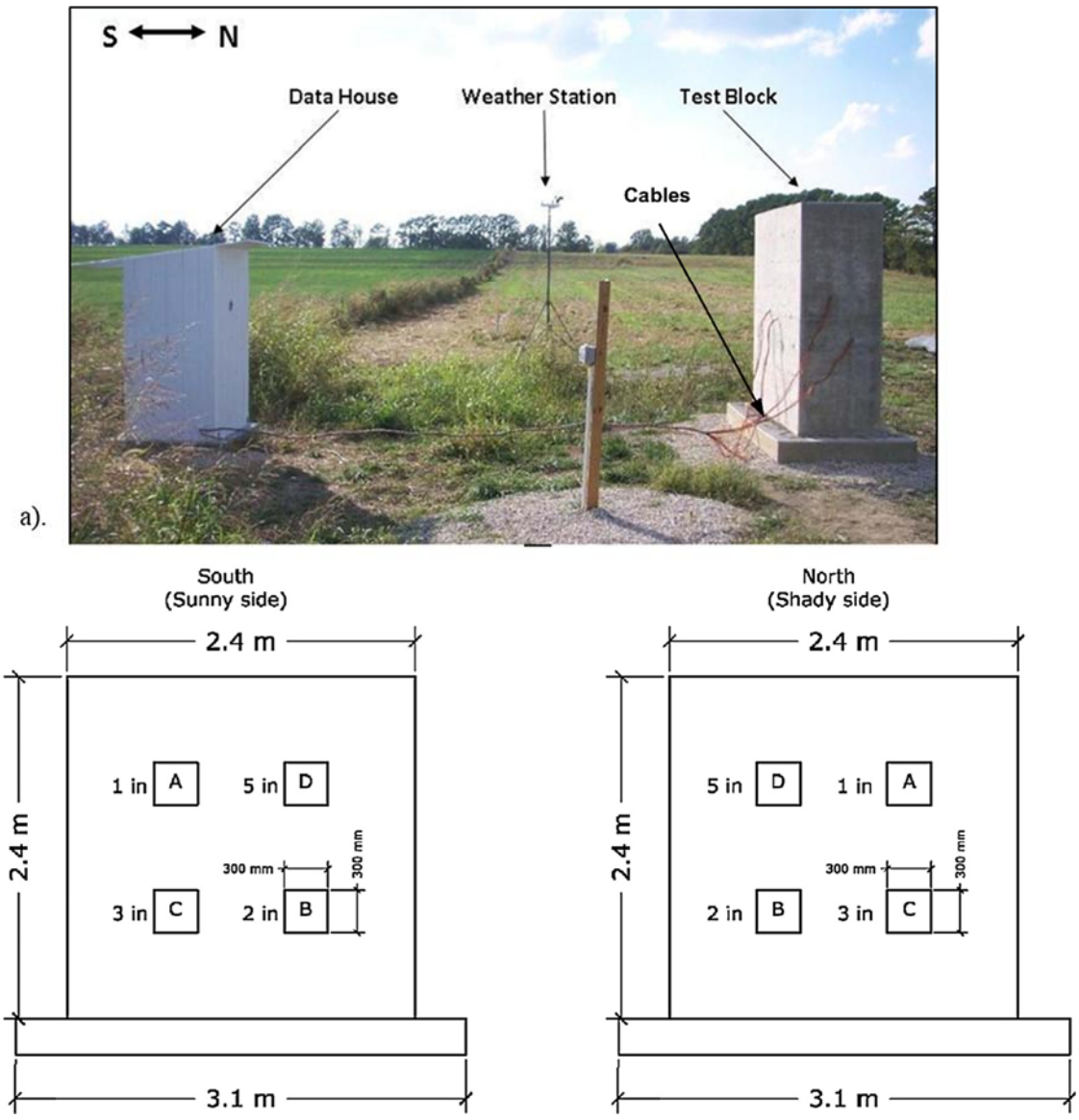

Figure 3-2: (a) Site layout and Concrete block with defect locations: (b) sunny side (south), (c) shady side (north).

All images acquired during the period of analysis were passed through a pre-processing routine where noisy information was detected and isolated. The process begins by first transforming 2D IR image snapshots into a 1D time series representing the temperature variation of each pixel in the image over the entire duration of the data acquisition. Next, the average temperature variation for each 1D signal is estimated using the maximum and minimum envelope as shown in Figure (3-3b). The average temperature variation is finally subtracted from the original 1D time series for each pixel location (Figure 3-3c). The result is a de-trended temperature variation for each pixel which is passed on to subsequent processes for analysis.

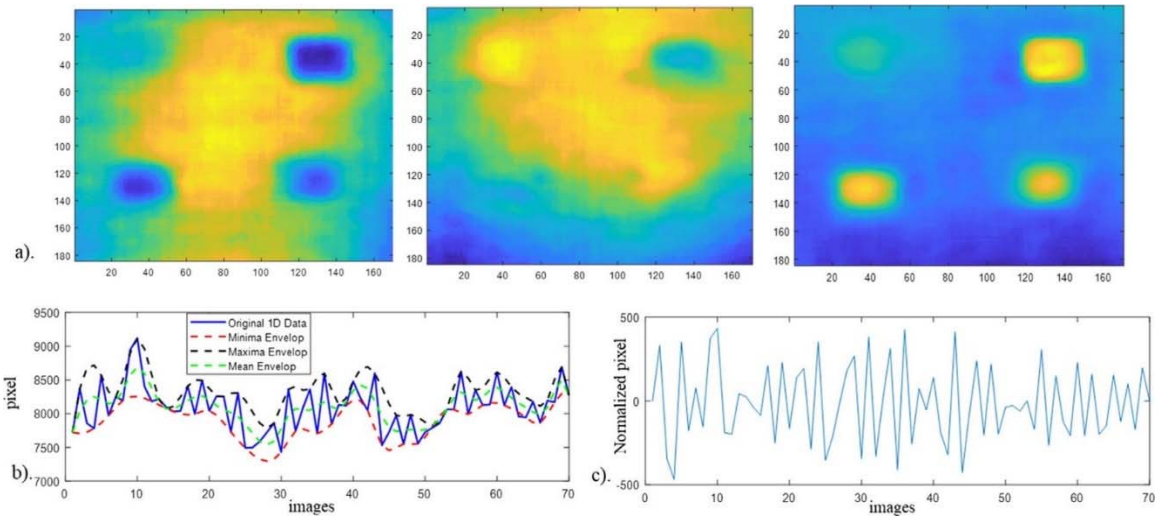

Figure 3-3: (a) Raw, unprocessed IR image snapshots at different time of the day. (b) Estimating average temperature variation using maxima and minima envelopes. (c) Detrended pixel temperature variation (subtract the average temperature variation from the original 1D time series data).

3-5 Multiscale Analysis of 1D Temperature Variations

The de-trended signal from the preceding section is affected by several mechanisms: variations in atmospheric temperatures, temperature variations due to surface or sub-surface defects and even random noise from rain, fog and shadows, etc. The goal of multiscale analysis is to analyze the internal structure of the detrended signal by decomposing it into a set of time-frequency distributions that correlates with all these driving mechanisms. Once the driving mechanisms have been isolated from each other, the components corresponding to sub-surface defects can be mined to detect their location.

Several data decomposition algorithms such as short-term Fourier transforms, Gabor filters, and empirical mode decomposition exist for extracting multiscale trends from data. However, temperature variations (obtained from passive thermography) are inherently nonstationary and, therefore, require highly adaptive algorithms to extract meaningful trends. The current study adopted the WT for analyzing the de-trended signal at different frequency scales. Wavelet Transforms operate at the scale of every oscillation and, are therefore, ideal for extracting localized defect information from time series data. Wavelet analysis has been widely applied in the areas

of nondestructive health monitoring [65], damage detection [66], incident management [67], and general signal processing. A summary of the WT is given below.

3-6 Wavelet Transform

The Wavelet Transform is considered one of the powerful mathematical techniques that was developed in the 1980s of the last century. The purpose of adopting this approach is by scheming signals of time-scales into frequency representations. It is an efficient tool that magnificently works with nonstationary signals, for example signals that stem from raw thermal imaged which are affected with several leverage factors, such as environmental circumstances. Another interest of the Wavelet Transform is by using different stretched band-widths, which allows the approach to do multiresolution analysis of the signals. Meaning that the method uses narrower bandwidth with high frequency signals in contrast with a border bandwidth with low frequency signals [68].

In the current research, the Wavelet analysis yields a time-frequency representation of a 1D signal by convolving it with a family of scaled and shifted basis functions. The total sum of a signal over time multiplied by

scaled, shifted version of the wavelet is called the continuous WT. The continuous WT function f(t) can be represented as [68, 69]:

$$W_f(S,T) = \int_{-\infty}^{+\infty} f(t)\, h_{ST}^{*}(t)\, dt = Re + j\, Im \tag{3.1}$$

where W_f denotes the WT, T is the translation factor, S is the scaling factor, Re is the real part, Im is the imaginary part, and h_{ST} is the daughter wavelet defined from the mother wavelet h:

$$h_{ST}(t) = \frac{1}{\sqrt{S}}\, h\left(\frac{t-T}{S}\right) \text{ and } h(t) = e^{j\omega t}\, e^{\left(-t^2/2\right)} \tag{3.2}$$

where ω_o provides the size of the Morlet wavelet h(t) chosen here as the mother wavelet.

An implementation of the continuous wavelet is designed as follows:

- Take a wavelet and compare it to the section at the start of the 1D de-trended temperature variation signal. Note the correlation coefficient is recorded throughout the time.
- Shift the wavelet to the right and re-compute the coefficient.
- Scale or stretch the wavelet and repeat the first preceding steps.
- Vary the scale of the wavelet and repeat all steps.
- Output the coefficients, frequency (scales), and time information.

MATLAB software was used to implement the WT. Figure (3-4) shows a wavelet decomposition of temperature variations of a single pixel in the IR image over a one-month period. The different scales shown in Figure (3-4) can be grouped into three classes: High, medium, and low-frequency components. Levels 1, 2, and 3 can be considered as high-frequency components (HFC). They capture short duration temperature variations at a scale of 1 cycle every 1– 15 min. Because HFCs have relatively very low energy (sum-square of amplitudes) and variance, the amount of sub-surface defect information that it captures is also low. The majority of information stored in HFCs is pure noise. Defects that are likely to be detected at these frequencies are those very close to the surface of the concrete block. The medium frequencies (MFC); levels 4, 5, 6, and 7 generally have the highest variance and energy, which means they store the most information about the sub-surface defects. From the figure, they capture hourly and daily temperature variations (1 cycle per hour – 1 cycle per day). Levels 8 through 13 can be considered as low-frequency components (LFM) (1 cycle for greater one day), also capturing relevant sub-surface defects due to the high levels of energy stored in them.

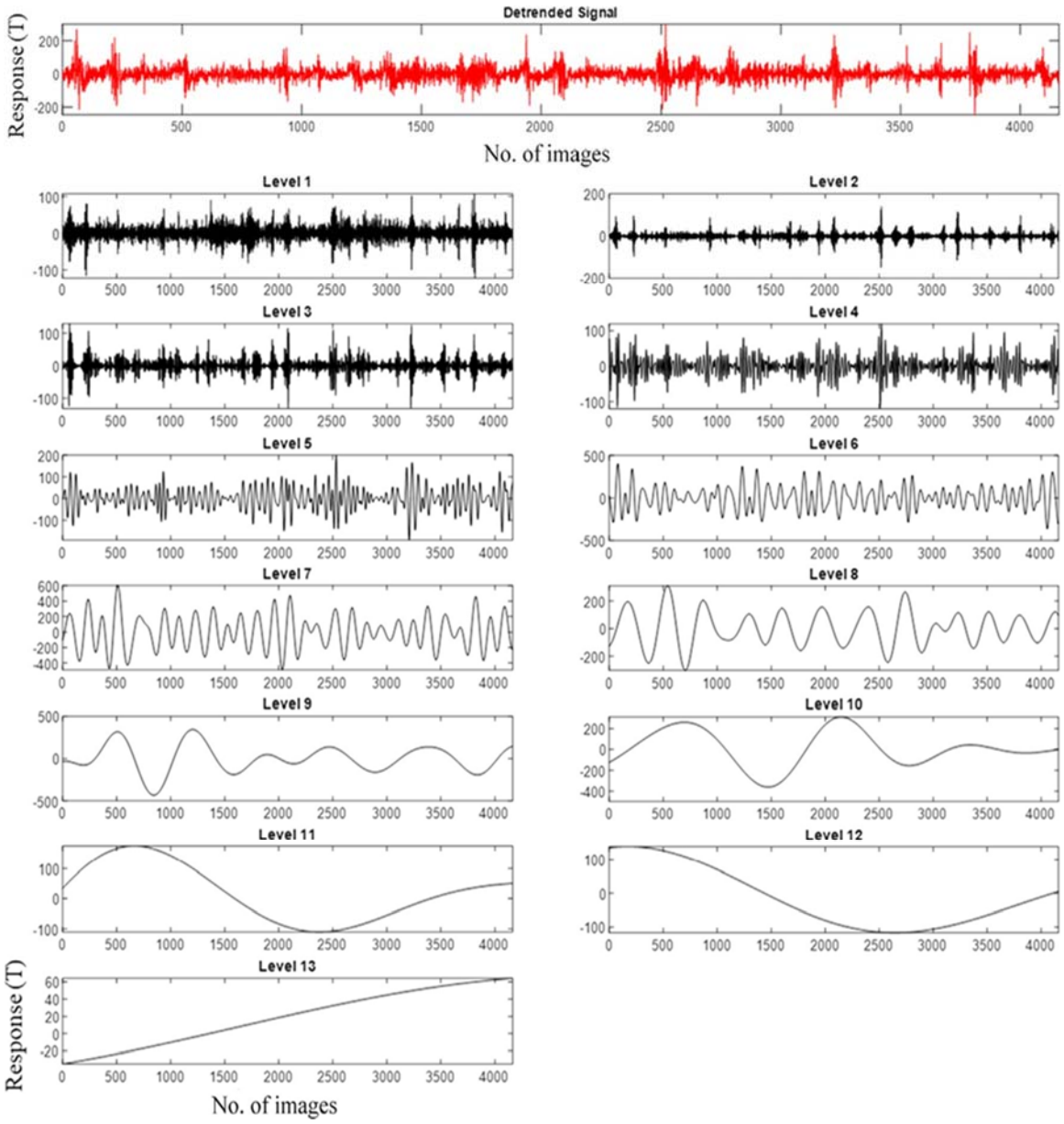

Figure 3-4: Graphs showing wavelet decomposition of IR image capture for one-pixel location during the month of February.

3-7 Signal Reconstruction

The goal of signal reconstruction is to generate a single composite image from all the snapshots (4320 snapshots a month) that accurately outlines all sub-surface defects. The algorithm in Table (3-1) is used to achieve this goal. For each pixel, a composite HFC, MFC, and LFC value is computed by subtracting the local maximum and minimum envelopes of the respective modes. Taking a log of the envelope difference serves as a smoothing function.

Figures (3-5a–d and e–h) show the reconstructed composite images for HFCs, MFCs, and LFCs on the shady and sunny sides of the concrete block respectively. As expected, the majority of information captured by the composite HFC image is noise. Although the edges of the 1–2-in. defects can be inferred from the image, the edges are not clear and, therefore, could be misinterpreted. Deeper defects are completely obscured at this scale. As shown on the color bar in Figure (3-5), the MFCs accurately captured information on 1–2-in. depth defects with a maximum pixel intensity of approximately 895 and 110,000 on the shady and sunny sides respectively. The 3-in. depth defects are also visible at this scale at a relatively lower intensity. The composite image at this scale has removed most the noise and

transient temperature variations that were obscuring detection of sub-surface defects. The LFCs, on the other hand, emphasizes deeper defects (3–5 in. beneath) more than shallow ones as shown in Figures (3-5c and g). These results reveal the essence of multiscale decomposition; the ability to extract defect information based on the depth is invaluable. Figures (3-5d and h) display the final composite image which sums up the MFCs and LFCs. All defects within 5 in. from the surface are clearly outlined although their geometric shapes have morphed into circles instead of squares. From the composite image on the sunny side (Figures 3-5h), it is also important to note the effective removal of noise introduced by the temperature sensing wires. A visual comparison of the composite images in Figures (3-5d and h), makes it clear that, although the maximum temperature difference is observed on the sunny side, the shady side appears to have a higher contrast between the defective and non-defective region relative to the sunny side.

Table 3-1: Signal Reconstruction

1. Group decomposition results into HFCs, MFCs and LFCs.
2. For each pixel location $I(x, y)$ in groups HFC, MFC and LFC:
   (a) Construct a maximum E_{max} and minimum envelop E_{min}
   (b) Subtract the minimum envelop from the maximum to obtain the E_{diff}
   (c) Find the extremas of E_{diff} and compute the slope between the extremas.

$$E_{slope} = \frac{k_{i+1} - k_i}{\Delta t} \tag{3.3}$$

where k designates a series of extremas, and Δt, the time difference between two successive extremas.

   (d) Sum up the log of slope over time to obtain the reconstructed value for each pixel.

$$I_{rec}(\mathrm{x}, \mathrm{y}) = \sum_t \log(E_{slope}) \tag{3.4}$$

3. Output $I_{rec}(\mathrm{x}, \mathrm{y})$

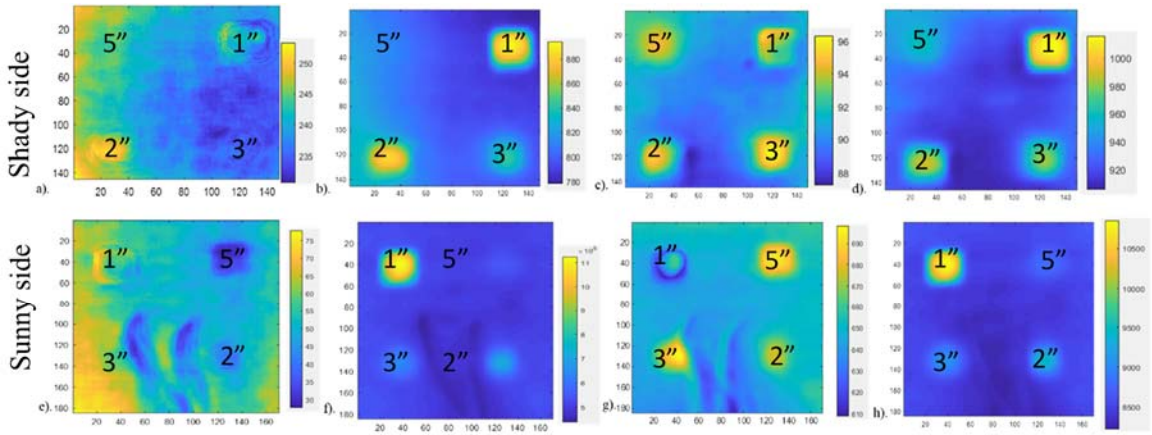

Figure 3-5: Signal Reconstruction from: (a) HFVs. (b) MFVs. (c) LFVs. (d) Sum of MFV and LFV Composite Images from the shady side. (e) HFVs. (f) MFVs. (g) LFVs. (h) Sum of MFV and LFV Composite Images from the sunny side.

3-8 Sub-surface Defect Boundary Extraction

The final stage of the framework is to automatically extract the boundary location of defects captured in Figures (3-5d and h). Traditional edge detectors and thresholding algorithms have been widely used for automating damage detection in images [70]. These algorithms generally work by setting the grey value of each pixel in the image to a value that is dependent on the magnitude of the gradient of the grey level at the corresponding point in the original image. The concept of an edge is far more than the presence of a high gradient at a particular location; it highly depends on the spatial distribution of these high and low gradient points across the image. An edge detector, however, does not explicitly possess the capability of identifying the distribution of the gradients. Any regions with high gradients are detected, whether they are edges or noise. In this study, instead of relying on tradition edge detection systems, a model-based alternative called Active Contour is employed to automatically extract the exact location and geometric parameters of the boundary of the sub-surface defect.

3-9 Active Contour Models

Active contours, also called snakes, belong to a class of model-based methods for representing the edges or boundaries of image features. They consist of energy minimizing deformable splines, influenced by constraint and image forces which pulls it towards object contours or boundaries. First introduced by Kass et al. [17], the technique has gained much popularity since then. It has been used in a variety of applications including bio-medical image analysis [71], traffic sign recognition [72], pavement and rail distress image analysis [73]. The snake can be thought of as an elastic band of arbitrary shape, represented by a chain of point that wiggles in the image towards regions of high image gradient distribution. So, the edge pixels must "pull" the snake points. The stronger the edge, the stronger its pull on the snake points. Active contours are broadly classified into two main groups: the parametric active contour model and the geometric active contour models. Parametric models represent the active contours explicitly as parameterized curves. In geometric models however, they are represented as level sets of a two-dimensional function that evolves in a Eulerian framework. It is able to break or merge naturally during evolution. This helps it to handle topological changes very well. A detailed analysis of the algorithm can be found in [61, 74]. The level set algorithm developed in [75] is implemented in this study.

The evolving level set function is approximated to a signed distance function. Equation (3.5) is used as a metric to characterize how close a function is to a signed distance function.

$$P(\varphi) = \int \frac{1}{2}(|\nabla\varphi| - 1)^2 dxdy \tag{3.5}$$

The snake is influenced by two types of forces.

- The Internal Energy (E_{int}): Also called the bending energy of the curve. It preserves the snake (keeping it smooth) as it is being pooled by image forces.

$$E_{int} = \mu P(\varphi) \tag{3.6}$$

where μ is a parameter controlling the effect of penalizing the deviation of from a signed distance function.

- The External Energy (E_{ext}): The force that moves the snake points or zero level curve. It is dependent on the edge strength at a point; the stronger the edge, the stronger the pull. The external energy is supposed to be minimal when the snake is at the object boundary position. We designate this energy as:

$$E_{ext}(\varphi) = \lambda \int g\delta(\varphi)|\nabla\varphi| dxdy + v \int gH(-\varphi) dxdy \tag{3.7}$$

$$\delta(\varphi) = \begin{cases} 0 & |x| > \varepsilon \\ \frac{1}{2}\left[1 + \cos\left(\frac{\pi}{\varepsilon}\right)\right], & |x| \leq \varepsilon \end{cases} \quad (3.8)$$

$\lambda > 0$ and v are constants, δ is the univariate Dirac function, and H is the Heaviside function. The total energy E_{total} can therefore be defined as:

$$E_{total}(\varphi) = \mu P(\varphi) + \lambda \int g\delta(\varphi)|\nabla\varphi|dxdy + v \int gH(-\varphi)dxdy \quad (3.9)$$

3-9-1 Active Contour Implementation Steps

The performance of active contour models hinges on three main steps: the type of contour specified, parameters defined for contour initialization and the maximum number of contour iterations. The implementation steps adopted in the current study is described as follows:

Specifying the Type of Contour: rectangular and circular shaped contours are the most common type of contours frequently used. Circular shaped contours are preferable for scenes where the shape of the object of interest is not known a-priori. In this study, rectangular shaped contours were specified since it matched the shape of the sub-surface defects of interest.

Defining Parameters for Contour Initialization: the size of the contour and its proximity to the defect location is one parameter that can marginally influence the performance of the active contour model. If the contour is initialized far aware from the defect, it may not be attached to the defect boundary when the maximum number of iterations is reached. To ensure that contours are initialized at the right location, we developed an automated approach for contour initialization shown in Table (3-2). The algorithm uses the number of local minimum from the reconstructed image to determine the number of contours to be initialized. This is followed by a horizontal and vertical projection of image pixels to determine the size of each contour. Figure (3-7) shows initialized contours for the composite image.

Table 3-2: Active Contour Initialization

Step 1: Use an $m\ by\ n$ filter to find the local minimums in the reconstructed image. A pixel value is minimum if it is lower than all its neighboring pixels within the $m\ by\ n$ filter. The number of contours to be initialized is set to equal the number of minimums detected.

Step 2: Project image pixels $f(I, j)$ column-wise and row-wise onto a horizontal H_{AC} and a vertical accumulator V_{AC}:

$$H_{AC}(j) = P[f(:, j)], \text{ and } V_{AC}(i) = P[f(I, :)];$$

where P is the sum operator in this case. I and j are the row and column index respectively.

Step 3: Compute the first derivate for each accumulator and detect all zero crossings as shown in Figure (3-6).

Step 4: The distance between the first and last zero crossing for each signal defines the width or height of the contour, whereas the second zero crossing corresponds to the contour's centroid.

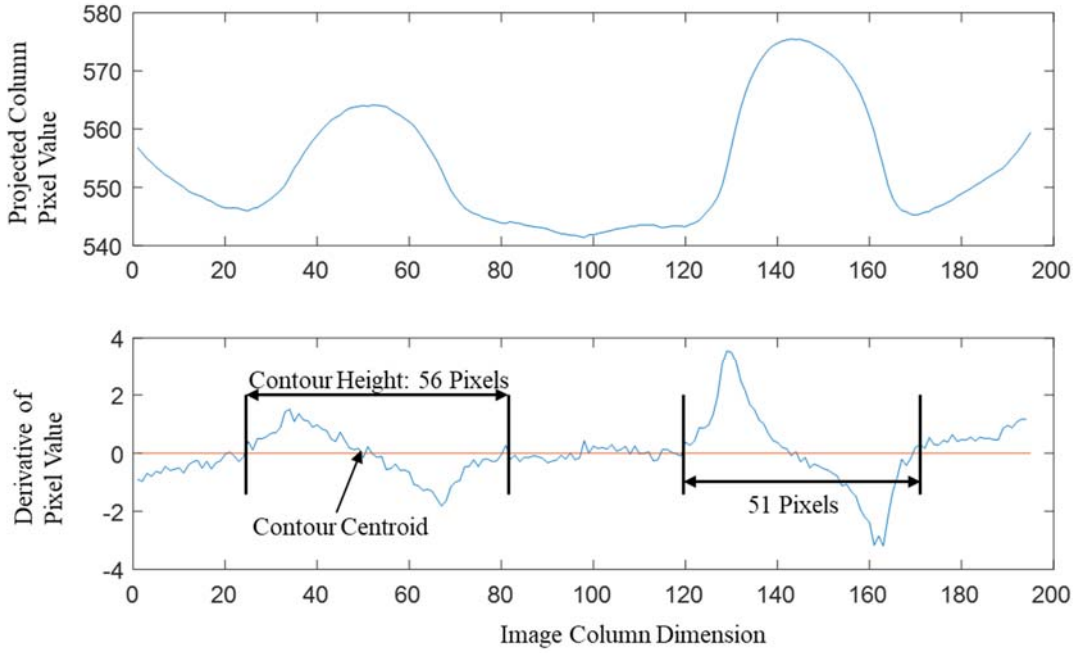

Figure 3-6: Estimating the width and height of contour.

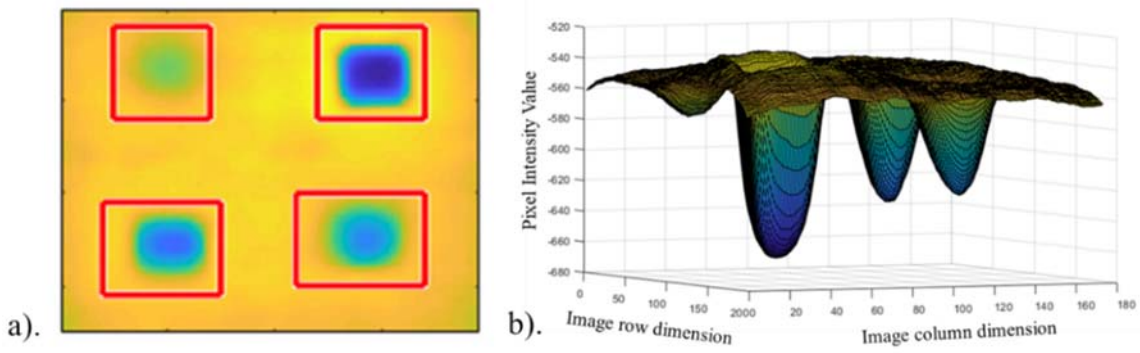

Figure 3-7: a). Specifying Contour Type and Initialization. b). Defining Image Minimum.

Determine maximum number of iterations: as explained previously, the contour moves by an external force driven by the image gradient. The contour

stops evolving when equation (3.9) is minimized or when the contour is attached to the edge of the image feature. However, in cases where the image contains multiple features, the evolution of the contour must be constrained by the maximum number of iterations parameter. Setting this parameter low could lead to incomplete feature boundaries. Figure (3-8) below shows three different stages of contour iteration toward an image feature until exact boundary is extracted. In this study, the maximum number of iterations is adaptively selected using the relation in equation (3.10). From the equation, the number of iterations is correlated with the feature with the strongest gradient. The stronger the gradients in the image, the higher the number of iterations and vice versa.

$$I_p = k * \left[\frac{\sum_{\forall r}\sum_{\forall c} x_p}{max[\sum_{\forall r}\sum_{\forall c} x_k]^{k=1:n}}\right] \tag{3.10}$$

where I_p is the maximum number of iterations (capped at 500 in this study), k is a constant set to 500, r and c are rows and columns x_p contains all the image pixels defined by contour initialization height and width and x_k image pixels for all features in image.

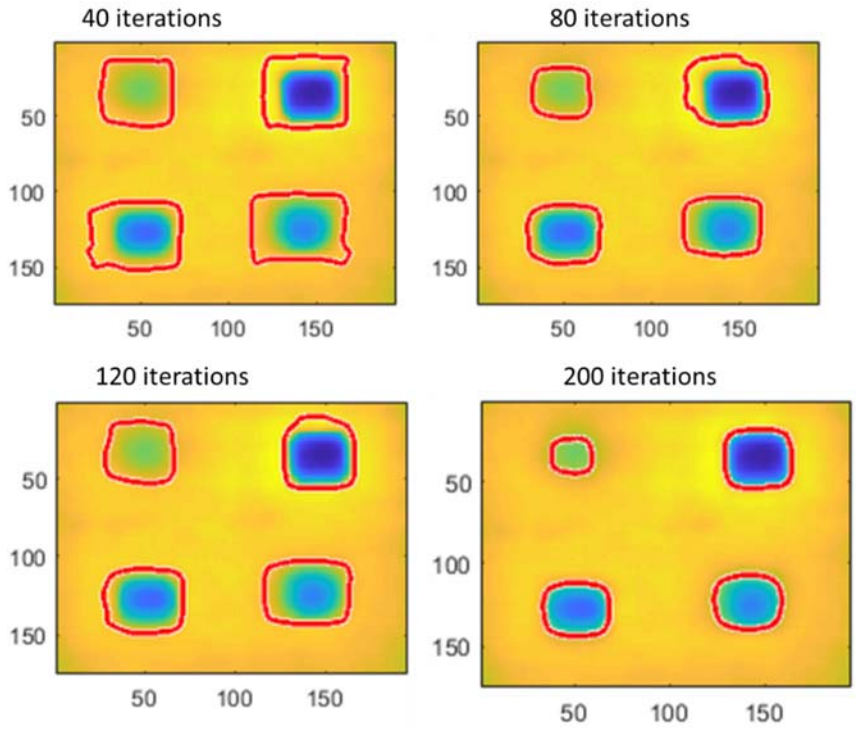

Figure 3-8: Evolution of Contours toward image feature boundaries.

Without any manual interventions, the number of defects in the image can be extracted by counting the number contours initialized; the depth of the defect could also be inferred based on the multiscale analysis. The size of the contours reveals the extent of subsurface damage in the concrete, a key factor in decision-making regarding preservation, repair, and replacement of bridge decks.

3-10 Performance Evaluation and Discussion of Results

The performance of the developed framework is evaluated based on defect size detection accuracy and the amount of contrast enhancement between defective and non-defective regions of a TLT processed image.

To evaluate the defect detection size accuracy, we compared the ratio of the area of defect extracted by the framework to the actual or expected area of the defect. Assuming that there were no geometric image distortions during data acquisition, the original dimensions of the block specimen (2.4 m × 3.1 m) and defects (300 mm × 300 mm) were transformed into pixel areas. The TLT algorithms were then used to process IR data acquired at different time periods. The final size of the contours extracted for each day were compared to the true size of the defects and reported in Table (3-3). From the Table, although there are obvious discrepancies in the size of defects extracted by the TLT framework, the reported sizes are detectable. For example, for 5-in. depth defects, about a quarter to have of its size (depending on atmospheric conditions) could be seen on TLT processed images.

Table 3-3: Defect size detection accuracies.

Defect depth	Detection size accuracy
1 in.	0.84–0.96
2 in.	0.77–0.88
3 in.	0.71–0.81
5 in.	0.18–0.46

To evaluate the performance of the proposed TLT framework based on contrast, we defined a quantitative measure of contrast enhancement which is influenced by two main parameters: The size of the defect in the processed image compared to its original (known) size and the pixel intensity of the defective area compared to its immediate surroundings. The result is a modified version of signal-to-noise (SNR) [76, 77] ratio designated as follows.

- Consider the defective and non-defective regions as signal (S_{area}) and noisy (N_{area}) area respectively as shown in Figure (3-9). The defective region is extracted from the final location of the active contour, whereas the non-defective region is the area surrounding the identified defective region.
- Compute the contrast measure (mSNR) for the processed image using equation (3.11).

$$mSNR = 20log_{10}\left[k * \left[\frac{abs\left(\frac{1}{m*n}\left(\sum_{m,n} S_{area} - \sum_{m,n} N_{area}\right)\right)}{\sigma_{noise}}\right]\right] \tag{3.11}$$

where $k = v/V$; v is the size of defect extracted by the active contour and V is the known size of the defect. m and n are the dimensions of the image, σ_{noise} is the standard deviation of the noisy area.

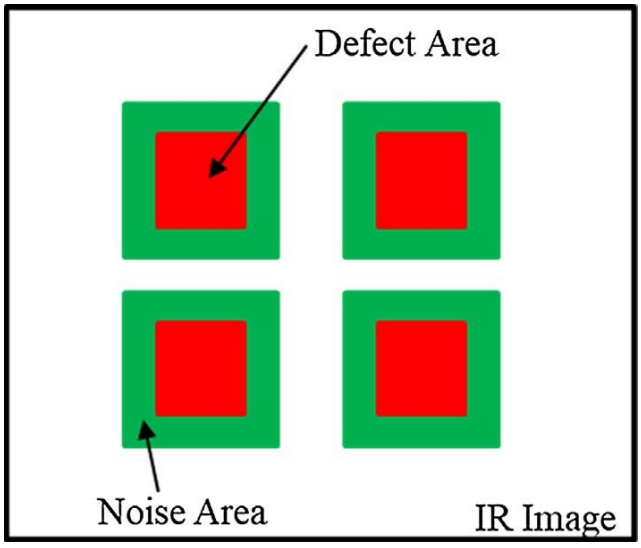

Figure 3-9: Schematic diagram showing the defect areas and surrounding noise areas used for SNR calculations.

IR Data were analyzed using the contrast measure developed to address two key questions regarding the application of the framework developed. First, how often should images be acquired, i.e., what sampling intervals should be used during data collection. Second, given a selected sampling interval, what is the appropriate data collection period be, i.e., how long should data be collected. The effect of the time of year when data was collected and also analyzed.

3-10-1 Sampling Interval

The influence of the camera's sampling rate was investigated using 5 different sampling intervals. The data utilized in the study was collected at a sampling interval of 10 min; additional sampling intervals of 1, 3, 6, and 12 h were analyzed by sampling the available data at the appropriate times. Figure (3-10a–c) shows the normalized contrast for simulated defects at depths of 1, 2, 3, and 5 in., for data collection intervals of 24 hrs (Figure 3-10a), 1 week (Figure 3-10b) and 1 month (Figure 3-10c). A normalized contrast of 0 or less means the defect cannot be detected visually in the image. As shown in the figure, simulated defects at depths of 1–3 in. were detectable using any of the selected sampling intervals; using a smaller sampling interval generally improved the contrast between defective and non-defective regions.

3-10-2 Data Collection Period

The analysis indicated that simulated defects that were 1–3 in. beneath the surface were detectable with only 24 hrs of data collection, as shown Figure (3-10a). At a sampling interval of 10 min, even 5-in. deep defects could be detected using a 24-hr data collection period, although at very low contrast.

Figure (3-10b) and c show that the contrast for a 5-in.-deep defect was improved when the data collection period lasts for 1 or more weeks.

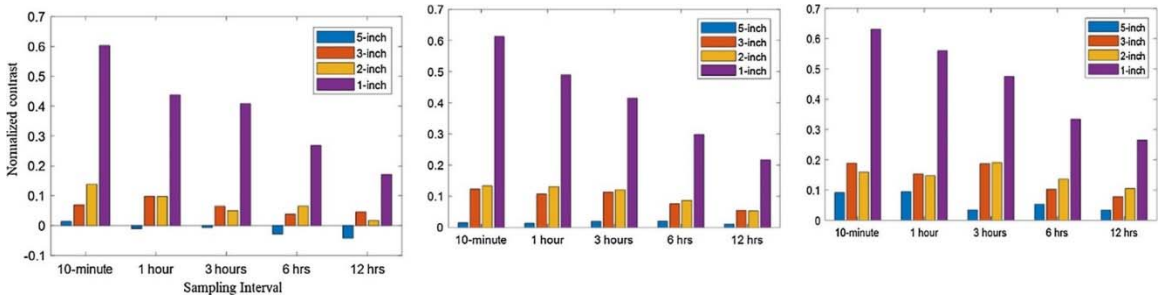

Figure 3-10: Graphs showing average normalized image contrast using IR images acquired over a period of (a) 24 h. (b) 1 week. (c) 1 month.

3-10-3 Inspection Timing

Figure (3-11) shows that defects within 5-in. from the surface can be detected with the proposed framework irrespective of the month the inspection was carried out. However, the amount of contrast observed for 3- and 5-in. defects will vary; hotter months appear to have a higher contrast compared to colder months. The IR camera was in position on the shady side between February and July and on the sunny side between October and Jan. As explained earlier, imaging from the shady side generates higher contrast images as compared to imaging on the sunny side. The explanation for these results may be that the longer days during February-to-July (shady side) as

compared with October-to-January (sunny side) provide more thermal contrast.

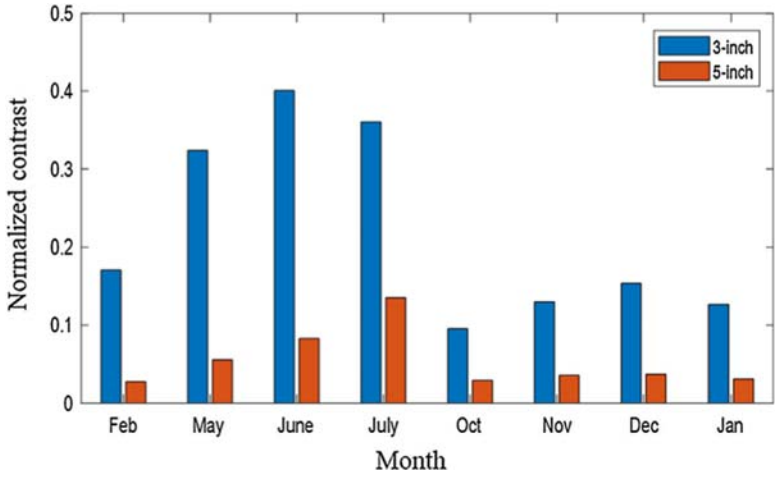

Figure 3-11: Average normalized image contrast by month for 3- and 5-in. defects.

3-11 Assessment of the A-TLT Methodology

A comparison of the SNR for the A-TLT processed data with lock-in thermography and conventional IRT data was completed to assess the performance of the A-TLT processing. Conventional lock-in thermography is used for active thermography where the characteristics of the external heat source is known. To implement the lock-in algorithm for passive thermography, the maximum temperature response from a non-defective location was used to approximate the external heat source, also called the reference signal. This was followed by a correlation process which simply multiplies the reference signal to temperature variations from every pixel. The

resulting data were then processed using a four-point method. The four-point method is a popular technique for extracting sub-surface defects in materials using lock-in thermography. The method requires only 4 snapshots of the specimen to be captured during the heating and cooling cycle. Phase and amplitude image are then reconstructed from the snapshots using equations (3.12 and 3.13) below [3, 78, 79].

$$\phi(x,y) = \tan^{-1}\left(\frac{S_1 - S_3}{S_2 - S_4}\right) \tag{3.12}$$

$$A(x,y) = \sqrt{(S_1 - S_3)^2 + (S_2 - S_4)^2} \tag{3.13}$$

where S_1, S_2 and S_3, S_4 corresponds to concrete block temperatures during heating and cooling cycles respectively. Table (3-4) summarized the process used to implement lock-in for passive thermography.

Table 3-4: Lock-in for passive thermography.

1. Heat-source or reference signal approximation: For all images, find non-defective region with maximum temperature response.
2. Denoising: Convolve each pixel's temperature variation with the approximated reference signal to amplify variations correlating with the heat source.
3. Four-Point: Apply four-point method and extract phase and amplitude images using equations (3.12 and 3.13).
4. Output: Select amplitude or phase image with highest contrast between defective and non-defective regions for comparison.

Either the phase or amplitude image can be used to visualize the sub-surface defects. Figure (3-12) shows the results of using the four-point method to process IR images acquired on the shady and sunny sides. The processed images shown were obtained by applying equations (3.12) and (3.13) above to four images which maximized the contrast between defective and non-defective regions. From the figure, 1–3-in. defects are easily distinguishable whereas 5-in. depth defects cannot be seen. Comparing Figure (3-12a) and d also illustrates qualitatively that the A-TLT processing produced greater contrast between defective and non-defective areas, suggesting that A-TLT had improved denoising capabilities as compared to the four-point-snapshot approach.

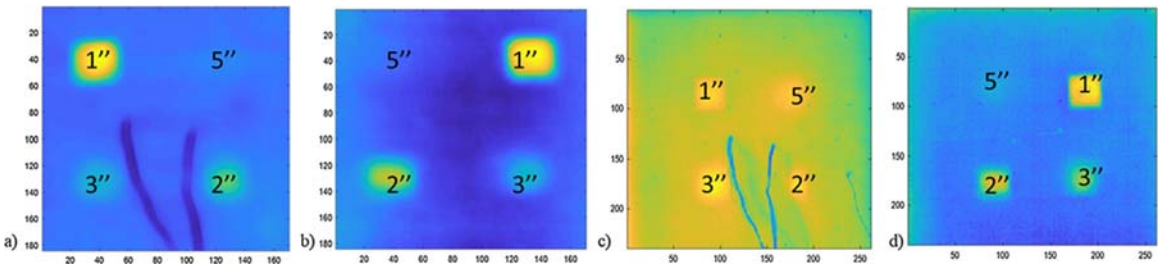

Figure 3-12: Images produced from the four-point method showing (a) Lock-in – Sunny Side. (b) Lock-in – Shady Side of the concrete block. (c) Conventional – Sunny Side. (d) Conventional – Shady Side.

To illustrate the improvements of the A-TLT processing as compared with conventional IRT and the four-point TLT method quantitatively, an analysis of one month of data was completed and is shown in Figure (3-13).

The normalized contrast between 3 and 5-in. deep simulated defects and sound areas of concrete was determined for each method based on the calculated SNR. A positive normalized contrast means the defect is visually distinguishable in the images produced. Conventional IRT data were determined from raw IR images that produced the greatest contrast for the 3 and 5-in. depths. In other words, these data represent the maximum contrast values determined from conventional IRT during the month, as determined from visually inspecting all of the images acquired during the analysis period. Data for the four-point method were determined for each diurnal temperature cycle during the month.

In general, it can be observed that the average normalized contrast for defects detected with the A-TLT increases with time whereas those observed with the four-point approach are unstable because they are heavily influenced by diurnal temperature variations. The figure shows that both methods were able to detect 3-in. defects on all days in July. The contrast observed using A-TLT is approximately double that of the four-point approach. For defects 5 in. beneath the surface, the A-TLT provided significantly increased contrast as compared with the four-point method. The contrast for the A-TLT ranged from 0 (during the first 3 days in July) to 0.18 (by the end of July). The generally increasing trend over time emphasizes the benefit of continuous

imaging for IRT. In fact, after 15 days of continuous imaging in July, the contrast for 5-in. defects using A-TLT is comparable to the contrast for 3-in. defects using the four-point approach. From the figure, 5-in. defects are not easily detected using the four-point method. The normalized contrast is negative on most days.

Comparing A-TLT to the conventional IRT, it can be observed that it takes about 10 – 14 days for the A-TLT method to produce an image with comparable contrast to the maximized conventional IRT image. After 14 days, the A-TLT slightly edges past the baseline. This is once again evidence of superior denoising capabilities of the proposed framework.

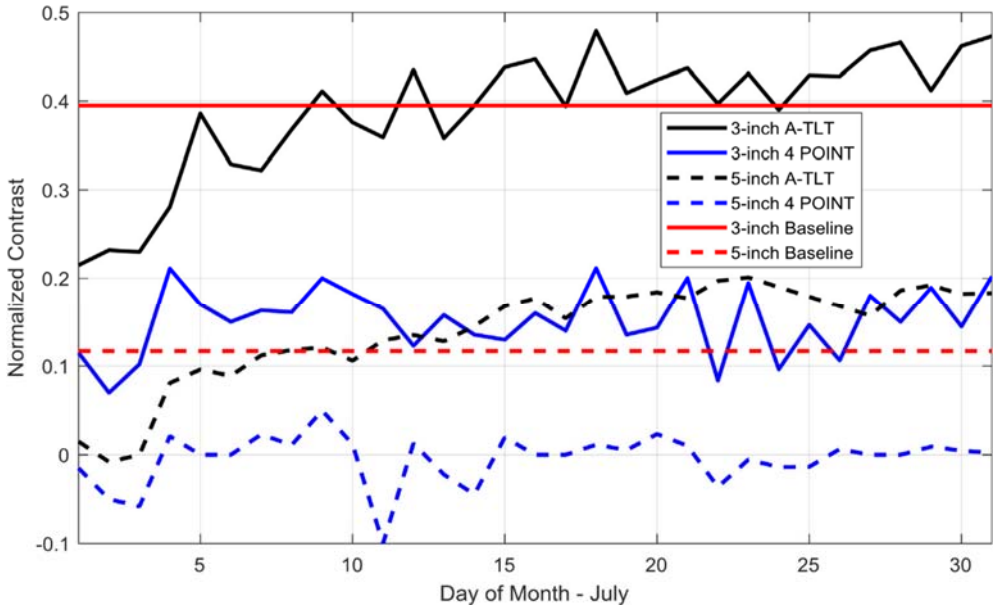

Figure 3-13: Comparison of proposed framework (A-TLT) with the four-point method based on daily contrast for 3- and 5-in. sub-surface defects in the month of July.

CHAPTER FOUR

4- DETERMINATION OF DEPTHS IN DELAMINATION IN REINFORCED CONCRETE STRUCTURES BY USING MACHINE LEARNING

4-1 Background

With the extensive numbers of concrete bridge decks in poor structure conditions, highway foundations have an increased necessity to evaluate their conditions which leads to optimize the timing and scope for preventive maintenance [80] to evaluate the durability and serviceability of these bridges before they become risky and costly. For that reason, it is essential for detecting and predicting defects in concrete bridge decks in order to determine accurately the structural state of concrete components to suggest a proper renovation technique for possibly damaged parts in the concrete bridge decks. Several reasons have led to cause or create defects inside concrete decks. Deterioration factors, such as an excessive traffic loading, weather conditions, cycles of freeze-thaw, shrinkage, thermal effects, and corrosion of reinforcing rebars, cause cracks, air voids, delamination and spalling [26]. These bridge deck deteriorations often occur below the deck surface and become difficult

to be evaluated by visual means [19]. Furthermore, delamination is shaped from hidden cracks inside the concrete components and is initiated at reinforcement rebar layers (top or bottom) or even at region between reinforcement rebar layers [81, 82]. On the contrary, sub-surface delamination might be detected by using visual examination, which mainly depends on experience of inspectors [12]. Consequently, the visual inspection might not give clear decision-making relating to maintenance, repairing and replacement.

To detect this delamination potentially, nondestructive testing (NDT) is used and has the ability to reveal these defects (i.e., areas of delamination) by employing techniques such as manual sounding (chain dragging and hammer sounding), impact echo (IE), ultrasonic, and advanced methods, like ground penetrating radar (GPR) and infrared thermography (IRT).

However, there are two main approaches that are employed by the IRT: the active and the passive thermography. The active thermography mainly utilizes objects that are simulated by a heating or cooling source such as halogen lamps or electrical heaters as a thermal excitation for detecting delamination in concrete structure components [45-47]. Unlike the active thermography, the passive thermography utilizes the natural solar as a heating

or cooling resource such as diurnal temperature or a heating that is generated by an object itself such as machines [24, 83].

The components of reinforcement concrete structures commonly have low diffusivities than metal materials. For that reason, a thermographic testing needs more time for heating up concrete specimens and testing record. Moreover, it is difficult to ensure that the heating up over a specific time is practically homogeneous because the wide size of specimens being inspected. Consequently, the concrete buildings are considered as non-homogeneous structures since they have voids, cracks and reinforcement and that what makes the use of active thermography in civil engineering is less than other majors, for example the aerospace industry and mechanic engineering [53].

During the last few decades, the active thermography has been widely employed for detecting anomalies like voids or defects in metals, plastic, and composite materials. Nowadays, the active thermography has demonstrated to be an outstanding technique to qualify (the location) and quantify (the depth) of delamination in reinforced concrete structures [54, 55, 81, 84, 85].

From previous researches, most developed methods in the active thermography, on estimating depths in defects, are as a function of phase contrast ($\Delta\phi$), frequency (f), thermal contrast (ΔT), time (t), and material

properties of specimens being inspected, for example the thermal diffusivity length [49, 53, 86].

The active thermography tests are held under controlled environment conditions, such as the frequency of the test, intensive of heating subjecting on inspected materials, the distance between a heating source and a specimen being tested, … etc. In active thermography, several models have been adopted to calculate the quantitative delamination in concrete structures such as pulsed phase (PPT) [87, 88] and lock-in (LIT) thermography.

Likewise, the passive thermography has manifested an excellent method for investigating delamination in concrete structures. The previous mentioned models in the active thermography proved to be incompatible with the passive methodology to predict depths in delamination in the reinforced concrete structures.

In the current work, the passive thermography has been used to predict depths in delamination since the concrete bridges are exposed to direct solar energy and ambient temperature changes. Parameters, like solar heating, daytime and nighttime, wind speed, clouds, and shadows, are affecting on the process of passive thermography. For these reasons, machine learning (ML) has been proposed as an alternative method for the quantitative analysis to

detect depths in defects in the concrete structure components. However, an analysis approach called the Fast Fourier Transform (FFT) has been taken into consideration to assist in excerpting features from the thermal raw data, for instance phases, frequencies, and amplitudes. The concept of the machine learning works by training and testing the extracted features of the defect and sound areas in the concrete specimens. The proposed methodology has shown a good accuracy by employing different algorithms like support vector machine (SVM) and k-nearest neighbor (KNN) which will be discussed later in this research. The objectives of the current study could be summarized as follows:

(a) Developing an algorithm to fully calculate phases, amplitudes and frequencies and extract features from the delaminated and non-delaminated areas.

(b) Proposing classifier learners such as SVM and KNN to build predictive models to estimate depths in delamination.

(c) Conducting a comparative analysis of different Machine Learning models for depth prediction.

4-2 Related Works

Infrared thermography adopts two main approaches depending on the heat resource: active and passive thermography. In active thermography method, a surface of specimen object is artificially subjected by an external heating stimulus, such as halogen lamps, flash lamps, electrical heaters, ultrasonic excitors [18], while, the heat in passive thermography approach is naturally applied by using solar source that comes from sun or a cooling process during nighttime [18].

Active thermography has been extensively proposed to quantify defect depth in metal and composite materials [89]. The first study on defect quantification in reinforced concrete structures had been done by Maierhofer et al [49, 90] and Meola et al [91]. Maierhofer et al [90] studied a quantitative analysis on a concrete block with dimensions (1.5m x1.5m x0.5m). A computer program based on finite element differences method was adopted to stimulate the heating up and cooling down. An inverse solution was used depending on maximum temperature difference which had been determined from experimental tests. Another research had been accomplished by Dumoulin et al [87] in 2010 to estimate defect depths in a concrete block. Pulsed phase thermography (PPT) had been used since a direct relationship

exists between depth (z) and thermal diffusion length (μ) [92]. A considerable error was obtained between the calculated and real depths, which was attributed to the estimation of using the thermal properties of defect materials [87]. A number of stimulations was completed by Cotic et al [53] depending on experimental tests. The model was developed by employing the sizes of defects. A quadratic relationship had been used between the depth of defect (z_{def}) and the time (t_{max}) or the frequency (f_{max}). In 2006, Arndt et al [88] used pulsed-phase-thermography (PPT) to adopt an equation which was mainly established on the maximum phase contrast, blind frequency, thermal diffusivity of the inspected specimen and a correlation factor. Furthermore, an experimental test was fulfill by Huh et al [84] on a concrete block which has delamination with different areas and depths. The authors adopted a relationship between observation times and defect depts as $t=z^2/\delta$, where δ is the thermal diffusivity of materials being tested. The time (t) in the previous relationship could be illustrated as the time that could the absolute contrast (ΔT) stays constant or gets to the maximum value after the heating up process. In 2017, Milovanovic et al [93] had employed an empirical expression that is driven from a solution of a heat flux [94] as illustrated below:

$$D = \sqrt{(\propto_{diff} \ \pi^2 \ t_{inf})/C_{inf}} \tag{4.1}$$

where α is the thermal diffusivity of the concrete and t_{inf} is the time where the influence point of thermal constant occurs. The calibration coefficient (C_{inf}) should be calculated for each inspected specimen.

Tran et al [55] had studied detectability of defects with different width-to-depths (w2d). A concrete block with artificial simulated delamination was tested by using pulsed phase thermography (PPT). The research concentrated on the w2d ratios less than 2.0. A quadratic relationship had been adopted between the observation time (t) and square depth (z^2) [95, 96]. In addition, the study showed that the increasing of heating up subjected on the specimen increases the estimation of defect depth. Another research had been performed by the same authors in 2018 [54]. They focused on the effects of depth, heating time, and rebar on detectability of defects on concrete specimens. Long pulsed thermography (LPT) had been used in the experimental work. The signal-to-noise ratio (SNR) was employed to evaluate the detectability of delamination. Moreover, an analytical equation was adopted a quadratic function between the observation time (T_{max}) and the depth of delamination based on a one-dimensional equation of heat flux [95, 96]. The mean absolute percentage error (MAPE) was employed to assess the results between the calculated and real depths [97]. In 2017, Hiasa et al [98] studied the effect of the size and shape of defects to improve the reliability

and applicability of infrared thermography in concrete structures. It was possible to estimate the delamination depths by using a finite element modeling. The process had been done by comparing the temperature difference (ΔT), between the sound and defect areas, that was obtained from infrared thermography which was gained from the finite element model (FEM) at several depths. The results showed that the method worked in a very good agreement.

Cheng [99] had used the machine learning (ML) to detect defects in a concrete specimen. An experimental test had been achieved in a laboratory but with three different conditions to evaluate the performance of models. In addition, a procedure had been developed to include the thermal conditions by using principal component analysis (PCA) and later on predict defects by two supervised machine learning models. A convolutional neural networks (CNN) had been adopted by Perez et al [100] to automatically detect and localize defects, mould, deterioration and stain in buildings. The method showed a very good accuracy throughout training images to detect the defects. On the other hands, the approach had some limitations, such as several types of defects are not considered in the network.

4-3 Research Methodology

A new process has been adopted for the present study by employing a combination of two approaches on the collected thermal images, the Fast Fourier Transform (FFT) and the Machine Learning (ML) technology. Figure (4-1) illustrates the steps that have been proposed to achieve the main goals of this research.

Date acquisition: Thermal images were acquired with a resolution of 324 × 256-pixel display, as a 2D-matrix for each individual image. This operation let the analysis engine deal individually with each extracted signal, performing to be more beneficial in the next process.

Pixel-wise data pre-processing and manipulating: All thermal IR images collected during the current study have been passed through a pre-process of manipulation, in order to identify and separate noisy information. First, the process starts with the transformation of the 2D IR images captured into a 1D dataset which represents the pixel's temperature changing during the period of a test acquisition. The next stage is by locating the maximal and minimal envelope as stated in Figure (4-1b) for each one-dimensional signal obtained to approximately estimate the average temperature changing in these

signals. The final stage is by subtracting the obtained average temperature signals from the original one-dimensional signals for each pixel located in the two-dimensional thermal snapshots, as shown in Figure (4-1d). The purpose of this routine is to smooth the dataset that leads to detrend, normalized and denoise the thermal images.

3D Matrix and reconstructing 2D high contrast image: All detrended signals are transferred into a 3D matrix leading to reconstruct a 2D high contrast image for any course of time.

Splitting defects in the concrete specimen: Each delamination inside the concrete specimen will be split into parts. This analysis engine provides the flexibility for the Machine Learning (ML) to train the data smoothly, which will be discussed in details later. However, delamination is divided into four parts and then the temperature variations are extracted from each part and transferred as a one-dimensional signal. Moreover, a specific period (a day, a week, or a month) of a dataset has been split up into regions to obtain the temperature variations. For example, the signals of a dataset for a one day have been divided into four regions between 12:00 am – 06:00 am, 06:00 am

– 12:00 pm, 12:00 pm – 06:00 pm and 06:00 pm – 12:00 am. The aim of this process is to efficiently increase the capability of reading the delamination temperature at variety depths and to decrease the disparities in each individual defect in the concrete components.

Processing of the Fast Fourier Transform: the FFT is individually applied on each signal and likewise on region (i.e., from 06:00 am to 12:00 pm) to build phases and amplitudes from a series of 3D matrix and as well as to acquire the frequency of these signals. The phase in the infrared thermography has a slighter influence by environmental circumstances such as, reflections, emissivity, surface geometry and nonuniform heating [101]. This advantage gives an agreeable for quantitative characterization in concrete objects being inspected [86].

Feature engineering: Features, from the previous routines, are extracted from the acquired phase and amplitudes. Two categories of features are sorted in this scenario: the major and the minor features (or the sub-features). The minor features are completely excerpted from the major features. There are four major features which are the pixel, the amplitude, the

phase, and the frequencies. These four main features are completely extracted from a specific period that is split into regions. Minor features are to be entirely contingent on main features by taking the averages and subtraction of these values. More details will be illustrated later in the Machine learning (ML) section.

Machine Learning and building predictive models: This process is appointed by training the extracted features for different periods by using the concept of Machine Learning (ML) via two classifiers, the Support Vector Machine (SVM) and k-Nearest Neighbor (KNN) to create training models.

Estimation depths in delamination: This phase is employing the predictive models on other datasets to estimate delamination depths in concrete specimens. The following sections will provide in details a clarification about the current methodology.

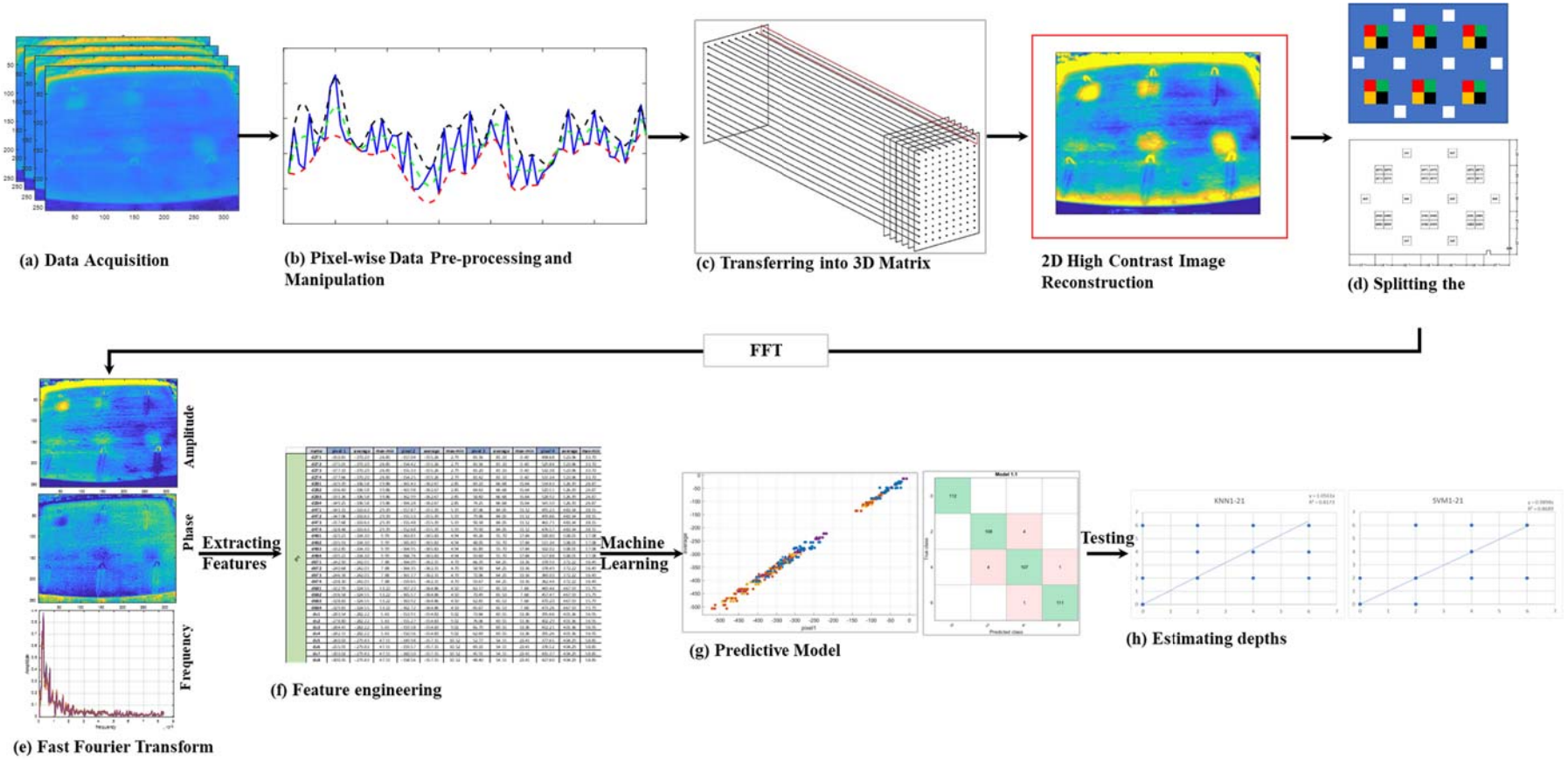

Figure 4-1: Schematic representation of the data processing methodology used in detecting defect depths.

4-4 Slab Fabrication

4-4-1 An Overview

A full-scaled reinforced concrete slab was fabricated and inspected in order to provide appropriate data for the Machine Learning analysis. The following sections will include in brief the outlines of selecting the design, experimental set up and materials being used. Moreover, figures, diagrams and directions of tests will be discussed in details.

Once the IR images are collected from the tests, a suitable procedure of analysis is employed to extract the necessary features. FFT analysis and machine Learning are both utilized to quantitatively estimate delamination depths.

4-4-2 Design and Construction

The reinforced concrete measures fourteen and a half feet by ten and a half feet width and eight inches thick (14.5 ft × 10.5 ft × 8 in.) as illustrated in Figure (4-2). Two mats of reinforcement steel (top and bottom) in both directions were used with concrete covers of 2.50 in. from the top and bottom layers of reinforcement mats to the nearest concrete surface as shown in

Figure (4-3). For the top steel reinforcement mat, steel bars #6 were placed each 6 in. along the long direction, while for the short direction, steel bars #5 spaced each 15 in. In addition, steel bars #5 were used for the mat in both direction with spacings of 9 in. and 10 in. for the long and short direction, respectively as schematic in detail in Figure (4-3). The reason that why the reinforcement design was selected is to fulfil the minimum requirement of Missouri Department of Transportation (MoDOT), and to imitate an actual concrete deck slab with existing delamination. In Engineering Policy Guide of MoDOT [102]. MoDOT guide involves several typical cross-sections depending on the functionality, loading and design. A minimum design cross-section (HL93,24'-0" Roadway-4 Girder) [102] was adopted with 8 in. thick in the current study.

Concrete type B-1 with 28-day design compressive strength of 4000 psi was used in the concrete slab to fulfill the minimum requirement of MoDOT for concrete deck slabs [102].

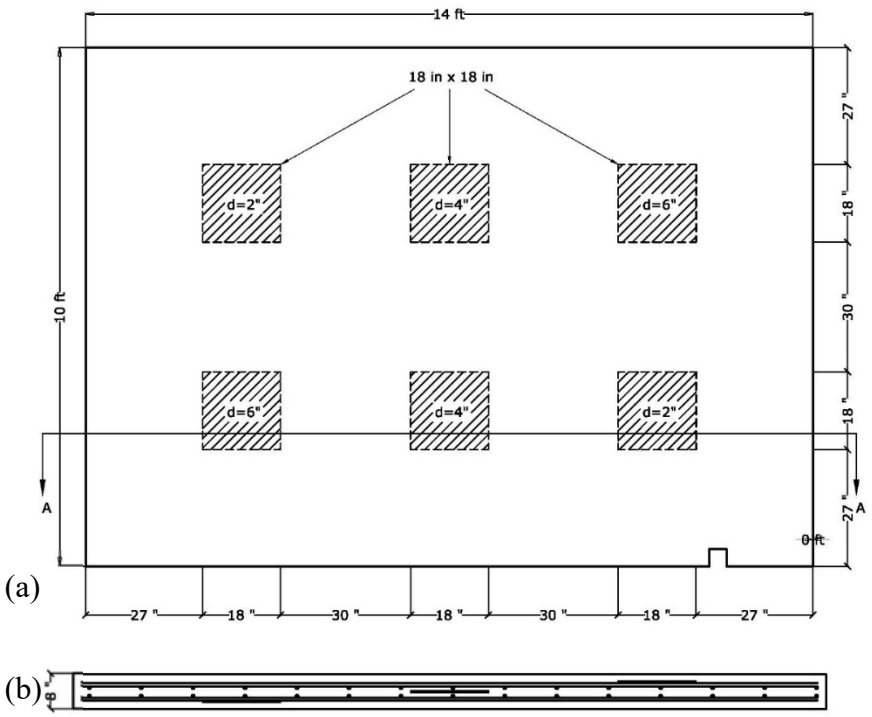

Figure 4-2: Plan view of concrete slab: a) showing the locations and dimensions of delamination embedded in the specimen, b) A cross section A-A showing the defect locations within the depth.

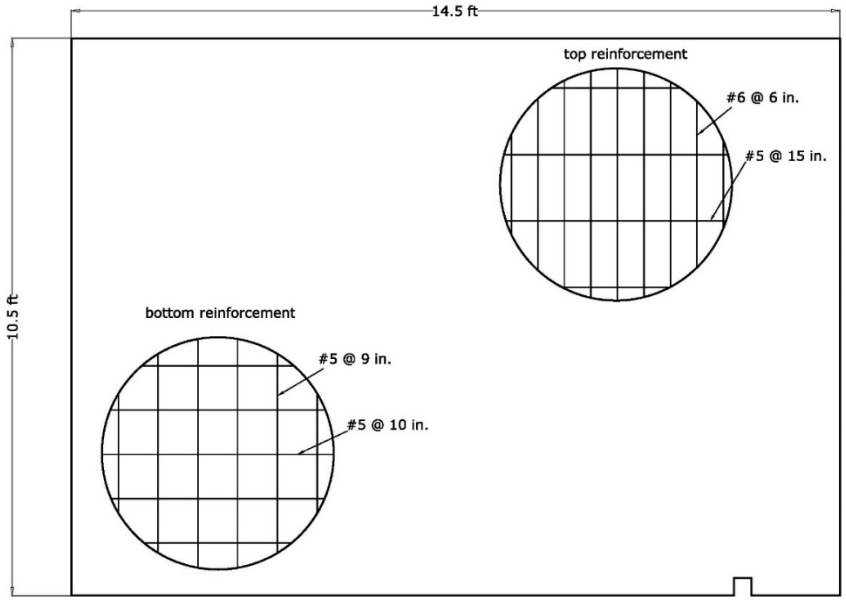

Figure 4-3: Details of the top and bottom layers of reinforcement steel in the concrete specimen.

To accurately simulate an actual condition of delamination inside deck slabs, the current research primarily depended on a previous research [18]. This research [18] had selected and tested three different materials symbolizing verified defects inside a small concrete specimen. The three materials (the defects) were open-celled Styrofoam, bubble wrap and open-celled plastic sheets. Each material being inspected by using the Impact Echo (IE) method showing a relative electrical resistance close to the relative acoustic electrical resistance of air [18], since the delamination is considered as air-filled.

The current study selected the open-celled Styrofoam material with 0.22 in. thick. All delamination targets measure eighteen inches by eighteen inches (18 in. × 18 in.). Three defect depths have been chosen: 2-inch, 4-inch, and 6-inch in the current research. Six targets had been embedded in the concrete slab, two for each defect depth. This delamination had been arranged into two rows (top and bottom), each row has three targets. The order of them is 2-in., 4-in., 6-in. and 6-in., 4-in., 2-in. for the top and bottom rows, respectively.

The 2-inch delamination deep is attached to the highest top layer of rebars, while the 6-inch delamination deep is linked to the bottom surface of

the lowest bottom layer of reinforcement. In addition, a small frame has been built, which is also attached to both the top and bottom steel mat to mount the 4-inch-deep delamination. Figure (4-4) shows more details of fixing these targets.

As described in chapter two, most of the delamination occur due to corrosion in steel reinforcement. Specified concrete cover depths are typically 1.5-2.5 inches, with constructions errors sometimes resulting in shallow defect on the order of 2-in. deep on the top layer of steel, or 6-in. deep on the bottom layer of the reinforcement mat. Moreover, in some cases, rigid overlay of 2-in. thickness is applied to bride decks to provide a wearing surface and/or to rehabilitate a bridge deck. The cover deck depth of 4-inches was included to represent such a case. Additional details of fabricating the slab are shown in Figures (4-5) and (4-6) before pouring the concrete, showing the steel reinforcement and the locations of delamination.

Figure 4-4: Details of mounting defects with 4-in deep in the concrete slab: A steel frame was used to mount delamination at the middle of the concrete slab.

Figure 4-5: Location of the specimen in an open area next to the RTF and working on bottom layer of steel reinforcement.

Figure 4-6: Details of both layers of steel reinforcement, top and bottom, the locations of defects, and locations of hooks in the specimen before pouring the concrete.

4-4-3 Test Summary

The place of the specimen is located at an open field on the west side of the University of Missouri's Remote Testing Facility (RTF) as illustrated in the google map photo in Figure (4-7).

Two locations of the Infrared Ultra Time Domain (IR-UTD) have been employed as shown in Figure (4-7). The first location was set up to the north of the specimen, Figure (4-8) while the second one was installed on the west of the concrete slab. Several tests on the specimen have been done collecting thermal images. On the first location, two weeks of testing with a 1-minute interval has been completed by capturing more than 20,000 images. Later on, the IR-UTD system has been moved to the second spot and another two weeks of inspecting was made with also more than 20,000 collected pictures. Moreover, another two tests on location 2 have been implemented of three-day and one-week tests.

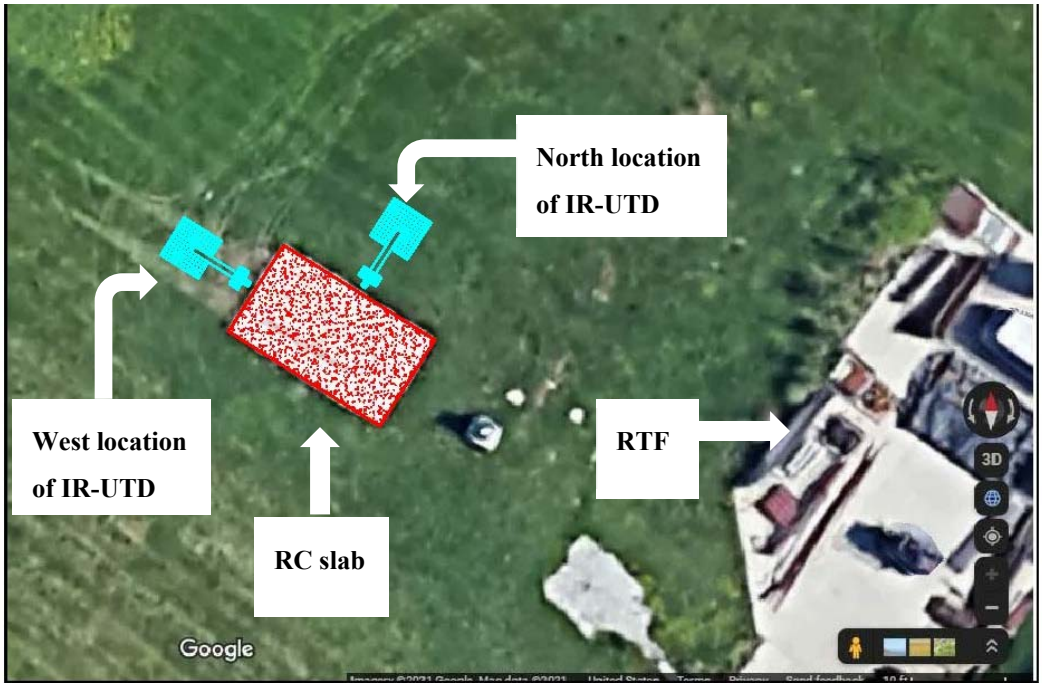

Figure (4-7): A map illustrating the location of the specimen with respect to the RFF and locations of IR-UTD system (the north and the west positions) with respect to the specimen itself.

Figure 4-8: The concrete specimen laying on the ground with the IR-UTD system located at the north side.

4-5 Multiscale Analysis of 1D Temperature Variations

Several decomposition algorithms are available for extracting multiscale 1D temperature signals, such as Fast Fourier Transform (FFT), Gaber Filters, Principal Component Analysis (PCA), Wavelet Transform (WT) and Empirical Mode Decomposition. The main reason of using the decomposition algorithms is to convert signals obtained from thermal images of the passive thermography to spectrum domain that exposes image features, such as phase, amplitude, and frequency, which are not visible in spatial domain. The frequency domain can also achieve more compact representations; for instance, the extension of the image itself. Another advantage can be seen in the spectrum domain which is designing digital filters that assist in improving the quality of images. For these reasons, the Fast Fourier Transform is adopted to extract features with the Machine Learning concept. The next sections are briefing of these approaches.

4-5-1 Fast Fourier Transform (FFT) Algorithm

Fast Fourier Transform (FFT) is considered one of the common methods that is used for signals analysis and image processing. It had been first developed and submitted by Joseph Fourier in 1807 for solving the

propagation of heat in solid bodies [103] by using Fourier series, which was a very powerful tool in solving ordinary partial equations. The main concept of the Fourier Transform is by generating a formula which comes from the summation of periodic functions such as sine and cosine terms. Moreover, this idea had been adopted to solve either the non-periodic functions by using the principle of Fourier integrals [104].

Fast Fourier Transform converts the time domain of a signal to the frequency component by using the one-dimensional Fourier Transform. Since that reason, the FFT surpasses other algorithms in their capability, such as Wavelet Transform (WT), in most stationary and non-stationary signals [105]. However, the components of the FFT can be either a real or complex number [106]:

$$Fn = \Delta t \sum_{k=0}^{n-} T\,(k\,\Delta t)\, e^{\left(-\frac{j2\pi nk}{N}\right)} = Re_n + lm_n \qquad (4.2)$$

where j = the imaginary number ($j^2 = -1$).

n = refers to the frequency increment (n=0, 1, … N).

Δt = the sampling interval.

Re = the real part of the Fourier Transform.

lm = the imaginary part of the Fourier Transform.

The real and imaginary terms of the complex transform are employed to calculate the amplitude A and the phase Ø [107] and construct 2D matrices as shown in Figure (4-1).

$$A_n = \sqrt{Re_n^2 + lm_n^2} \tag{4.3}$$

$$\emptyset_n = \tan^{-1}(\frac{lm_n}{Re_n}) \tag{4.4}$$

In the non-destructive thermography (NDT) implementations, it can be noticed that equation (4.2) is a very powerful tool, yet it is not practical because of the length of computation. The Fast Fourier Transform (FFT) is available in common softwares such as the MATLAB, which makes it more advantageous.

In general, temperature profiles (Temperature vs time length) are real functions which create real and odd imaginary when applying the FFT. In other words, they refer to symmetrical and non-symmetrical parts, which are even and odd functions. Therefore, there are N/2 of frequencies that are useful and the negative frequencies can be rejected.

4-6 Machine Learning (ML)

Machine learning (ML) has become one of the remarkable tools throughout developed organizations that are exploring renewal manners to leverage robust algorithms and increase the levels of understanding. ML authorizes systems to learn and test datasets, that are submitted by users, by utilizing specific algorithms. In other words, it is the output that is created when a user trains a machine-learning algorithm with a dataset. Machine-leaning is classified into supervised, unsupervised and deep learning [108]. The novel of supervised learning is dealing with labeled features. It typically discovers patterns in datasets, in contrast with, unsupervised learning which is employed when users deal with unlabeled datasets. Furthermore, problems have a massive amount of data. This method uses specific algorithms to classify the data depending on clusters that it discovers. The third type is deep learning which is a distinct method that merges neural network (NN) with layers to learn the datasets in other words, deep learning mimics the human brains [108]. It becomes useful when users deal with unstructured data.

Limited number of researches have been published throughout the last two decades by employing the machine learning methodology to detect subsurface defects. In 1998, Maldague et al [109] did a first attempt to

quantify depths. The research combined PPT with NN approach. An experimental work on aluminum and plastic materials had been done. Darabi et al in 2002 [110] had been providing quantitative information by using artificial neural networks. First step, a carbon fiber reinforced plastic (CFRP) had been modeled as a 3D thermal model. Later on, two neural networks (NN) were adopted to detect and estimate defects. Dudzik had utilized two-stage neural networks for detecting and estimating depth [111]. A classification neural network was improved to detect defects. The second stage used a regressive neural algorithm to estimate the depths. Halloua et al has used more detailed network for detection characterization defects [112]. Experimental work showed an effectiveness results in the prediction model.

There is no recent published research estimate the delamination depth in concrete structures under the natural environmental (passive thermography). The current research has adopted the machine learning (ML) to estimate the depth defects in concrete block. Classifiers, such as support vector machine (SVM) and k-nearest neighbor (KNN) have been adopted to train and test the extracted features from the inspected concrete block to predict a model. The following sections will discuss in brief the concept of these two algorithms.

4-6-1 Support Vector Machine (SVM)

The support vector machine (SVM) is an effective and simple algorithm which is widely adopted for classification, pattern recognition and regression. The SVM was first developed by Vladimir Vapnik and Alexey Chervonenkis [113] in 1963. In 1990's, SVM was improved and suggested by Vapnik [114] and later on used by Byun and Agarwal [115, 116] based on a statistical learning methodology. The concept of SVM method unlike the traditional approaches, such as neural network (NN), is to classify the dataset into two groups or more by using a linearly or nonlinearly hyperplane (a separable line or curve) and to increase the margin between separating data as illustrated in Figure (4-9).

The best hyperplane that has the biggest margin between two categories in one dataset, which represents distances between the hyperplane and the closet points in the classified categories in the dataset. In 1990's, Vapnik developed SVM as a Soft Margin Classifier or support vector machine in case there are some misclassifications of datasets as stated in Figure (4-9). Furthermore, the SVM had been improved by utilizing Kernel techniques by maximizing the features space boundaries to employ non-linearity between classes [117]. Kernel functions are algorithms that quantify resemblances

between observations. There are several types of Kernels that are adopted to classify non-linear datasets, such as polynomial, radial basis and linear Kernels.

For a 2D linear case, the following steps are below summarized to depict the procedure that is employed to solve a problem in the support vector machine (SVM).

- A linear classifier has a form of:

$$f(x) = W^T x_i + b \tag{4.5}$$

where W is the weight vector, x is the input vector, b is the bias and i=1, 2, …., N.

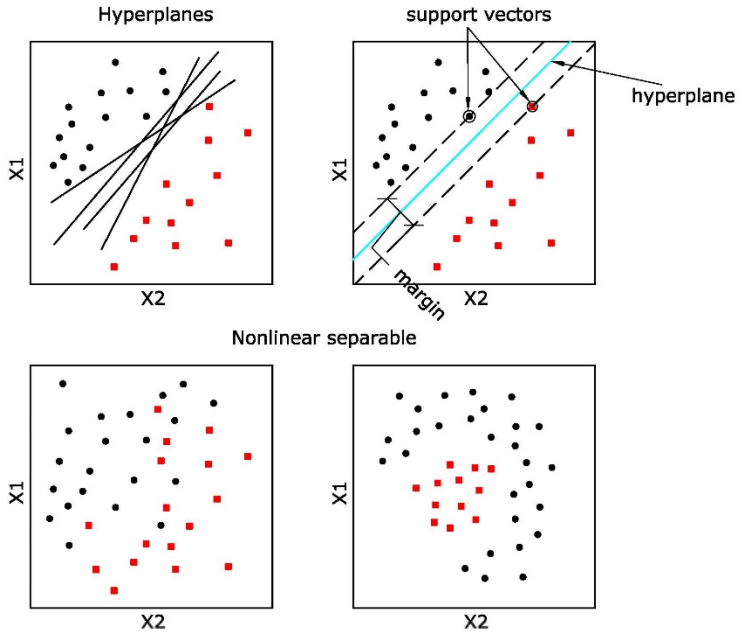

Figure 4.9: Define the hyperplanes in a dataset. H_1 and H_{-1} are the positive and negative support vectors, respectively.

$H_1: W^T x + b = +1$, $H_{-1}: W^T x + b = -1$, $H_0: W^T x + b = 0$ (4.6)

- d^+ and d^- are the smallest distances from the hyperplane to the nearest positive and negative points respectively. Thus, the margin is $d=d^+ + d^-$ for a given weight vector W and bias b.
- Maximizing the distance d leads to increase the margin in order to obtain an optimal hyperplane.
- The distance from a point (x_0, y_0) to a line:

$$ax + by + c = 0 \text{ is } \frac{ax_0 + by_0 + c}{\sqrt{a^2 + b^2}} \quad (4.7)$$

Consequently, the distance between H_1 and H_0 is:

$$d^+ = \frac{W^T x + b}{\|W\|} = \frac{1}{\|W\|} \text{ and then the margin } = \frac{2}{\|W\|} \quad (4.8)$$

1. From the previous equation, $\|W\|$ needs to be minimized to maximize the margin under the status that there are no points between H^1 and H^{-1} lines.

$$\max \frac{2}{\|W\|} \text{ is subjected to } W^T x + b \begin{matrix} \geq 1 \; if \; y_i = +1 \\ \leq -1 \; if \; y_i = -1 \end{matrix} \; for \; i = 1, 2, \dots, N \quad (4.9)$$

and equivalently $\min \|W\|^2$ is subjected to $y_i(W^T x_i + b) \geq 1 \; for \; i = 1, 2, \dots, N$ (4.10)

2. The obtained optimization problem is a quadratic function that can be solved by using the Lagrangian multiplier method.

4-6-2 k-Nearest Neighbor (KNN)

k-Nearest Neighbor (KNN) is considered one of the supreme machine learning classifiers. Its applications are multi-sided and could be used in finance, healthcare, political science, image processing and many other purposes. It has two main features: non-parametric and lazy learning algorithm. The formation of the model is decided from the dataset itself. It means no assumptions are required for data distribution. It is more beneficially since most datasets do not obey mathematical models. moreover, it does not need to train data to generate models, for lazy algorithm, since all data are trained during the testing phase. In other words, this makes the training phase faster and testing phase slower. In general, KNN needs more time to train and test the whole dataset which means more memory.

Basic steps illustrated in Figure (4-10) could be summarized into three points as followed:

1- Calculating distance between a new point (an example) and the other points of the other classes (such as Euclidean distance, Hamming distance, Manhattan distance and Minkowski distance).

2- Finding and deciding which are the closet neighbors.

3- Voting for labels depending on the neighbors that are close to a new point.

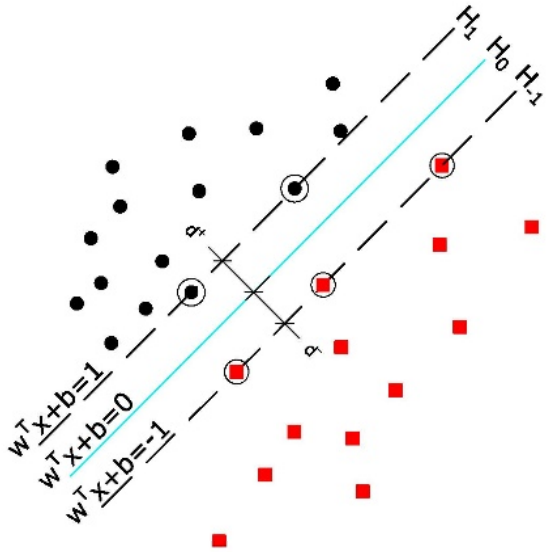

Figure 4-10: The steps are used to calculate the distances and decide what is the closet neighbors in the k-Nearest Neighbor (KNN).

In general, KNN works perfectly with a lower number of features. This means that the high great number of features requires more datasets. In addition, another disadvantage with KNN is the number of dimensions, which calls the curse of dimensionality. This issue (the growth of dimensions) might cause an overfitting.

Several solutions might be dealt with to avoid such a problem like this. Performing the principal component analysis before subjecting the machine learning technique or using another method which calls a feature selection approach.

There is no optimal value for k-nearest neighbor approach since each dataset has a unique features or own requirements. Researches have demonstrated that a small value of neighbor gives low bias but high variance while a high value of neighbor displays a lower variance but a higher bias.

The k-Nearest Neighbor is one of the simple algorithms that has been used in machine learning. the concept of KNN is by classifying new points based on another points of dataset that are more similar to them. KNN is an algorithm which is treated as both non-parametric and lazy learning. the feature of non-parametric means that there are no assumptions would be made. In other words, the full model is composed depending on the given datasets in lieu of assuming its structure. For lazy learning, there is no popularization. So, training datasets is little in the training process while all of the training datasets are employed second time in testing phase by using KNN method. Figure (4-11) below shows the concept or the idea of how the KNN works when attempting to assort a new point in dataset based on another given datasets.

It would be figured that the process will be started to its nearest points and assort depending on which is closet and more similar to. There are several ways and methods that calculate the distances between the new points and the

points of given datasets such as Euclidean, which is a mathematical method. KNN calculates the distances between each new point and tested datasets, the method then detects the probability of similarity between the new points and tested datasets and then assorts them according on the highest score of probability.

Despite that the KNN is simple to use and has no assumptions on the datasets, but still has some cons. Its accuracy mainly depends on the quality of the data. Moreover, an optimal k number (the value of nearest neighbor) must be determined to obtain the more accurate.

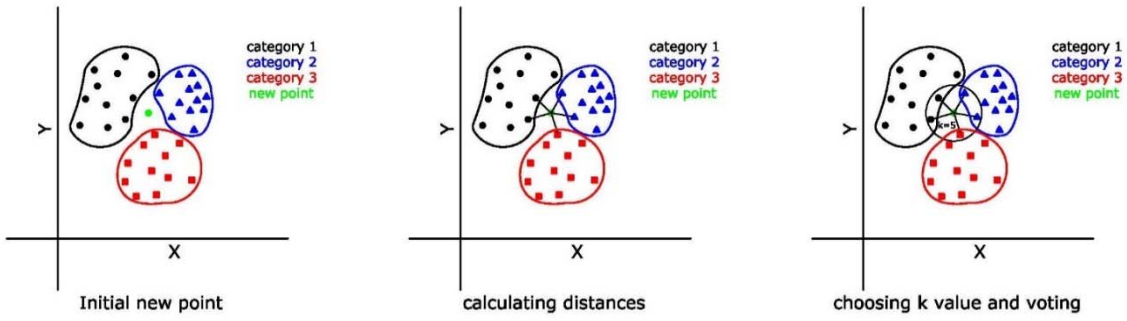

Figure 4-11: The concept of assorting new points depending on given datasets.

4-7 Feature Engineering

4-7-1 An Overview

A routine was utilized by using the FFT with the differentiation in the pixels of datasets to extract features. The strategy has been adopted to estimate depths by training their features to construct predictive models. The current method has proven to be more reliable since its accuracy was assessed with a forecasting model. The forthcoming sections will describe in details each process.

4-7-2 Feature Extraction

The features have been extracted by submitting the Fast Fourier Transform (FFT) algorithm on each pixel on the 3D matrix over a specific time to reconstruct amplitudes and phases. The specific period (for example a day, which is equal to 1440 snapshots) for the concrete block has been divided into four regions, every six hours as illustrated in Figure (4-12a). Before applying the FFT, the differentiation between thermal images captured have been taken, so, the one day has 1440 snapshots and it was split into four regions, each region consists of 360 images (a 6-hrs period). A contrast was taken between the image 12:00 am and the image at 06:00 am (region 1). This

separation had been repeated for region 2, region 3 and region 4. Moreover, for the same process, phases have been created for each region for each specific day, it means in each one day, four phases have been extracted by employing the FFT. In addition, this process is repeated for the frequency.

In general, the obtained features are classified into two sets according to the effective impact on the analysis that is done by the ML: Major and minor features. The major features refer to elements that have a substantial effect on the training analysis. These features, the major ones, increase the accuracy of training models with an influential value as will be clarified in the performance analysis section. The four major features that are utilized in this research are the phase, the amplitude, the frequency, and the pixel, columns 2, 5, 8 and 11 refer to the pixels, as stated in Table (4-1). The minor features are more reliant on the major features. That is to say, they are gained from the major features themselves by taking the average of these sets (the major features for their regions) or subtracting the minimum from the maximum values for each set. The purpose of adding these minor features is to strengthen the analysis, thus the classifiers will be able separately to distinguish each set in its zone. For instance, Table (4-1) illustrates that the values in column 2 and from row d2T1 to row d2T4 belong to a specific set or group of data.

Furthermore, minor features improved the results as will be discussed in the section analysis.

All the previous features are marked as input data in the classification. The output data are pointed as defect and sound areas. Column 14, named depth, in Table (4-1) has four values; 0 refers to the sound areas, spots are not delaminated, that are located in the concrete block as shown in Figure (4-13). The other three values are2, 4, and 6 that represent the depths of the embedded delamination inside the concrete block being tested.

Table 4-1: Illustration of major and minor features for one day.

		Major	Minor	Major	Minor	Major	Minor	Major	Minor	Depths
	column 1	column 2	column 3	column 4	column 5	column 6	column 7	column 8	column 9	column 10	column 11	column 12	column 13	column 14
	name	pixel 1	average	max-min	pixel 2	average	max-min	pixel 3	average	max-min	pixel 4	average	max-min	depth
Number of observations per one day	d2T1	-350.81	-370.20	26.85	-157.04	-155.26	2.79	81.16	81.33	0.40	498.68	523.06	33.70	2
	d2T2	-375.01	-370.20	26.85	-154.42	-155.26	2.79	81.56	81.33	0.40	529.84	523.06	33.70	2
	d2T3	-377.33	-370.20	26.85	-155.33	-155.26	2.79	81.20	81.33	0.40	532.38	523.06	33.70	2
	d2T4	-377.66	-370.20	26.85	-154.25	-155.26	2.79	81.42	81.33	0.40	531.34	523.06	33.70	2
	d2B1	-329.39	-336.58	19.86	-161.43	-162.67	2.85	69.23	66.68	15.64	514.63	526.39	26.87	2
	d2B2	-336.40	-336.58	19.86	-161.98	-162.67	2.85	64.63	66.68	15.64	520.51	526.39	26.87	2
	d2B3	-331.26	-336.58	19.86	-162.99	-162.67	2.85	58.60	66.68	15.64	528.92	526.39	26.87	2
	d2B4	-349.25	-336.58	19.86	-164.28	-162.67	2.85	74.25	66.68	15.64	541.50	526.39	26.87	2
	d4T1	-341.31	-333.63	29.39	-157.87	-155.39	5.19	87.06	84.05	11.12	495.23	483.34	38.15	4
	d4T2	-347.06	-333.63	29.39	-155.53	-155.39	5.19	79.06	84.05	11.12	499.86	483.34	38.15	4
	d4T3	-317.68	-333.63	29.39	-155.48	-155.39	5.19	90.18	84.05	11.12	461.71	483.34	38.15	4
	d4T4	-328.48	-333.63	29.39	-152.68	-155.39	5.19	79.90	84.05	11.12	476.57	483.34	38.15	4
	d4B1	-329.21	-334.30	9.99	-163.81	-165.83	4.94	49.26	55.70	17.84	500.80	508.01	17.08	4
	d4B2	-335.93	-334.30	9.99	-165.80	-165.83	4.94	48.05	55.70	17.84	511.34	508.01	17.08	4
	d4B3	-332.85	-334.30	9.99	-164.95	-165.83	4.94	65.89	55.70	17.84	502.02	508.01	17.08	4
	d4B4	-339.21	-334.30	9.99	-168.76	-165.83	4.94	59.60	55.70	17.84	517.88	508.01	17.08	4
	d6T1	-242.90	-242.01	7.88	-164.09	-162.31	4.70	66.39	64.25	13.16	378.93	372.22	16.49	6
	d6T2	-240.68	-242.01	7.88	-164.35	-162.31	4.70	58.90	64.25	13.16	378.49	372.22	16.49	6
	d6T3	-246.18	-242.01	7.88	-161.17	-162.31	4.70	72.06	64.25	13.16	369.03	372.22	16.49	6
	d6T4	-238.30	-242.01	7.88	-159.65	-162.31	4.70	59.67	64.25	13.16	362.44	372.22	16.49	6
	d6B1	-322.99	-324.55	13.22	-167.23	-164.86	4.50	63.17	65.53	7.68	469.44	467.59	15.79	6
	d6B2	-316.58	-324.55	13.22	-165.57	-164.86	4.50	70.49	65.53	7.68	457.47	467.59	15.79	6
	d6B3	-328.83	-324.55	13.22	-163.92	-164.86	4.50	62.81	65.53	7.68	470.20	467.59	15.79	6
	d6B4	-329.81	-324.55	13.22	-162.72	-164.86	4.50	65.67	65.53	7.68	473.26	467.59	15.79	6
	ds1	-283.54	-282.22	5.61	-153.91	-154.83	9.02	73.66	69.55	13.36	395.66	401.36	16.95	0
	ds2	-278.80	-282.22	5.61	-155.27	-154.83	9.02	76.06	69.55	13.36	402.29	401.36	16.95	0
	ds3	-284.41	-282.22	5.61	-159.58	-154.83	9.02	65.79	69.55	13.36	412.21	401.36	16.95	0
	ds4	-282.11	-282.22	5.61	-150.56	-154.83	9.02	62.69	69.55	13.36	395.26	401.36	16.95	0
	ds5	-260.03	-279.83	47.11	-149.98	-157.15	10.52	52.77	54.11	23.41	377.65	404.29	58.85	0
	ds6	-255.91	-279.83	47.11	-159.57	-157.15	10.52	69.33	54.11	23.41	376.52	404.29	58.85	0
	ds7	-303.02	-279.83	47.11	-160.50	-157.15	10.52	45.91	54.11	23.41	435.37	404.29	58.85	0
	ds8	-300.35	-279.83	47.11	-158.56	-157.15	10.52	48.40	54.11	23.41	427.60	404.29	58.85	0

Table (4-1) is an example of the features that have been used in the learning analysis. The rows stand for features at different regions while the columns are the input and output data of the defect and non-defect spots. It can be noticed that, in Table (4-1), each defect and/or non-defect area has four values instead of one since the days have been split into four regions (each 6 hours) as mentioned before. Moreover, as stated in Figure (4-13), each defect has been divided into four equal parts. The reason of this scenario is to improve the capability of detection of the delamination depths by reducing the impact of edge effect in the defects and noise elements. This might occur by a heat transfer around the edges which have an exposure to the ambient environmental. Furthermore, this process increases the number of features, as depicted in Figure (4-13) and written in Table (4-1) by boosting the training models. Each defect will have four additional features by enhancing the sensitivity of the models. The thermal image of the inspected concrete specimen displays that there are some distortions and differentiations at the edges for each delamination which potentially affects the constructing of the training model. Through this premise, the concept has been adopted by increasing the number of observations by utilizing four defects instead of one in each delamination depth.

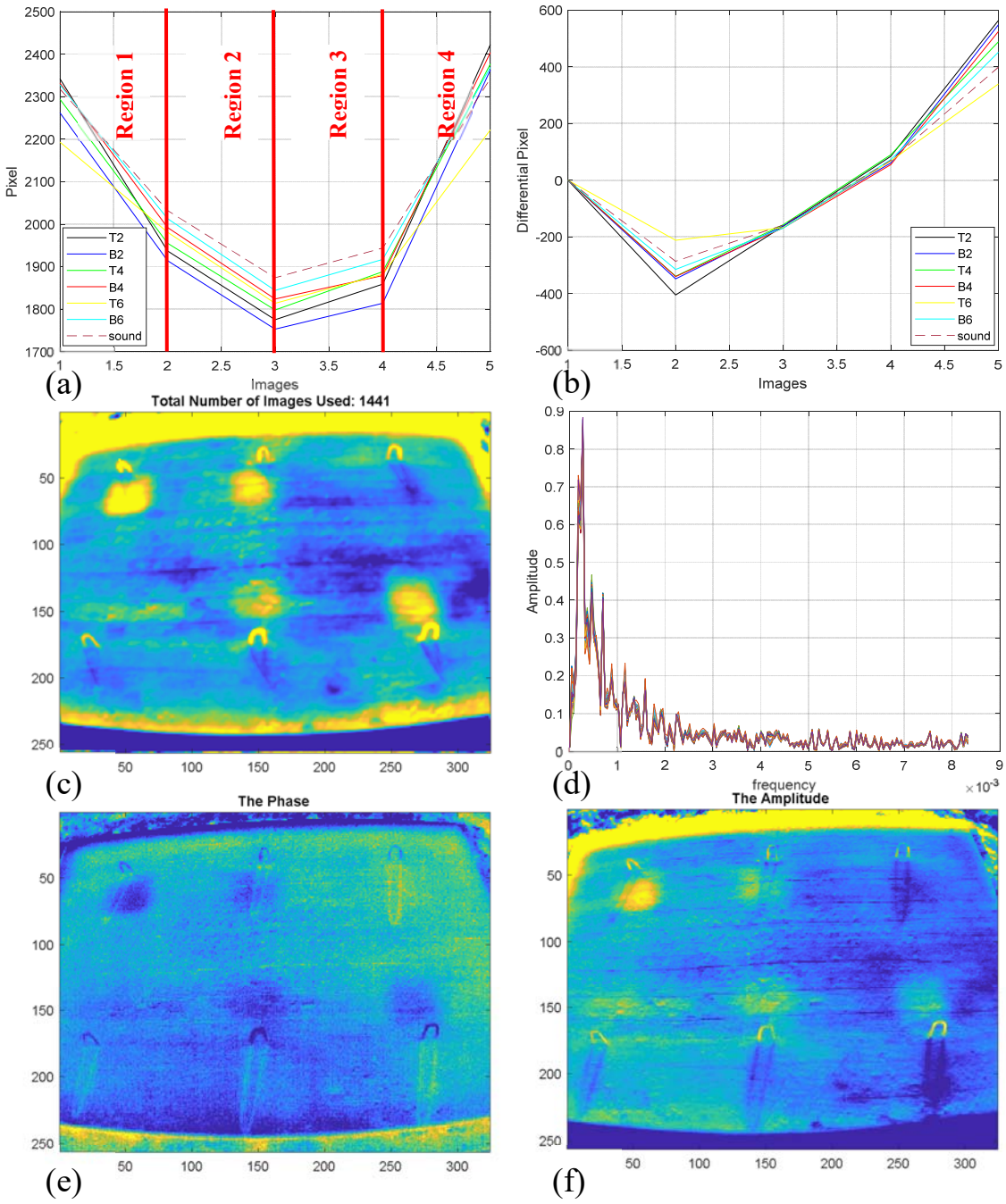

Figure 4-12: The concept used to extract major features: a) dividing a specific period into four regions, b) differentiation of each pixel for the specific period to obtain pixels, c) the normalized thermal image for the specific period, d) choosing frequencies for each defect and sound areas, e) the phase of the specific period and f) the amplitude of the specific period.

This technique was needed to have a robust algorithm for detecting and analyzing sub-surface delamination. This approach will award a more prominent scope to train the datasets and thus augment the reliability of predicted model by the Machine Learning.

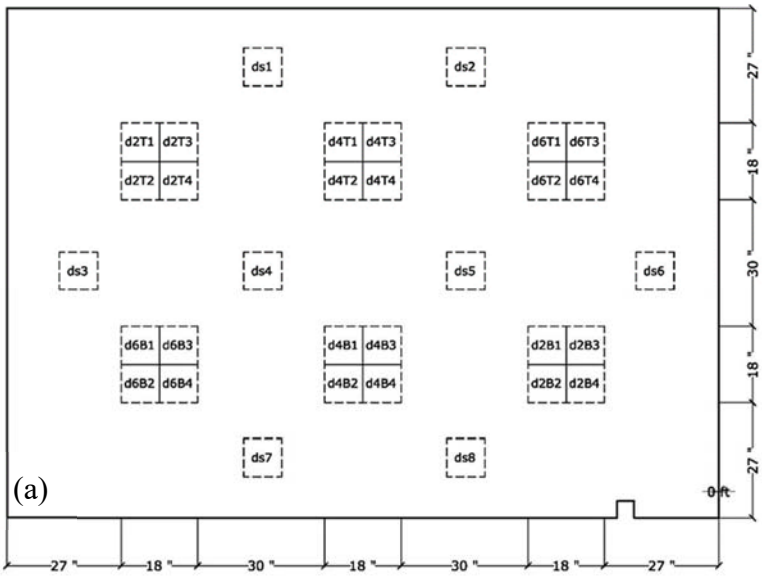

(a)

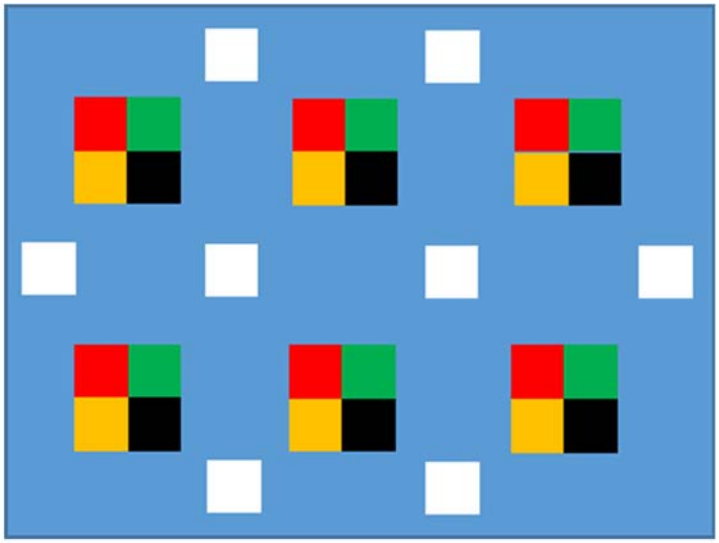

(b)

Figure 4-13: a) The labels of the four parts of defects and sound areas, b) the process of dividing each defect and the locations of sound areas in the specimen. The white spots are the sound areas, and the remaining colors are the defect areas.

Therefore, eight features have been chosen for each delamination depth since there are three different depths (2, 4 and 6 inches) and each particular depth has two delamination in the same concrete specimen being inspected. For this reason, eight sound (non-defect) areas have been randomly selected as shown in Figure (4-13) to avoid the unbalanced training in the Machine Learning process.

4-8 Performance Analysis and Discussion of Results

4-8-1 Validation Scheme

It is important to choose a better validation technique to examine the predictive accuracy of the ML models. The validation estimates the model performance on the input data (extracted features) compared to the training data and assists to select better models. One of the advantages of choosing better validation is to protect learning against overfitting. All classifiers could be compared in session using the same validation scheme by choosing a validation scheme before training any model. The forthcoming sections will describe the validation schemes that are used in the current classification.

1. **Cross-Validation:** It selects a number of folds (or divisions) to partition the dataset used by the learners. By assuming n folds, the following steps are summarized:
    a. Partitioning the data into n discrete sets.
    b. For each fold:
        - The application trains a model using the out-of-fold observations.
        - The application evaluates model performance using in-fold data.
    c. Calculating the average error over all the n folds.

This process gives a very good estimation of the predictive accuracy of the final model since all the data are trained. It requires multiple fits but the merit of using it by making an efficient employment of all the data, so it is recommended for a small dataset.

2. **Holdout Validation:** It chooses a percentage of the data to be used as a test division. The model is trained on the training division and valued its performance with the test fold. Thus, the model subjected for validation is only based on a portion of the data. The final model is trained with the

full data set. For this reason, holdout validation is only recommended for a large dataset.

4-8-2 The Confusion Matrix

The aim of plotting the confusion matrix is to understand how the currently selected classifier performs in each class. Moreover, it identifies the areas where the classifier has performed properly or poorly. Figure (4-14) shows an example of a confusion matrix where the rows show the true class, and the columns show the predicted class. The diagonal cells depict where the true class and predicted class are matching. If these cells are green, the classifier has performed well and classified observations of this true class correctly. The default view states a number of observations in each cell.

Finding the areas where the classifier performed poorly is done by examining the cells off the diagonal that display high percentages and are red. The higher the percentage, the brighter the hue of the cell color. In these red cells, the true class and the predicted class do not match. The data points are misclassified.

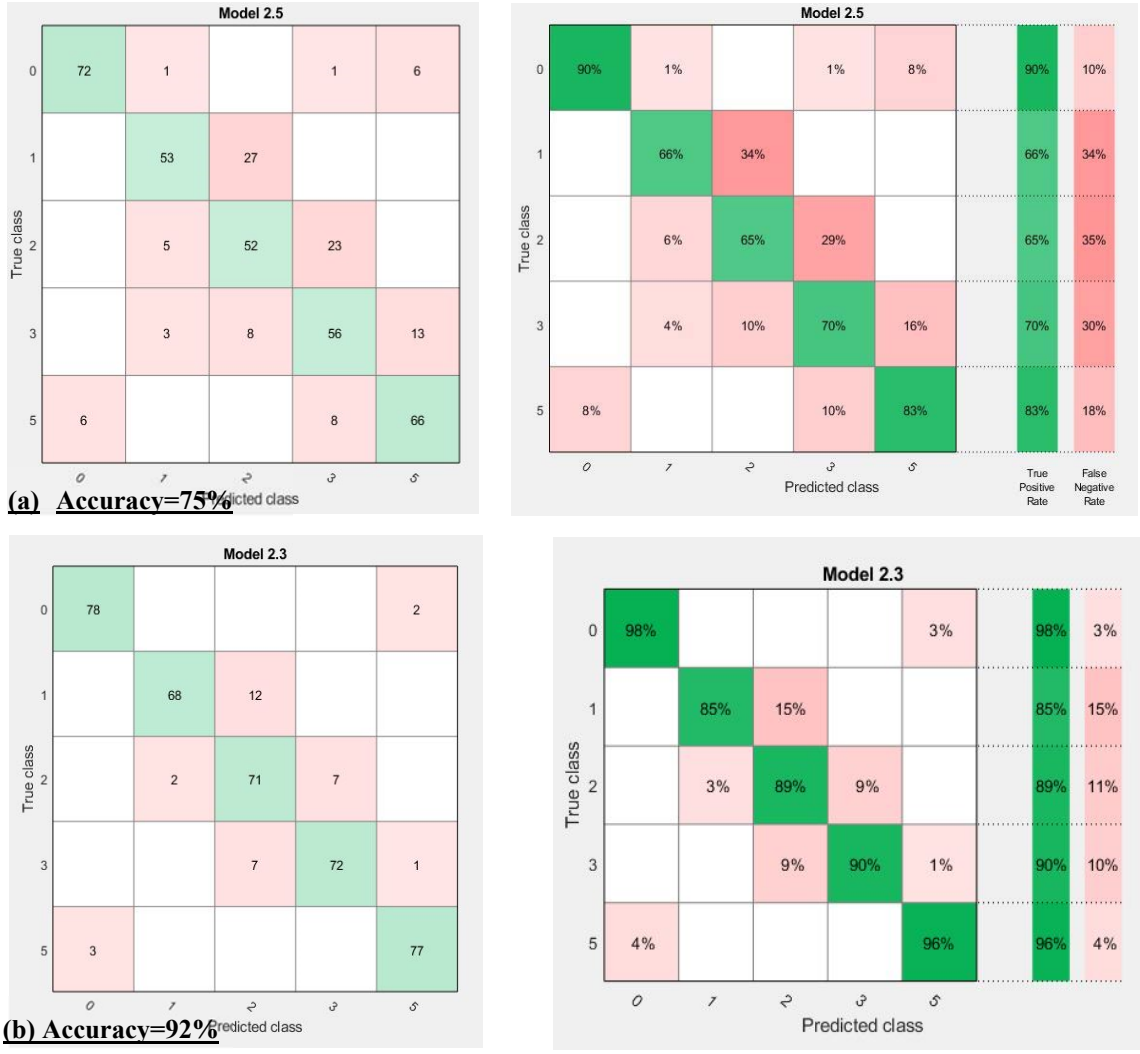

(a) Accuracy=75%

(b) Accuracy=92%

Figure 4-14: An example of a confusion matrix showing the accuracy of two models: a) a model with 75% accuracy illustrating where the classifier poorly performs, b) a model with accuracy of 92%.

4-8-3 The ROC Curve

The receiver operating characteristic (ROC), shown in Figure (4-15), curve illustrates true positive rate versus false positive rate for the currently selected trained classifier.

The marker on the plot states the performance of the presently classifier. Moreover, the marker shows the values of the false positive rate (FPR) and the true positive rate (TPR) for the currently selected classifier. For instance, a false positive rate (FPR) of 0.2 indicates that the current classifier assigns 20% of the observations incorrectly to the positive class. A true positive rate of 0.9 indicates that the current classifier assigns 90% of the observations correctly to the positive class.

A perfect result with no misclassified points is a right angle to the top left of the plot. A poor result that is no better than random is a line at 45 degrees. The Area Under Curve number is a measure of the overall quality of the classifier. Larger Area Under Curve values indicate better classifier performance.

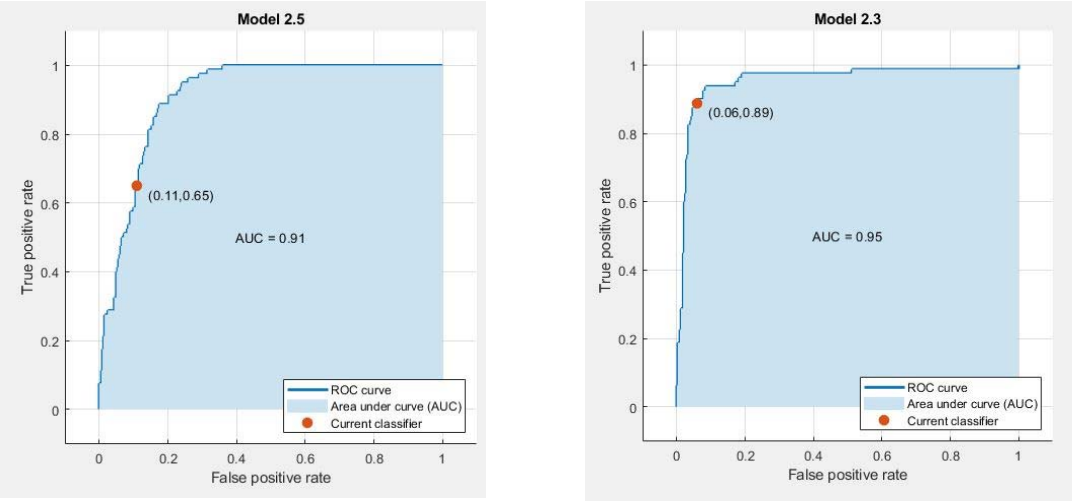

Figure 4-15: An example of the ROC for defect areas.

4-8-4 Analysis and Results

4-8-4-1 An Overview

In the forthcoming sections, multiple classifier learners have been employed, the Support Vector Machine (SVM) and the k-Nearest Neighbor (KNN). In the presented approach, several steps have been followed to estimate the depths in delamination. The first step is training a group of datasets that have been extracted from the test (the first two weeks and the second two weeks), previously stated in section (4-5), in order to build predictive models that will be used to estimate the depths in delamination in the concrete slab. A MATLAB Software package has been employed to conduct the training models and estimate depths in the concrete specimen.

4-8-4-2 Building Predictive Models

As mentioned in the section (4-7), the features that are extracted from the concrete slab have been completed. To build a better predictive model, several training analyses have been performed to reach the optimum performance depending on the accuracy of the results. Four major features have been taken into consideration in the analysis which are Pixels, Phases, Amplitudes and Frequencies. Moreover, additional minor features have been

added sequentially to the major features over the training. The purpose of that was to achieve and build efficient models for estimating the depths in defects. Table (4-2) illustrates the cases that have been accomplished. The Table confirms the increasing in accuracy percentage of the built models by adding the minor features to the major features.

Table 4-2: The process of algorithm analysis for the features.

	First Two Weeks				
				Accuracy %	
	Cases	features	observations	KNN	SVM
1	pixel (only majors)	4	448	86.20%	65.40%
2	pixel + minors	12	448	100.00%	100.00%
3	pixel + phase (only majors)	8	448	88.20%	84.80%
4	pixel + phase + minors	24	448	98.20%	98.20%
5	pixel + phase + amp (only majors)	12	448	89.30%	87.90%
6	pixel + phase + amp + minors	36	448	99.10%	99.10%
7	pixel + phase + amp + freq (only majors)	16	448	83.00%	83.90%
8	pixel + phase + amp + freq + minors	48	448	98.70%	98.90%
9	phase + amp + freq + minors	12	448	78.30%	79.10%
10	phase + amp + freq + minors	36	448	95.00%	96.30%
11	pixel+phase + amp + freq (only major) (one part)	16	112	29.50%	38.40%
12	pixel+phase + amp + freq + minors (one part)	48	112	80.40%	89.30%

4-8-4-3 Training Models and Predicting Depths

Several analyses have been accomplished on the concrete specimen being tested in the RTF (Remote Testing facility at University of Missouri) to acquire the delamination depths. As previously mentioned in section (4-4-3), two main tests had been done on the concrete slab at the north and west sides. Each test had lasted for two weeks (more than 20,000 snapshots within 1-minute interval time). For that reason, the analysis has been grouped into ten

parts: two-week training on two-week testing, one-week training on one-week testing, three-day training on three-day testing, one-day training on one-day testing, three-week training on one-week testing, two-week training on one-week testing, three-week training on three-day testing and one-day testing respectively, two-week training on three-day testing and one-day testing sequentially, one-week training on one-day testing, and finally three-day training on one-day testing. The following sections outline in details the description of each analysis, fitting diagrams, and tables. In each analysis, two fitting diagrams are selected including both classifiers, the KNN and the SVM. All the fitting diagrams are presented in Appendix A.

4-8-4-3-1 Two-week Training on Two-week Testing

In this analysis, the first two weeks have been trained by using the classifiers SVM and KNN which gave an accuracy of accuracy of 99.6% and 100% respectively throughout building the models. In this case, the first two weeks (day 1 to day 14) have been trained and tested on the next two weeks (day 15 to day 28). The next step is by training the second two weeks then testing them on the first two weeks.

In this case, four major features and their minors have been included in the analysis. The total number of the major and minor features are 48 with one output, the defect depths. The total observations in this case are 448 since there are 14 days each.

The results showed, Figure (4-16), that the second case obtained better results since the R^2 values are 0.71 and 0.74 for the KNN and SVM respectively. Table (4-3) summarizes the obtained depths.

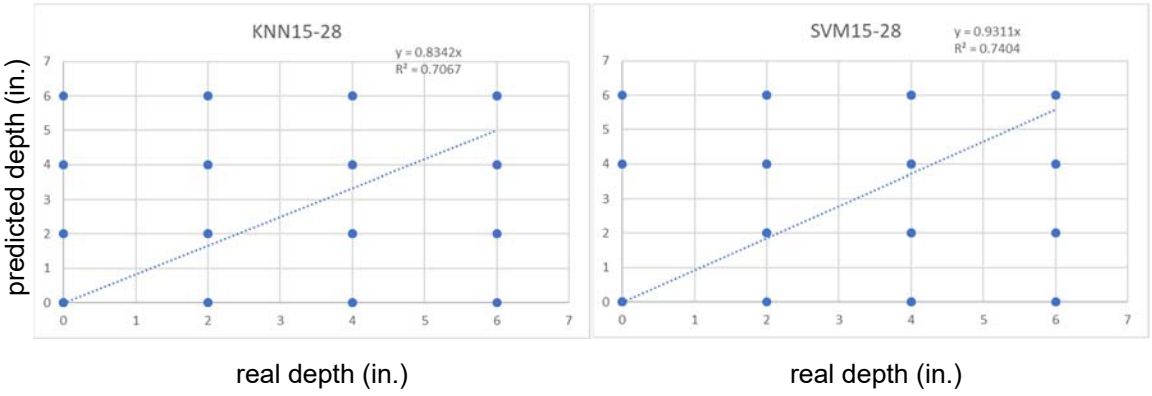

Figure 4-16: Fitting diagrams for two-week training on two-week testing.

Table 4-3: The calculated depths of the delamination, case two-week on two-week.

	Case 1		Case 2	
	KNN (in)	SVM (in)	KNN (in)	SVM (in)
Sound	0	0	0	0
Defect 2-in.	1.53	1.57	1.67	1.86
Defect 4-in.	3.07	3.13	3.37	3.72
Defect 6-in.	4.60	4.70	5.01	5.59

4-8-4-3-2 One-week Training on One-week Testing

Six cases have been chosen and taken into consideration in the current analysis. The weeks were divided into four parts which are (day 1 to day 7), (day 8 to day 14), (day 15 to day 21), and (day 22 to day 28). Each week has been trained to create models by using both the KNN and SVM classifiers. The first part (day 1 to day 7) has been tested on days (8 to 14) and days (15 to 22). Each part of the test has been trained and their models are created by using both the KNN and SVM classifiers. Moreover, the days (8 to 14) and days (15 to 22) are tested by days (1 to 7) to estimate depths. On the other hand, days (1 to 7) has been inspected by days (8 to 14) and days (15 to 22) respectively. Furthermore, the last case was by training days (15 to 21) then examined them on days (22 to 28). In contrary, the days (15 to 21) are tested by days (22 to 28). Overall, each week forementioned has been trained and inspected by the other week. Figure (4-17) explains the process that has been achieved.

Since there are seven days for each part, the total observations are 224. The total features are the same as the previous case, which are 48 features plus one out, the depths.

Good results have been obtained in the current process. R^2 values are 0.76 and 0.80 when training days (8 to 14) on days (1 to 7) for both the KNN and SVM respectively. Moreover, the case of training days (15 to 21) 0n days (22 to 28) has values of R^2 equal to 0.87 and 0.69 for the SVM and KNN sequentially. Table (4-4) summarized most of the cases that have given better results in this procedure.

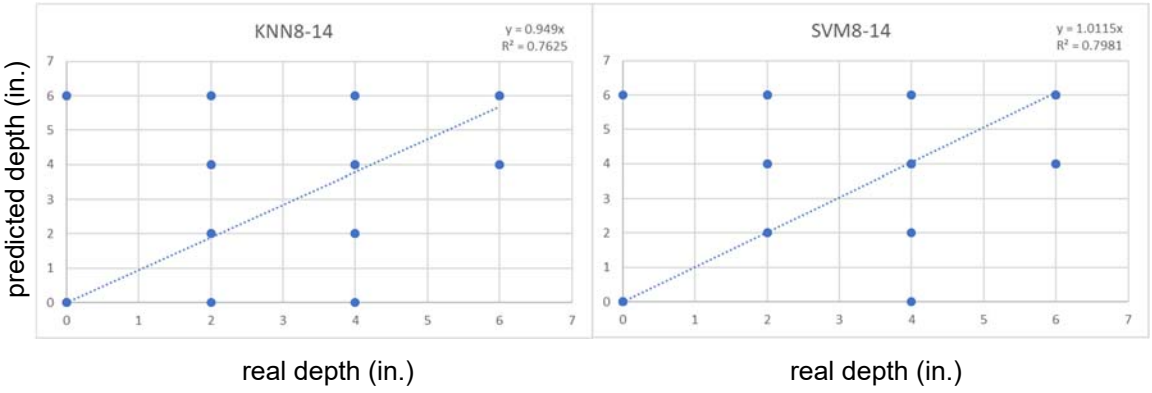

Figure 4-17: Fitting diagrams for one-week training on one-week testing.

Table 4-4: The calculated depths of the delamination, case one-week on one-week.

	Case 1		Case 2		Case 3		Case 4	
	KNN (in)	SVM (in)	KNN (in)	SVM (in)	KNN (in)	SVM (in)	KNN (in)	SVM (in)
Sound	0	0	0	0	0	0	0	0
Defect 2-in.	1.90	2.02	1.82	1.91	1.98	2.14	1.79	1.55
Defect 4-in.	3.80	4.05	3.63	3.82	3.95	4.29	3.58	3.10
Defect 6-in.	5.69	6.07	6.07	5.73	5.93	6.43	5.37	4.65

4-8-4-3-3 Three-day Training on Three-day Testing

In this process, five groups of three days have been selected on eight cases of training and testing to estimate the depths in delamination. These the three-day groups are days (1 to 3), days (4 to 6), days (15 to 17) and days (22 to 24). Most of these built models, the SVMs and KNNs, have granted good agreements and fitting outcomes with the exact solution. The models that have yielded appropriate results are days (1 to3), days (22 to 24) and days (15 to 17) with adequate values of R^2 as illustrated in Figure (4-18). Moreover, the remaining models have acceptance agreement regardless of the low rate of R^2 within sixties since the accuracy of the depths was more than eighties.

The current procedure deals with 96 observations since there are three days of the analysis by 32 observations per day. In addition, the same number of features have been employed which is 48 combined form the major and minor features in total.

The results of fitting paragraphs are listed in Figure (4-18). Group of days (1 to 3) on days (4 to 6) gave a precision of 95% with 0.61 R^2 value. The groups of days (22 to 24) on days (15 to 17), days (1 to 3) on days (15 to 17) and days (15 to 17) on days (1 to 3) have reached values of R^2 equal to 0.67, 0.71 and 0.75 respectively in both the SVMs and KNNs models with

accuracies in eighties and nineties. The remaining models have given a good accuracy but with R^2 values in sixties. The results have been summed up in Table (4-5).

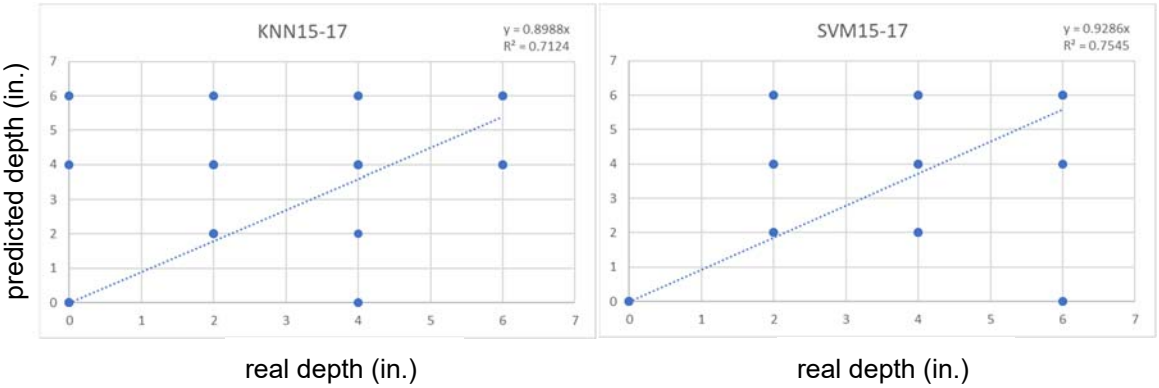

Figure 4-18: Fitting diagrams for three-day training on three-day testing.

Table 4-5: The calculated depths of the delamination, case three-day on three-day.

	Case 1		Case 2		Case 3		Case 4	
	KNN (in)	SVM (in)	KNN (in)	SVM (in)	KNN (in)	SVM (in)	KNN (in)	SVM (in)
Sound	0	0	0	0	0	0	0	0
Defect 2-in.	1.64	1.90	1.61	1.68	2.21	2.11	1.80	1.86
Defect 4-in.	3.29	3.81	3.21	3.36	4.42	4.23	3.60	3.71
Defect 6-in.	4.93	5.71	4.82	5.04	6.63	6.34	5.39	5.57

4-8-4-3-4 One-day Training on One-day Testing

Many cases have been performed for the one-day training and one-day testing. Most of the cases have not provided good estimation for the delamination depths. Figure (4-19) states some cases that have been accomplished. It is clear that the fitting diagrams did not yield acceptable R^2 values, yet some cases awarded corresponding and suitable accuracy for estimating the depths. Subsequently, the values are low might be attributed to the number of the observations that have been employed in the current training (only 32 observations) to predict the depths in the concrete specimen. This hypothesis will be boosted through the discussion on the next sections that describe the training of data with larger observations than testing data. Table (4-6) summarizes some cases that are accomplished and produced below the rate of R^2 values.

In the current cases, only 32 observations have been employed with 48 features and one output value which is the depth.

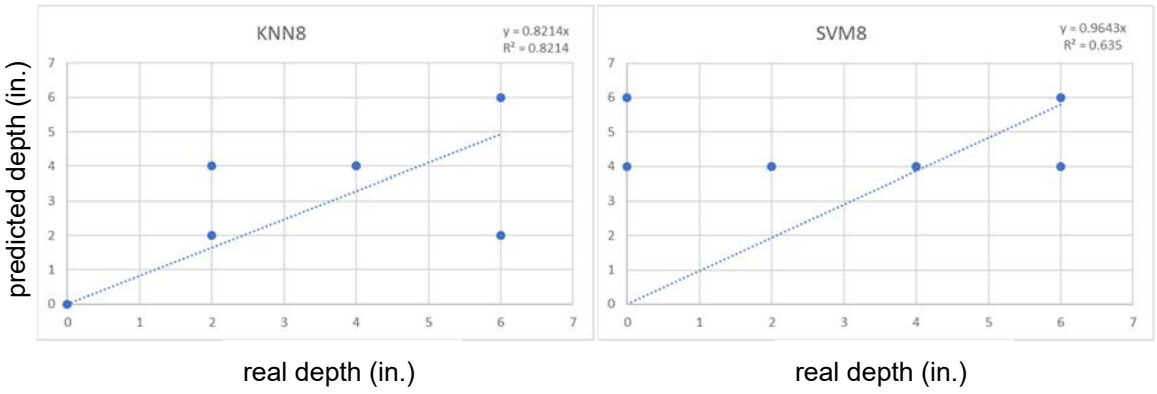

Figure 4-19: Fitting diagrams for one-day training on one-day testing.

Table 4-6: The calculated depths of the delamination, case one-day on one-day.

	Case 1		Case 2		Case 3	
	KNN (in)	SVM (in)	KNN (in)	SVM (in)	KNN (in)	SVM (in)
Sound	0	0	0	0	0	0
Defect 2-in.	1.77	1.29	1.64	1.93	1.56	1.43
Defect 4-in.	3.54	2.57	3.29	3.86	3.11	2.86
Defect 6-in.	5.30	3.86	3.86	5.79	4.66	4.29

4-8-4-3-5 Three-week Training on One-week Testing

In the current scenario, three weeks have been trained on one week to predict the depths in delamination. Since there are four weeks of thermal images testing, three weeks have been trained on a one-week testing. Two analyses have been accomplished, a training from day 1 to day 21 has been performed on testing from day 22 to day 28. The obtained results of the fitting diagrams for both the R^2 and the accuracy have outstanding values throughout

predicting the depths. However, the model of training days (1 to 21) earned values of R^2 equal to 0.82 and 0.87 with accuracy of +5% and -1% for the KNN and SVM respectively. Furthermore, the KNN classifier obtained an R^2 value equals to 0.76 while the SVM classifier got 0.73 value of R^2 when the model of training days (8 to 28) is adopted. The accuracy values for both classifiers in the last model are -5% and -11%.

In the current training, the observations are 672 since there are 32 ones per day and the features are 48 with one output. When the number of the observations in the training data is greater than the testing data this leads to higher R^2 and accuracy values which will be apparently in the section of three-week training with three-day testing.

Figure (4-20) illustrates the two models that have been employed in the current case. In addition, Table (4-7) outlines the theoretical and real depths values and their percentage errors.

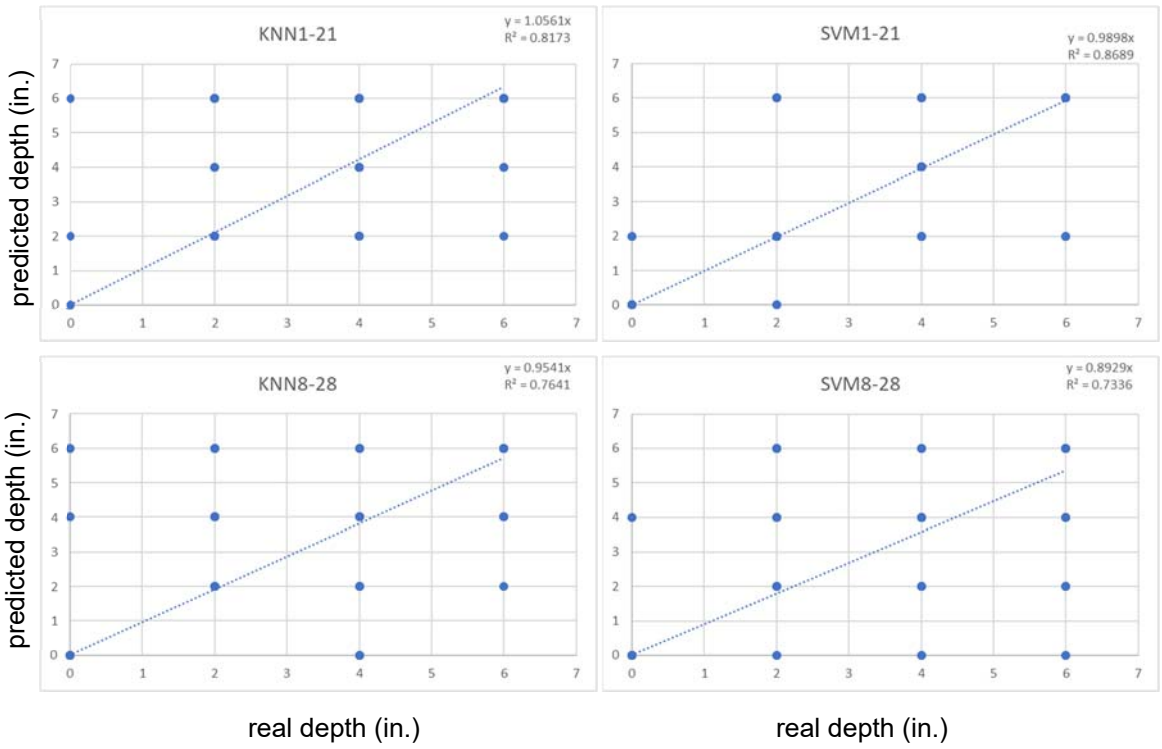

Figure 4-20: Fitting diagrams for three-week training on one-week testing.

Table 4-7: The calculated depths of the delamination, case three-week on one-week.

	Case 1		Case 2	
	KNN (in)	SVM (in)	KNN (in)	SVM (in)
Sound	0	0	0	0
Defect 2-in.	2.11	1.98	1.91	1.79
Defect 4-in.	4.22	3.96	3.82	3.57
Defect 6-in.	6.34	5.94	5.73	5.36

4-9-4-3-6 Two-week Training on One-week Testing

Four examples have been accomplished to predict depths in defects in the current state, the training of two-week and testing one-week. To do the variety of analyses, two samples of weeks are selected to be trained, two weeks are in the same sequence while the other two weeks are not. The first two-week in the same succession are days (1 to 14) and days (15 to 28) whereas the second two week that are not in sequence are days (1 to 7 and 15 to 21) and days (8 to 14 and s to 28). The one-week groups chosen to be tested are days (1 to 7) and days (8 to 14). Overall, the accuracies of the present cases range from 74% to 95%, which gives a convenient predictability of estimating depth in delamination. On the other hand, the R^2 values extended from 0.55 to 0.73, which is under or at the average acceptance. Figure (4-21) depicts all the fitting diagrams that have been completed in the two-week on the one-week case. There are three models that have been given good agreement, training days (15 to 28) on testing days (1 to 7), training days (1 to 7 and 5 to 21) on testing days (8 to 14), and training days (8 to 14 and 22 to 28) on testing days (1 to 7) for both learners the SVM and KNN.

Table (4-8) summarizes all the predicted depths and their errors, which gave acceptable results despite the low R^2 values in some cases.

The process has adopted 448 observations with 48 features including the major and minor features for the two-week case.

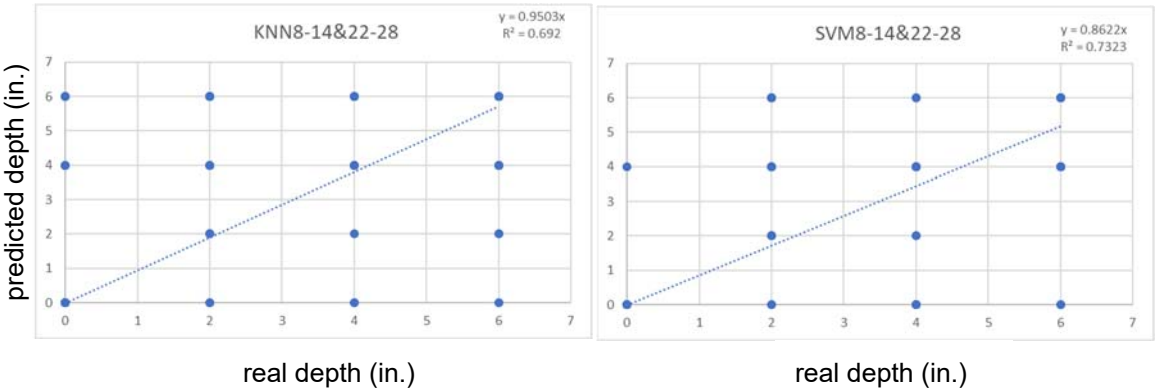

Figure 4-21: Fitting diagrams for two-week training on one-week testing.

Table 4-8: The calculated depths of the delamination, case two-week on one-week.

	Case 1		Case 2		Case 3		Case 4	
	KNN (in)	SVM (in)	KNN (in)	SVM (in)	KNN (in)	SVM (in)	KNN (in)	SVM (in)
Sound	0	0	0	0	0	0	0	0
Defect 2-in.	1.49	1.65	1.55	1.72	1.80	1.87	1.90	1.72
Defect 4-in.	2.97	3.31	3.11	3.45	3.61	3.74	3.80	3.45
Defect 6-in.	4.96	4.66	4.66	5.17	5.41	5.62	5.70	5.17

4-8-4-3-7 Three-week Training on Three-day and One-day Testing

Another two scenarios have been achieved, a three-week training on three-day testing and on one-day testing. The agreement of estimating the depths in the defects are in magnificent results. Two cases for each scenario have been analyzed. In the first scenario, two cases have been done, training days (1 to 21) on testing days (22 to 24) and training days (8 to 28) on testing days (1 to 3). Figure (4-22) states the fitting diagrams for both cases with reasonable R^2 values and sufficient accuracy except the classifier SVM of training days (8 to 28) on testing days (1 to 3). The R^2 values in the first case are 0.85 and 0.93 while they are 0.81 and 0.68 in the second case for both classifier the KNN and SVM respectively.

Likewise, the second scenario, the three-week training on one-day testing, presented satisfactory prediction of the delamination depths. Two cases as well have been adopted in the present scenario. Training days (1 to 21) on testing day 22 and training days (8 to 28) on testing day 1. R^2 values of the classifiers are 0.97 and 0.96 in the first case for both the KNN and SVM sequentially. While they are 0.68 and 0.88 in the second case as shown in Figure (4-22).

Tables (4-9) and (4-10) depict in detail the estimated depths in each case for both scenarios that are adopted here. In addition, the accuracy of each depth is listed as well.

In such scenarios, the procedure employs 672 observations to train the data and create the predicting models, which handed a good agreement in estimating the depths since the testing data are 96 and 32 for the three-day and one-day respectively. The utilized features, the majors and minors are still 48 for the input and one for the output, which is the depths.

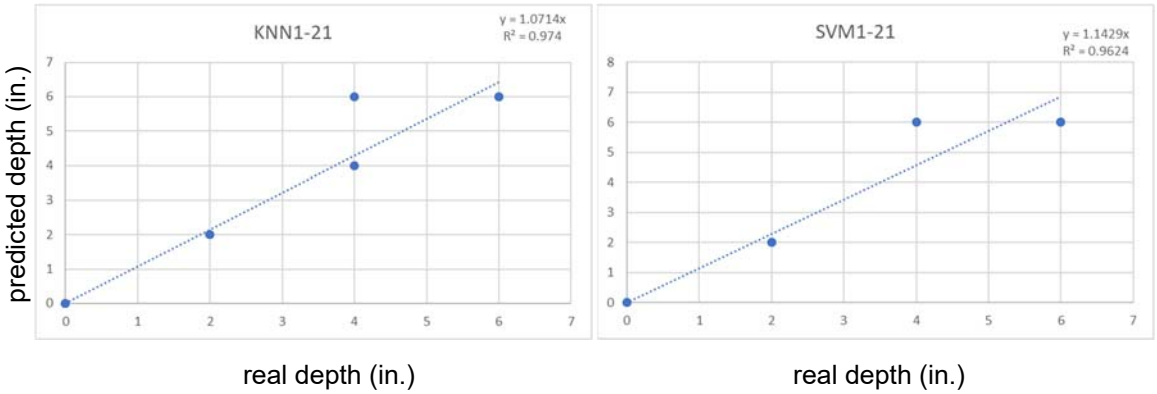

Figure 4-22: Fitting diagrams for three-week training on three-day and one-day testing.

Table 4-9: The calculated depths of the delamination, case three-week on three-day.

	Case 1		Case 2	
	KNN (in)	SVM (in)	KNN (in)	SVM (in)
Sound	0	0	0	0
Defect 2-in.	1.70	1.86	1.62	1.45
Defect 4-in.	3.39	3.72	3.24	2.91
Defect 6-in.	5.09	5.58	4.86	4.36

Table 4-10: The calculated depths of the delamination, case three-week on one-day.

	Case 1		Case 2	
	KNN (in)	SVM (in)	KNN (in)	SVM (in)
Sound	0	0	0	0
Defect 2-in.	2.14	2.29	1.73	2.21
Defect 4-in.	4.29	4.57	3.47	4.43
Defect 6-in.	6.43	8.86	5.20	6.64

4-8-4-3-8 Two-week Training on Three-day and One-day Testing

The last scenario that has been utilized is by training two weeks of thermal images and testing three days and one day of IR datasets, respectively. Two situations have been fulfilled for each scenario, training days (1 to 14 and 15 to 28) and testing days (22 to 24 and 1 to 3) respectively. The second scenario was training days (1 to 14 and 15 to 28) and testing days (15 and 1) sequentially. R^2 values acquired in the first case are 0.61 and 0.57 for the KNN and SVM respectively with a precision of -8% and -25%. In addition, values 0.65 and 0.71 of R^2 have been earned in the second case with accuracy of -35% and -29% for both the KNN and SVM classifiers. Figure (4-23) illustrates the two cases that have been adopted in the first scenario. Table (4-11) shows the predicted depths for two cases, similarly in the second scenario two cases have been completed with acceptance corresponding results. The

R^2 values are 0.74 and 0.88 with an accuracy of -2% and +18% for both classifiers the KNN and SVM sequentially. The second got an exceptional agreement especially for the SVM classifier. The results were 0.52 and 0.95 for the R2 with a precision of -19% and +7% as stated in Figure (4-24). Details are summarized in Table (4-12) that shows the predicted depths for each delamination in the concrete specimen for both the KNN and SVM learners.

As mentioned previously, the two-week training model adopted 448 observations to estimate the depths in the testing of 96 and 32 observations, the three and one days, respectively.

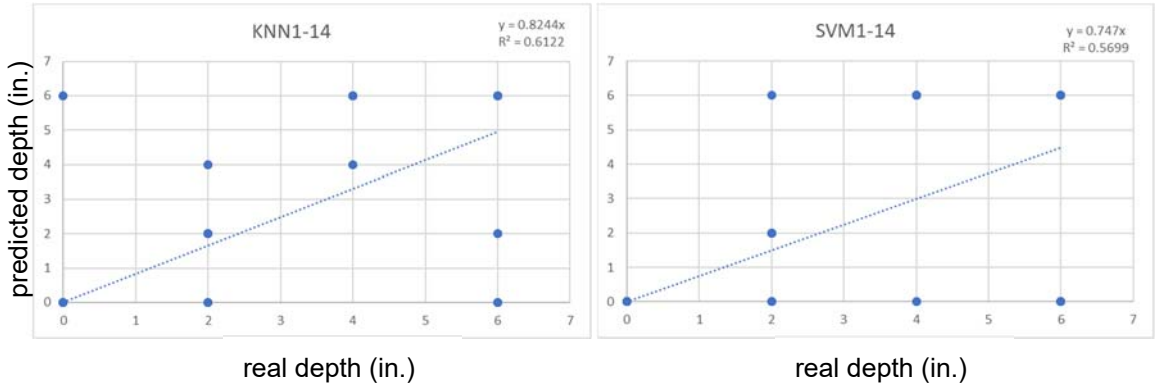

Figure 4-23: Fitting diagrams for two-week training on three-day testing.

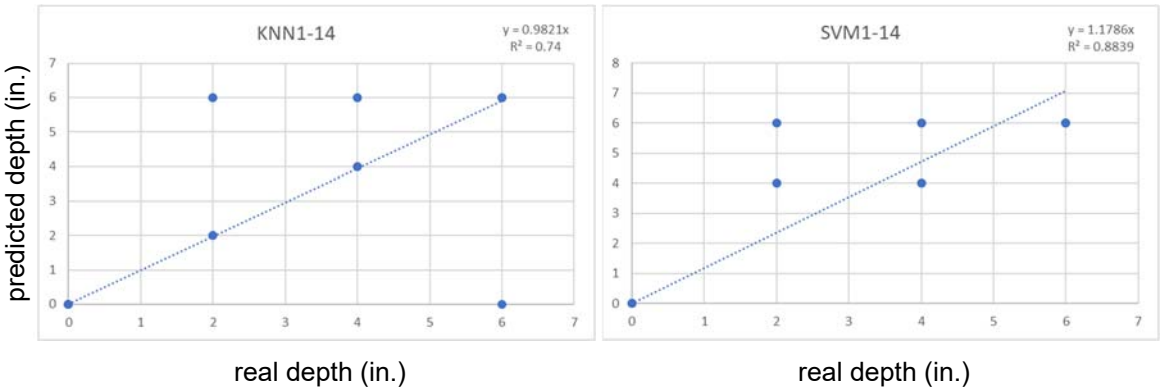

Figure 4-24: Fitting diagrams for two-week training on one-day testing.

Table 4-11: The calculated depths of the delamination, case two-week on three-day.

	Case 1		Case 2	
	KNN (in)	SVM (in)	KNN (in)	SVM (in)
Sound	0	0	0	0
Defect 2-in.	1.65	1.49	1.30	1.43
Defect 4-in.	3.30	3.00	2.60	2.86
Defect 6-in.	4.95	4.48	3.89	4.29

Table 4-12: The calculated depths of the delamination, case two-week on one-day.

	Case 1		Case 2	
	KNN (in)	SVM (in)	KNN (in)	SVM (in)
Sound	0	0	0	0
Defect 2-in.	1.96	2.36	1.04	2.14
Defect 4-in.	3.93	4.71	2.07	4.29
Defect 6-in.	5.89	7.70	3.11	6.43

4-8-4-3-9 One-week Training on One-day Testing

The current scenario adopted four cases as illustrated in Figure (4-25). Two weeks have been selected, days (1 to 7) and days (15 to 2). However, the first week, days (1 to 7) tested days 8 and 15, respectively while the second week, days (15 to 21) inspected days 22 and 1 sequentially. As previously, the two learners the KNN and the SVM were used in the analysis. Good accuracies and R^2 values have been obtained except the case of training days (15 to 21) on testing day 1, the SVM learner, where the precision and the R^2 values were under the average.

The total number of observations are 224 for one week processing. Total number of major and minor features are 48 plus the depth.

The obtained results are 0.75, 0.76, 0.85 and 0.86 of R^2 values for the case, the training of days (1 to 7) on testing day 8 and day 15, respectively. While the R^2 are 0.93, 0.93, 0.79 and 0.64 for the second week, training week (15 to 21) on testing days 22 and 1, respectively. Table (4-13) summarized all the predicted depths and their errors which are in very good results.

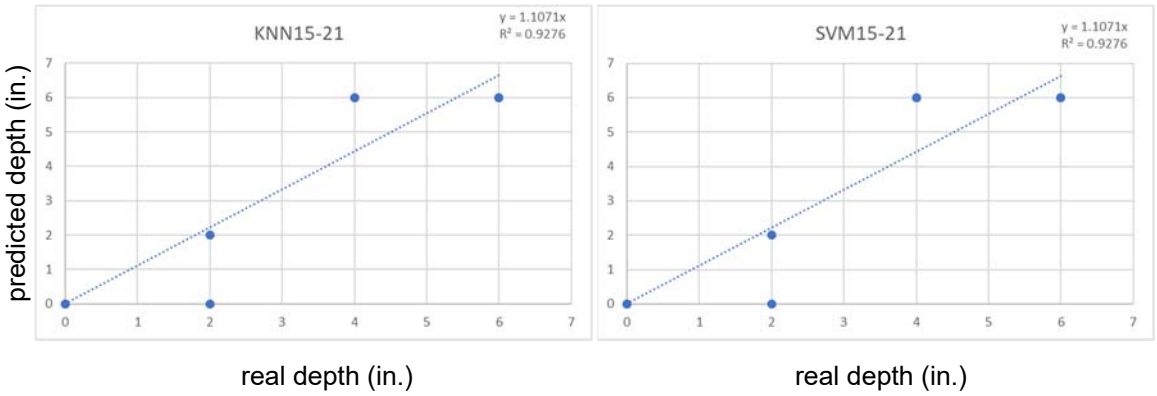

Figure 4-25: Fitting diagrams for one-week training on one-day testing.

Table 4-13: The calculated depths of the delamination, case one-week on one-day.

	Case 1		Case 2		Case 3		Case 4	
	KNN (in)	SVM (in)	KNN (in)	SVM (in)	KNN (in)	SVM (in)	KNN (in)	SVM (in)
Sound	0	0	0	0	0	0	0	0
Defect 2-in.	2.43	2.29	2.21	2.21	2.14	2.36	1.50	1.29
Defect 4-in.	4.86	4.57	4.43	4.43	4.29	4.71	3.00	2.57
Defect 6-in.	7.29	6.86	6.64	6.64	6.43	7.07	4.50	3.86

4-8-4-3-10 Three-day Training on One-day Testing

The last scenario was training three-day model and testing one-day datasets. Eight cases with four groups of three-day have been achieved in this scenario, Figure (4-26). These the four groups of three-days are: days (1 to 3), days (8 to 10), days (15 to 17), and days (22 to 24). Each three-day group has been trained then tested on a day that is from a different week. For example,

days (1 to 3) tested day 8 and day 15, days (8 to 10) tested day 1 and day 22, days (15 to 17) tested day 1 and day 22, and the last one was days (22 to 24) tested day 8 and day 15. The purpose of that was to examine the results from different weeks which have different environmental conditions. The gained outcomes were in good convenient level. The R^2 values are in most cases above the average values except the case of days (8 to10) on day 1 and day 22. Otherwise, the accuracies of the fitting diagrams ranged from -25% to +21% except the case days (8 to 10) on day 1.

All the results of the eight cases have been illustrated in Table (4-14) with their errors.

The number of observations that have been taken in this case was 96 since there 32 observations per day. The number of all features are 48 ones.

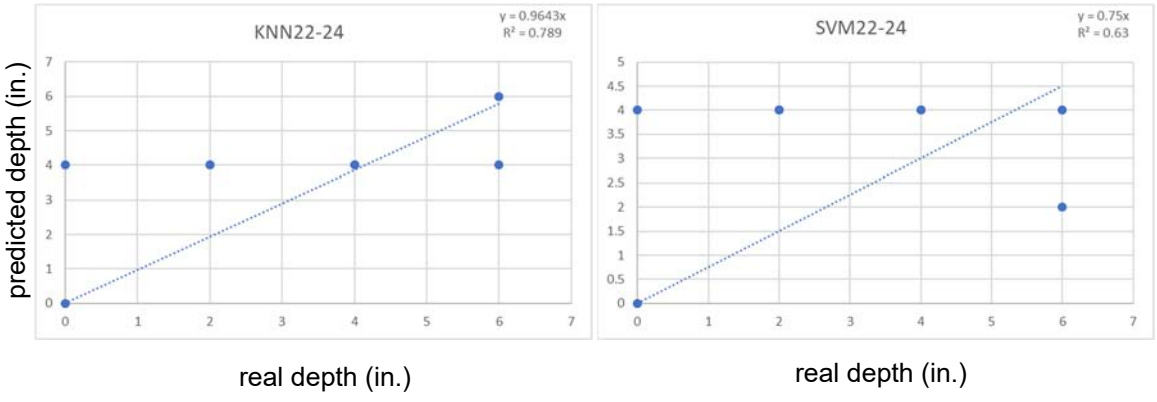

Figure 4-26: Fitting diagrams for three-day training on one-day testing.

Table 4-13: The calculated depths of the delamination, case three-day on one-day.

	Case 1		Case 2		Case 3		Case 4	
	KNN (in)	SVM (in)	KNN (in)	SVM (in)	KNN (in)	SVM (in)	KNN (in)	SVM (in)
Sound	0	0	0	0	0	0	0	0
Defect 2-in.	2.43	2.43	1.77	1.07	2.29	1.98	1.64	1.79
Defect 4-in.	4.86	4.86	3.54	2.14	5.47	3.96	3.29	3.57
Defect 6-in.	7.29	7.29	5.30	3.21	6.86	5.95	4.93	5.36

Table 4-13: The calculated depths of the delamination, case three-day on one-day (continued).

	Case 5		Case 6		Case 7		Case 8	
	KNN (in)	SVM (in)	KNN (in)	SVM (in)	KNN (in)	SVM (in)	KNN (in)	SVM (in)
Sound	0	0	0	0	0	0	0	0
Defect 2-in.	2.04	2.57	1.95	1.84	1.86	1.79	1.93	1.50
Defect 4-in.	4.07	5.14	3.89	3.68	3.71	3.57	3.86	3.00
Defect 6-in.	6.11	7.71	5.84	5.52	5.57	5.36	5.79	4.50

4-9 Summary

Table (4-15) summarizes all the cases that have been accomplished in each scenario. In some cases, the training period has the same testing period (same observation). Moreover, the training period has been doubled or tripled or more, for instance 2 weeks vs 1 week and 3 weeks vs 1 week or 3 weeks vs 3 days. It was taken into consideration that the testing periods are not included in the training periods which means that taking the variations of environmental conditions in the analysis.

Table 4-15: The summary of all scenarios taken in the research.

Case	Days	R^2		Error %	
		KNN	SVM	KNN	SVM
2W on 2W	(1-14) on (15-28)	0.58	0.60	-23	-22
	(1-14) on (15-28)	0.71	0.74	-17	-7
1W on 1W	(8-14) on (1-7)	0.76	0.80	-5	+1
	(1-7) on (8-14)	0.60	0.68	-10	-4
	(15-21) on (22-28)	0.69	0.87	-1	+7
	(15-21) on (1-7)	0.68	0.60	-10	-22
3D on 3D	(1-3) on (4-6)	0.57	0.61	-18	-5
	(22-24) on (15-17)	0.67	0.57	-20	-16
	(1-3) on (15-17)	0.71	0.71	+10	+6
	(15-17) on (1-3)	0.71	0.76	-10	-7
1D on 1D	2 on 1	0.71	0.56	-12	-36
	8 on 1	0.82	0.64	-18	-4
	16 on 15	0.60	0.72	-22	-29
3W on 1W	(1-21) on (22-28)	0.82	0.87	+6	-1
	(8-28) on (1-7)	0.76	0.73	-5	-11
2W on 1W	(1-14) on (15-21)	0.55	0.61	-26	-17
	(15-28) on (1-7)	0.65	0.71	-22	-14
	(1-7&15-21) on (8-14)	0.59	0.70	-10	-6
	(8-14&22-28) on (1-7)	0.69	0.73	-5	-14
3W on 3D	(1-21) on (22-24)	0.85	0.93	+16	+8
	(8-28) on (1-3)	0.81	0.68	-14	-27
3W on 1D	(1-21) on 22	0.97	0.96	+7	+14
	(8-28) on 1	0.68	0.88	-13	+11
2W on 3D	(1-14) on (22-24)	0.61	0.57	-18	-25
	(15-28) on (1-3)	0.65	0.71	-35	-29
2W on 1D	(1-14) on 15	0.74	0.88	-2	+18
	(15-28) on 1	0.52	0.95	-49	+7
1W on 1D	(1-7) on 18	0.75	0.76	+21	+14
	(15-21) on 22	0.93	0.93	+11	+11
	(1-7) on 15	0.85	0.86	+7	+18
	(15-21) on 1	0.79	0.64	-25	-35
3D on 1D	(1-3) on 8	0.75	0.74	+21	+21
	(8-10) on 1	0.85	0.57	-12	-46
	(1-3) on 15	0.80	0.87	+14	-1
	(8-10) on 22	0.46	0.64	-18	-11
	(15-17) on 1	0.63	0.86	+2	+29
	(22-24) on 8	0.74	0.68	-3	-8
	(15-17) on 22	0.69	0.68	-7	-11
	(22-24) on 15	0.79	0.63	-4	-25

4-10 Assessment of Depth Estimation

A forecasting model has been adopted in the current study to evaluate the linear regressions of the predicted depths in delamination. The mean absolute percentage error (MAPE) is considered as a common method to assess differences between two groups of datasets. The method calculates the average values in these datasets [118]. The MAPE can be computed according to the current mathematical expression:

$$MAPE\ (\%) = \frac{1}{N}\sum_{i=1}^{N}\left[\frac{D_{est}-D_{real}}{D_{real}}\right] \times 100 \qquad (4.11)$$

where D_{est} = the estimated depths in delamination

D_{real} = the real depths in delamination

N = the total number of evaluated depths

It was primarily developed by Lewis in 1982 and the rating of this method is according to Table (4-16) which had some improvement on its values in 1997 [97]. However, the model was used to verify and assess the differences between the real depths and the predicted depths in the current study. The Table indicates that the smaller obtained values the better results.

Table 4-16: The typical values of the mean absolute percentage error (MAPE).

MAPE	The accuracy of data
<10%	Very good
11%-20%	Good
21%-30%	Reasonable
>30%	Inaccurate

Table (4-17) illustrates all the MAPE values of the models that have been developed to estimate depths in delamination. Most the results are in good agreement according to Table (4-16) except one case that has more than 30% which is case 2 in (3D on 1D) (SVM). Moreover, some cases have percentage error more than 20%, such two cases in the mode 1D on 1D, one case in 2W on 3D and one case in 1W on 1D. Otherwise, all the remained cases are below (20%) error which gives a good indication for the predicated depths.

All results with valued under 10% in Table (4-17) have been highlighted since they give a very good prediction values according to Table (4-16).

Table 4-17: The values of MAPE of the training models.

Model	MAPE (%)							
	case 1		case 2		case 3		case 4	
	KNN	SVM	KNN	SVM	KNN	SVM	KNN	SVM
2W on 2W	17.52	16.23	1.11	5.21				
1W on 1W	3.79	0.85	0.44	3.38	0.85	5.35	0.72	16.88
3D on 3D	13.40	3.65	1.34	12.00	7.88	4.23	0.69	5.35
1D on 1D	8.67	26.73	1.62	2.63	16.65	21.38		
3W on 1W	4.17	0.75	0.31	7.98				
2W on 1W	17.15	14.27	1.52	10.40	7.40	4.83	0.34	10.40
3W on 3D	11.35	5.25	1.30	20.52				
3W on 1D	5.35	19.10	0.91	7.98				
2W on 3D	13.13	18.96	2.39	21.38				
2W on 1D	1.40	16.02	3.28	5.35				
1W on 1D	16.13	10.77	0.73	7.98	5.35	13.40	1.70	26.73
3D on 1D	16.13	16.13	0.79	34.88	16.40	0.71	1.22	7.98
	case 5		case 6		case 7		case 8	
3D on 1D	1.40	21.38	0.18	6.00	5.35	7.98	0.24	18.75

4-11 Limitations

In the current analysis, the estimation of defect depths was conducted over a period of time more than one month. In real life, implementation of a test on concrete deck slab has several limitations that would affect the results of estimation, such as the time course of the test, sampling interval between thermal images and number of extracted features employed in building predictive models. However, two cases have been adopted to present some limitations on predicting depths, the training days (15 to 21) on testing day (22) and training days (1 to 3) on testing day (15).

As concluded from chapter three, the small interval sample for a specimen being inspected provides better result in detection deeper defects. So, the interval of 1-minute will be used in the analysis. The process of predicting depths by employing all major and minor features might take some time to train and test datasets. So, the analysis will include estimating defects by using only major features in sequence.

The process was conducted into two stages. First was by taking major features, the pixel, the phase, the amplitude, and the frequency in sequence to build predictive models for both classifiers, the KNN and the SVM. The next stage was estimating depths in delamination by utilizing the previous models and calculating both values of R^2 and the error.

It is obviously seen, in Table (4-18) case 1, adopting only the major feature of pixel produced a reasonable value in the accuracy of building predictive models. By considering the features of the phase and the amplitude, the precision of predictive models acquired improved results. On the other hand, conducting the feature of the frequency in the analysis reduces the accuracy of the predictive model. But, that does not mean diminishing the importance of the frequency feature with their minors as concluded in fitting diagrams in the previous sections. Nevertheless, the predictive models have

been employed to estimate depths in delamination to assess the major features used in the current process. Table (4-19) shows that using only pixels in prediction gives reasonable results of R^2 and the accuracy in estimating depths as well adding the two features, the phase and amplitude, might improve results especially when the period length of inspection is big, for instance one week instead of three days. In the case of three-day training, using both features, the phase and amplitude would not rise the estimation which might refer to the number of days used in the analysis. Both cases illustrated that adding the feature of the frequency would not progress the results of depth estimation unless using the minor features with them.

Table 4-18: The accuracy of predictive models by using major features in sequence.

Training days (15 to 21)					
No.	**Cases**	**No. of Features**	**Observations**	**Accuracy (%)**	
				KNN	**SVM**
1	pixels	4	224	87.9	73.7
2	pixels + phases	8	224	90.6	83.5
3	pixels + phases + amp	12	224	94.6	92.9
4	pixels + phases + amp + freq	16	224	82.1	84.4
Training days (1 to 3)					
5	pixels	4	224	84.4	84.4
6	pixels + phases	8	224	92.7	95.8
7	pixels + phases + amp	12	224	91.7	93.8
8	pixels + phases + amp + freq	16	224	83.3	89.6

Table 4-19: Illustrates the values of R^2 and error of estimating defect depths.

Training days (15 to 21) on day (22)				
	KNN		**SVM**	
	R^2	**Error %**	**R^2**	**Error %**
Case 1	0.69	-25	0.64	-4
Case 2	0.36	-66%	0.69	+29
Case 3	0.54	+12.5	0.65	+25
Case 4	0.54	+12.5	0.64	+25
Training days (1 to 3) on day (15)				
Case 5	0.51	-44	0.44	-56
Case 6	0.44	-37	0.58	-36
Case 7	0.34	-59	0.29	-57
Case 8	0.38	-59	0.30	-65

CHAPTER FIVE

5- CONCLUSIONS AND RECOMMENDATIONS FOR THE FUTURE WORKS

5-1 Introduction

Chapter five sums up all the main conclusions and the future recommendations of the automated time-lapse thermography data processing and the determination of depths in delamination in reinforced concrete structures.

5-2 Time-Lapse Thermography Data Processing

The restricted use of infrared thermography for bridge deck inspection can be largely attributed to its inability to accurately characterize defects deeper than 2 inches from the surface and requirements for ideal environmental conditions during the inspection process. The current study developed a framework that improves the detectability of deeper defects in concrete using passive thermography at rates comparable to advanced NDT approaches such as radar and sounding methods. The framework consisted of four key data processing engines: a pre-processing module which de-trends

and normalizes the raw IR data, followed by a pixel-wise multiscale data decomposition, which analyzes the time-frequency distribution of temperature variations with respect to defect depth. A series of image processing techniques are subsequently developed to enhance the contrast between defective and non-defective regions. The resulting high contrast composite image is then passed through a defect localization engine which utilizes active contour models to automatically detect the boundary location of defects in the composite image. Finally, experiments are conducted to identify key settings necessary for implementing the proposed framework for automated time-lapse thermography (A-TLT). Based on the objective of the research, the following conclusions can be made:

1. *Improving sub-surface defect detectability*: Multiscale data decomposition assists in separating the acquired temperature response information into modes based on depth from the surface. In raw forms, temperature variations from shallow defects tend to mask those from deeper ones; the ability to be able to uniquely isolate them improves the detectability of deep defects. The proposed framework was able to localize defects irrespective of the inspection season (winter, fall, summer, spring, or month) in which

the data was collected. However, the magnitude of contrast between defective and non-defective regions was higher during periods of longer days and shorter nights. For very thick concrete objects, it is recommended that IR imaging to be performed on both sides to capture all sub-surface defects. The results presented in this study shows that defects can be detected by imaging from either the sunny or shady sides of the block specimen, although the magnitude of image contrast is higher on the shady side. On the sunny side, the extremely high pixel intensity of shallow defects tends to mask the intensity of the deeper ones.

2. *Investigating sampling rates and data collection periods for conducting TLT*: It was shown in the study that smaller sampling intervals generally improved the normalized image contrast for subsurface defects regardless of depth. It was observed that an IR camera image sampling rate of 1 image every 10 min over a period of 3 days was enough to visualize defects greater than 3 in. in depth. The sampling rate of the IR camera was found to be inversely related to the duration of data collection. At low camera sampling rates, the

duration of data collection needs to be increased (and vice-versa) to improve the detection rates of deeper defects.

3. *Performing a comparative analysis of the framework with traditional approaches*: The A-TLT processing produced increased contrasts for simulated defects at depths of 3 and 5 in. as compared with maximized conventional IRT images and TLT images processed using the four-point method. It was found that the normalized contrast for A-TLT processed images increased with increasing data collection periods. The A-TLT processing methodology provided improved normalized contrast as compared with four-point data. The A-TLT processing methodology provided improved normalized contrast as compared with the maximized conventional IRT images when data collection intervals were adequately long, greater than three days for the 3 in. deep simulated defect and greater than 15 days for the 5 in. deep simulated defect.
4. *Limitations*: The study was conducted over a long period of time. Although this is impractical for real inspection, the results showed that continuously acquiring data for 3 days was enough to detect

deeper defects. To reduce data acquisition time, it is recommended to increase the IR camera frame rate to achieve comparable results.

5-3 Determination of Defect Depths in Concrete Structures

In the last decades, the active thermography approach has been significantly used for estimating depths in defects in several materials such as metals, plastics, composite materials and as well in reinforced concrete materials. Moreover, in the active thermography, the circumstances in experimental works are held under controlled situation such as frequency of a test, excitation of heating and distances between heating sources and specimens. However, many researchers have developed many means and techniques to estimate depths in defects by adopting equations and empirical models as functions of several parameters and variables, for instance phase contrast, frequency, thermal contrast, time, and material properties.

In the current study, a reinforced concrete specimen was inspected under a direct energy from the sun, which is called the passive thermography concept. Many factors, such as solar, daytime, nighttime, wind, cloud, and shadow have impacts on the tests. Consequently, the models that have been adopted by the active thermography are not convenient with the passive

thermography. Therefore, the Machine Learning (ML) has been presented as a substitutional approach since it deals with features. Furthermore, the Fast Fourier Transform (FFT) was used to extract features from the defect and non-defect areas, for example phases, amplitudes, and frequencies. Finally, the extracted features have been trained by classifier learners, the SVM and KNN, to build appropriate models which are utilized to test other datasets for predicting the delamination depths in the concrete specimen. According to the objectives of the current study, several conclusions have been presented:

1. Using the Fast Fourier Transform (FFT) approach has a good assistance in extracting features from the defects and non-defect regions. Phase, amplitudes, and frequencies have been excerpted from delamination and sound areas to give each defect its particularity and characteristic. In addition, other features have been added, such as the differentiation between the pixel values of the defect and non-defect spots at varies times for each day.
2. *Dividing the delamination into parts*: This process has improved the results in two sides. The first side was by smoothing the behavior of each defect and diminishing the noise at the edges of each defect. The process with 48 features contributed to boost the accuracy of models

with 98.7% and 98.9% while the accuracy values were 80.4% and 89.3% when a one part was used for each defect for the KNN and the SVM respectively. In addition, when using a process with 16 features, only major features, the accuracy values were increased from 29.5% and 38.4% to 83.0% and 83.9% for both the KNN and SVM respectively. The second advantage of splitting the defects was by increasing the number of observations in the analysis. The more observation the more accuracy is obtained of building models and predicting depths.

3. *Major features*: There are four major features that have been utilized in training models. FFT has been used to assist extracting three major features: the phases, the amplitudes, and the frequencies. The fourth major feature has been mined by taking the differentiation between several thermal images over a period of time. However, the most important feature is the differentiation between pixel because it has two impact effects. The first influence is by displaying the attitude of each defect for a specific period of time such as between 6:00 am-12:00 pm, so the learners could distinguish each defect depth on that process of time. The second trace, which is concluded from the effect, is

improving the accuracy from 78.3% and 79.1% into 83% and 83.9% for the KNN and the SVM respectively in cases 9 and 10, Table (4-2). The phases and amplitudes, moreover, have no less important impact on the process than the differentiation. The progressive analyses in Table (4-2) illustrates the weight of each feature. For the frequency, as depicted in Table (4-2), the training obviously showed less improving in accuracy throughout models. Nevertheless, using all the obtained features with the sub-features (the minors) award better constructed models with high precision.

4. *Minor features*: The minor features, or called sub-features, have a direct connection with the major features. Adding these minor features strengthened building the models by raising their accuracy. The classifiers started placing each dataset of features in their classes that they belong to. This procedure has been accomplished by taking the average of each major feature and subtracting the minimum and maximum values for each group. The analysis showed that adding the minor features increases the precision from 83% into 98.7% for the KNN classifier, for example the cases 7 and 8 in Table (4-2). On the other hand, this process maximized the number of features to 48

columns instead of 16 columns, which is triple times columns of the major features. As mentioned in section (4-8-4-2), the more features are trained the more accurate models that are obtained for predicting depths in concrete specimens.

5. *Fitting Diagrams*: Several tests on estimating depths have been accomplished via different datasets. The analyses have been grouped into parts depending on the number of observations between the trained and tested datasets. However, the groups that have been selected might have the same observation number, for instance two-week training on two-week testing, or have double, or triple or a greater number of observations, for example two-week training on one-week testing and three-week training on three-day testing. It has been taking into consideration that the dataset period testing is not included from the training period. Moreover, it is important to include the differentiations of environmental circumstances between these datasets. Anyhow, twelve scenarios have been completed with several cases each. It is obvious that the cases that have the same period for training and testing datasets have R^2 values within the average. These values ranged between 0.57 to 0.82 for all the cases that have the same observations.

In addition, the accuracy in some cases reached to -1% and +1%. It is proved from the analyses that increasing the observations number of training period than the testing period leads to maximize the R^2 values. The training period of 3 weeks that has tested the periods of 1 week, 3 days and 1 day has the best results for both R^2 values and their precisions in predicting the depths in delamination. The values of R^2 reach to 0.97 and the best accuracy is between -1% and +1%. Moreover, the MAPE method has shown that the use of the Machine Learning gave acceptance results since only one training model has a value more than 30%, which refers to inaccurate model. Some values of the MAPE ranged in twentieth and most of them are less than 20%. This impression of the results tells that using the Machine Learning to predict depths is a good indication especially with the passive thermography where all the models that are employed in previous researches in the active thermography did not work with the passive thermography.

5-4 Recommendations

The current research has contributed to calibrate the infrared data in the field to enable the quantification of depth in defects in concrete bridge components. Several recommendations are suggested to improve the current research and some tasks for the future works as follows:

1. Evaluating the current study by taking the effect of the size of defects on the proposed framework. The size of defects was kept constant at different depths. Under real-world conditions, the size, shape, and depth of defects vary simultaneously. This will be considered in future studies. The biggest challenge with time-lapse thermography is how to store, process, and manage the large volumes of data (due to continuous imaging) for large-scale inspection.
2. Developing and evaluating a framework to calibrate the infrared thermography data processing in the field by covering concrete specimens with asphalt overlays with several thicknesses. The research should take study through the processing of thermal images before and after the overlays.

3. Proposing and building learner models depending on several sizes, shapes, and depths of delamination in the reinforced concrete structures. This process will widely extend and boost the trained models on estimating the depths in defects in reinforced concrete components.
4. Taking into consideration the effect of the Wavelet Transform approach in constructing the trained models. This technique will take the impact of environmental parameters with different frequency domains and investing the decomposed modes to predict the depths. Furthermore, this process will increase the number of features, equal to the number of modes multiplies the original features, that are employed in building the classifier models.

BIBLIOGRAPHY

1. Washer, G., *Advances in the use of thermographic imaging for the condition assessment of bridges.* Bridge Structures, 2012. **8**(2): p. 81-90.

2. Bertolini, L., et al., *Corrosion of steel in concrete*. Vol. 392. 2013: Wiley Online Library.

3. Choi, M., et al., *Quantitative determination of a subsurface defect of reference specimen by lock-in infrared thermography.* Ndt & E International, 2008. **41**(2): p. 119-124.

4. Maser, K.R. and W.K. Roddis, *Principles of thermography and radar for bridge deck assessment.* Journal of transportation engineering, 1990. **116**(5): p. 583-601.

5. Russell, H.G., *Concrete bridge deck performance*. Vol. 333. 2004: Transportation Research Board.

6. Ghorbanpoor, A. and N. Benish, *Non-destructive testing of Wisconsin highway bridges*. 2005: Wisconsin Highway Research Program.

7. Bremner, T., et al., *ACI 222R-01 protection of metals in concrete against corrosion.* American Concrete Institute, Farmington Hills, 2001.

8. Yehia, S., et al., *Detection of common defects in concrete bridge decks using nondestructive evaluation techniques.* Journal of Bridge Engineering, 2007. **12**(2): p. 215-225.

9. Olson, L.D., Y. Tinkey, and P. Miller, *Concrete bridge condition assessment with impact echo scanning*, in *Emerging Technologies for Material, Design, Rehabilitation, and Inspection of Roadway Pavements*. 2011. p. 59-66.

10. Maierhofer, C., *Nondestructive evaluation of concrete infrastructure with ground penetrating radar*. Journal of materials in civil engineering, 2003. **15**(3): p. 287-297.

11. Parrillo, R., R. Roberts, and A. Haggan, *Bridge deck condition assessment using ground penetrating radar.* Proceedings of the ECNDT, Berlin, German, 2006. **2526**: p. 112.

12. Moore, M., et al., *Reliability of visual inspection for highway bridges, volume I*. 2001.

13. Adminstration, F.H., *Deficient Bridges by Functional Classification Count 2015*. 2015.

14. Sultan, A.A. and G.A. Washer, *Reliability analysis of ground-penetrating radar for the detection of subsurface delamination.* Journal of Bridge Engineering, 2017. **23**(2): p. 04017131.

15. Bolleni, N.K., *Environmental effects on subsurface defect detection in concrete structures using infrared thermography*. 2009: University of Missouri-Columbia.

16. Fenwick, R.G., *Environmental effects on subsurface defect detection in concrete without solar load*. 2010, University of Missouri--Columbia.

17. Kass, M., A. Witkin, and D.J.I.j.o.c.v. Terzopoulos, *Snakes: Active contour models.* 1988. **1**(4): p. 321-331.

18. Sultan, A.A., *Advancements in evaluating reliability of nondestructive technologies for the detection of subsurface fracture damage in RC bridge decks*. 2017, University of Missouri--Columbia.

19. Gucunski, N. and N.R. Council, *Nondestructive testing to identify concrete bridge deck deterioration*. 2013: Transportation Research Board.

20. Miller, T.H., *Nondestructive inspection of corrosion and delamination at the concrete-steel reinforcement interface.* 2010.

21. Carino, N., *Methods to evaluate corrosion of reinforcement.* Handbook on Nondestructive Testing of Concrete, 2004: p. 11-1.

22. Liu, Y., *Modeling the time-to corrosion cracking of the cover concrete in chloride contaminated reinforced concrete structures*. 1996, Virginia Tech.

23. Yuan, Y., Y. Ji, and S.P. Shah, *Comparison of two accelerated corrosion techniques for concrete structures.* ACI Structural Journal, 2007. **104**(3): p. 344.

24. Rumbayan, R., *Modeling of environmental effects on thermal detection of subsurface damage for concrete bridges*. 2013: University of Missouri-Columbia.

25. Jana, D. *Delamination–A State-of-the-art Review*. in *Proceedings of the Twenty-ninth Conference on Cement Microscopy Quebec City, PQ, Canada*. 2007.

26. (PCA), P.C.A., *Types and causes of concrete deterioration.* PCA, 2002.

27. Standard, A., *D4580: Standard Practice for Measuring Delaminations in Concrete Bridge Decks by Sounding, ed.* West Conshohocken, PA: ASTM International, 2012.

28. Scott, M., et al., *A comparison of nondestructive evaluation methods for bridge deck assessment.* ndt & E International, 2003. **36**(4): p. 245-255.

29. Davis, A., et al., *Nondestructive test methods for evaluation of concrete in structures.* American Concrete Institute, ACI, 1998. **228**.

30. Carino, N.J., *The impact-echo method: an overview.* Structures 2001: A Structural Engineering Odyssey, 2001: p. 1-18.

31. ASTM, C. *1383-98a" Standard Test Method for Measuring the P-Wave Speed and the Thickness of Concrete Plates Using the Impact-Echo Method,"*. in *American Society for Testing and Materials*. 2006.

32. Rhazi, J., *NDT in civil engineering: the case of concrete bridge decks.* CSNDT JOURNAL, 2000. **21**(5): p. 18-25.

33. ASTM, *Standard test method for evaluating asphalt-covered concrete bridge decks using ground penetrating radar*. 2008.

34. Harris, K. and H. Melo, *Application of Thermal IR Imagery for concrete bridge inspection*. 2011, CEE.

35. Washer, G., R. Fenwick, and N. Bolleni, *Effects of solar loading on infrared imaging of subsurface features in concrete.* Journal of Bridge Engineering, 2010. **15**(4): p. 384-390.

36. 122, A.C. *Guide to thermal properties of concrete and masonry systems*. 2002. American Concrete Institute.

37. McKeel, W.T. and G.G. Clemena, *The applicability of infrared thermography in the detection of delamination in bridge decks*. 1977, Virginia Transportation Research Council.

38. Branco, F.A. and P.A. Mendes, *Thermal actions for concrete bridge design.* Journal of Structural Engineering, 1993. **119**(8): p. 2313-2331.

39. Lienhard, J., *A Heat Transfer Textbook. 2011.* Mineola, NY: Dover Publications.

40. Washer, G., et al., *Guidelines for thermographic inspection of concrete bridge components in shaded conditions.* Transportation research record, 2013. **2360**(1): p. 13-20.

41. Washer, G., et al., *Field Testing of Hand-Held Infrared Thermography, Phase II TPF-5 (247) Interim Report*. 2015, Missouri. Dept. of Transportation. Division of Construction and Materials.

42. Chase, S., Y. Adu-Gyamfi, and P. Tunuguntla. *Bridge deck sub-surface defect detection using time-lapse thermography*. in *TRB 94th Annual Meeting*. 2015.

43. Dawson, J., *Experimental assessment of advanced thermal imaging for detecting voids in ducts*. 2017, University of Missouri--Columbia.

44. Washer, G., et al., *Development of hand-held thermographic inspection technologies.* Materials Evaluation, 2008. **66**(3).

45. Avdelidis, N., et al. *Structural integrity assessment of materials by thermography*. in *Conf. Damage in Composite Materials CDCM, Stuttgart, Germany*. 2006. Citeseer.

46. Maldague, X.P.J.M.E., *Introduction to NDT by active infrared thermography.* 2002. **60**(9): p. 1060-1073.

47. Rumbayan, R. and G. Washer, *Modeling of environmental effects on thermal detection of subsurface damage in concrete.* Research in Nondestructive Evaluation, 2014. **25**(4): p. 235-252.

48. Weritz, F., et al., *Intestigation of concrete structures with pulse phase thermography*. 2005. **38**(9): p. 843-849.

49. Maierhofer, C., et al., *Application of impulse-thermography for non-destructive assessment of concrete structures.* 2006. **28**(4): p. 393-401.

50. Sakagami, T., S.J.I.P. Kubo, and Technology, *Development of a new non-destructive testing technique for quantitative evaluations of delamination defects in concrete structures based on phase delay measurement using lock-in thermography.* 2002. **43**(3-5): p. 311-316.

51. Ranjit, S., et al., *Investigation of lock-in infrared thermography for evaluation of subsurface defects size and depth.* 2015. **16**(11): p. 2255-2264.

52. Milovanović, B. and I.J.J.o.I. Banjad Pečur, *Review of active IR thermography for detection and characterization of defects in reinforced concrete.* 2016. **2**(2): p. 11.

53. Cotič, P., et al., *Determination of the applicability and limits of void and delamination detection in concrete structures using infrared thermography*. Ndt & E International, 2015. **74**: p. 87-93.

54. Huh, J., et al., *Detectability of Delamination in Concrete Structure Using Active Infrared Thermography in Terms of Signal-to-Noise Ratio.* Applied Sciences, 2018. **8**(10): p. 1986.

55. Tran, Q.H., et al., *Detectability of Subsurface Defects with Different Width-to-Depth Ratios in Concrete Structures Using Pulsed Thermography.* Journal of Nondestructive Evaluation, 2018. **37**(2): p. 32.

56. Milovanović, B. and I.B. Pečur. *Determination of material homogeneity using infrared thermography*. in *V Pan American Conference for Non Destructive Testing*. 2011.

57. M.R. Clark, D.M.M., M.C. Forde, *Application of infrared thermography to the non-destructive testing of concrete and masonry bridges.* NDT&E International, 2003. **36**: p. 265-275.

58. Lu, Y., et al., *Concrete Pavement Service Condition Assessment Using Infrared Thermography.* 2017. **2017**.

59. Fan, C., F. Sun, and L. Yang. *Investigation on nondestructive evaluation of pipelines using infrared thermography*. in *Infrared and Millimeter Waves and 13th International Conference on Terahertz*

Electronics, 2005. IRMMW-THz 2005. The Joint 30th International Conference on. 2005. IEEE.

60. Fox, M., et al., *Time-lapse thermography for building defect detection.* 2015. **92**: p. 95-106.

61. Tewary, S., et al., *Detection of subsurface defects using active infrared thermography*. 2013.

62. Washer, G., et al., *Effects of environmental variables on infrared imaging of subsurface features of concrete bridges.* 2009. **2108**(1): p. 107-114.

63. Hiasa, S., et al. *Utilizing Infrared technologies as a non-destructive evaluation for maintenance of concrete structures*. in *Fourth International Symposium on Life-Cycle Civil Engineering, IALCCE*. 2014.

64. Washer, G. and P. Fuchs. *Developments in the use of infrared thermography for the condition assessment of concrete*. in *International Symposium Non-Destructive Testing in Civil Engineering*. 2015.

65. Sharma, G., et al., *Wavelet transform-based approach for processing ultrasonic B-scan images.* 2017. **59**(2): p. 93-99.

66. Kim, H. and H.J.E.S. Melhem, *Damage detection of structures by wavelet analysis.* 2004. **26**(3): p. 347-362.

67. Asare, S.K., et al. *Adaptive freeway incident detection algorithm using the Hilbert-Huang transform*. in *92nd Annual Meeting of the Transportation Research Board, Washington, DC*. 2013.

68. Sheng, Y., *Wavelet Transform in The Transforms and Applications Handbook. Alexander D. Poularikas, Ed*. 2000, Boca Raton, Fl.: CRC Press LLC.

69. Ibarra-Castanedo, C., et al., *On signal transforms applied to pulsed thermography*. Recent research developments in applied physics, 2006. **9**: p. 101-27.

70. Lonkar, G., et al. *Automatic Detection of Subsurface Defects Using Infrared Thermography*. in *AIP Conference Proceedings*. 2005. AIP.

71. Derraz, F., M. Beladgham, and M.h. Khelif. *Application of active contour models in medical image segmentation*. in *Information*

Technology: Coding and Computing, 2004. Proceedings. ITCC 2004. International Conference on. 2004. IEEE.

72. Okyere, A.-G. and N.J.T.R.R.J.o.t.T.R.B. Attoh-Okine, *Traffic sign recognition using sparse representations and active contour models.* 2014(2463): p. 35-45.

73. Li, S., Y. Cao, and H.J.J.o.C.i.C.E. Cai, *Automatic pavement-crack detection and segmentation based on steerable matched filtering and an active contour model.* 2017. **31**(5): p. 04017045.

74. Xu, C., A. Yezzi, and J.L. Prince. *On the relationship between parametric and geometric active contours*. in *Signals, Systems and Computers, 2000. Conference Record of the Thirty-Fourth Asilomar Conference on*. 2000. IEEE.

75. Li, C., et al. *Level set evolution without re-initialization: a new variational formulation*. in *Computer Vision and Pattern Recognition, 2005. CVPR 2005. IEEE Computer Society Conference on*. 2005. IEEE.

76. Madruga, F., et al., *Signal to noise ratio (SNR) comparison for lockin thermographic data processing methods in CFRP specimen.* Qirt10, Quantitative Infrared Thermography, Québec, 2010: p. 1-6.

77. Hidalgo-Gato García, R., et al., *Quantification by signal to noise ratio of active infrared thermography data processing techniques.* 2013.

78. Maldague, X., *Theory and practice of infrared technology for nondestructive testing.* 2001.

79. Maldague, X. and P.O. Moore, *Nondestructive testing handbook: infrared and thermal testing*. 2001: American society for nondestructive testing.

80. Al Gharawi, M., Y. Adu-Gyamfi, and G. Washer, *A framework for automated time-lapse thermography data processing.* Construction and Building Materials, 2019. **227**: p. 116507.

81. Vaghefi, K., *Infrared Thermography Enhancements for Concrete Bridge Evaluation.* Michigan Technological University, 2013.

82. Tran, Q.H., et al., *Effects of rebars on the detectability of subsurface defects in concrete bridges using square pulse thermography.* NDT & E International, 2018. **100**: p. 92-100.

83. ASTM, *Standard test method for detecting delaminations in bridge decks using infrared thermography*. 2007.

84. Huh, J., et al., *Experimental study on detection of deterioration in concrete using infrared thermography technique.* Advances in Materials Science and Engineering, 2016. **2016**.

85. Wysocka-Fotek, O., W. Oliferuk, and M. Maj, *Reconstruction of size and depth of simulated defects in austenitic steel plate using pulsed infrared thermography.* Infrared Physics & Technology, 2012. **55**(4): p. 363-367.

86. Ibarra Castanedo, C., *Quantitative subsurface defect evaluation by pulsed phase thermography: depth retrieval with the phase.* 2005.

87. Dumoulin, J., et al. *Evaluation of FRP gluing on concrete structures by active infrared thermography*. in *Proceedings of the QIRT*. 2010.

88. Arndt, R., C. Maierhofer, and M. Röllig, *Quantitative pulse-phase-thermography for masonry and concrete structures.* ECNDT, Berlin, Germany, 2006.

89. Ibarra-Castanedo, C., et al., *Active infrared thermography techniques for the nondestructive testing of materials*, in *Ultrasonic and advanced methods for nondestructive testing and material characterization*. 2007, World Scientific. p. 325-348.

90. Maierhofer, C., et al., *Quantitative impulse-thermography as non-destructive testing method in civil engineering–Experimental results and numerical simulations.* Construction and Building Materials, 2005. **19**(10): p. 731-737.

91. Meola, C., et al., *Application of infrared thermography and geophysical methods for defect detection in architectural structures.* Engineering Failure Analysis, 2005. **12**(6): p. 875-892.

92. Ibarra-Castanedo, C. and X. Maldague, *Pulsed phase thermography reviewed.* Quantitative Infrared Thermography Journal, 2004. **1**(1): p. 47-70.

93. Milovanović, B., I. Banjad Pečur, and N. Štirmer, *The methodology for defect quantification in concrete using ir thermography.* Journal of civil engineering and management, 2017. **23**(5): p. 573-582.

94. Ringermacher, H., et al., *Towards a flat-bottom hole standard for thermal imaging*, in *Review of Progress in Quantitative Nondestructive Evaluation*. 1998, Springer. p. 425-429.

95. Maldague, X.J.T.i.o.n.t., *Applications of infrared thermography in nondestructive evaluation.* 2000: p. 591-609.

96. Vavilov, V. and R. Taylor, *Theoretical and practical aspects of the thermal nondestructive testing of bonded structures.* Academic Press, Research Techniques in Nondestructive Testing, 1982. **5**: p. 239-279.

97. Lewis, C.D., *Demand Forecasting and Inventory Control: A Computer Aided Learning Approach*. 1997, Cambridge, UK: Woodhead Publishing Ltd.

98. Hiasa, S., R. Birgul, and F.N. Catbas, *Effect of defect size on subsurface defect detectability and defect depth estimation for concrete structures by infrared thermography.* Journal of Nondestructive Evaluation, 2017. **36**(3): p. 57.

99. Cheng, C. and Z. Shen, *Detecting Concrete Abnormality Using Time-series Thermal Imaging and Supervised Learning.* arXiv preprint arXiv:1804.05406, 2018.

100. Perez, H., J.H. Tah, and A. Mosavi, *Deep learning for detecting building defects using convolutional neural networks.* Sensors, 2019. **19**(16): p. 3556.

101. Ibarra-Castanedo, C., et al., *Comparative study of active thermography techniques for the nondestructive evaluation of honeycomb structures.* Research in Nondestructive Evaluation, 2009. **20**(1): p. 1-31.

102. contributors, E.P.G. *751.10 General Superstructure*. 22 April 2021 19:09 UTC; Available from: https://epg.modot.org/index.php?title=751.10_General_Superstructure&oldid=49228.

103. baron de Fourier, J.B.J., *Théorie analytique de la chaleur*. 1822: Firmin Didot.

104. Erwin, K., *Advanced Engineering Mathematics . Jhon Wiley & Sons.* Inc., New York, 1993: p. 1040-1043.

105. Karim, S.A.A., et al. *Wavelet Transform and Fast Fourier Transform for signal compression: A comparative study*. in *2011 International Conference on Electronic Devices, Systems and Applications (ICEDSA)*. 2011. IEEE.

106. Bracewell, R.N. and R.N. Bracewell, *The Fourier transform and its applications*. Vol. 31999. 1986: McGraw-Hill New York.

107. Maldague, X. and S. Marinetti, *Pulse phase infrared thermography.* Journal of applied physics, 1996. **79**(5): p. 2694-2698.

108. Hurwitz, J. and D. Kirsch, *Machine learning for dummies.* IBM Limited Edition, 2018. **75**.

109. Maldague, X., Y. Largouët, and J.-P. Couturier, *A study of defect depth using neural networks in pulsed phase thermography: modelling, noise, experiments.* Revue générale de thermique, 1998. **37**(8): p. 704-717.

110. Darabi, A. and X. Maldague, *Neural network based defect detection and depth estimation in TNDE.* Ndt & E International, 2002. **35**(3): p. 165-175.

111. Dudzik, S., *Two-stage neural algorithm for defect detection and characterization uses an active thermography.* Infrared Physics & Technology, 2015. **71**: p. 187-197.

112. Halloua, H., et al. *An intelligent method using neural networks for Depth detection by standard thermal contrast in active thermography*. in *Halloua, A. Elhassnaoui, A. Saifi, A. Obbadi, Y. Errami, S. Sahnoun//proc. 13th International Conference on Quantitative Infrared Thermography 2016, July 4-8, Gdansk, Poland (QIRT 2016).–Gdansk, Poland*. 2016.

113. Vapnik, V.N. and C. AY, *On a class of pattern-recognition learning algorithms.* Automation and Remote Control, 1965. **25**(6): p. 838-&.

114. Vapnik, V., *The nature of statistical learning theory springer New York google scholar.* New York, 1995.

115. Byun, H. and S.-W. Lee. *Applications of support vector machines for pattern recognition: A survey*. in *International Workshop on Support Vector Machines*. 2002. Springer.

116. Agarwal, V., *Ridge regression approach to color constancy.* 2005.

117. James, G., et al., *An introduction to statistical learning*. Vol. 112. 2013: Springer.

118. Lewis, C.D., *Industrial and business forecasting methods: A practical guide to exponential smoothing and curve fitting*. 1982: Butterworth-Heinemann.

Appendix A

The Fitting Diagrams of the Predictive Models

A-1 Two-week Training on Two-week Testing

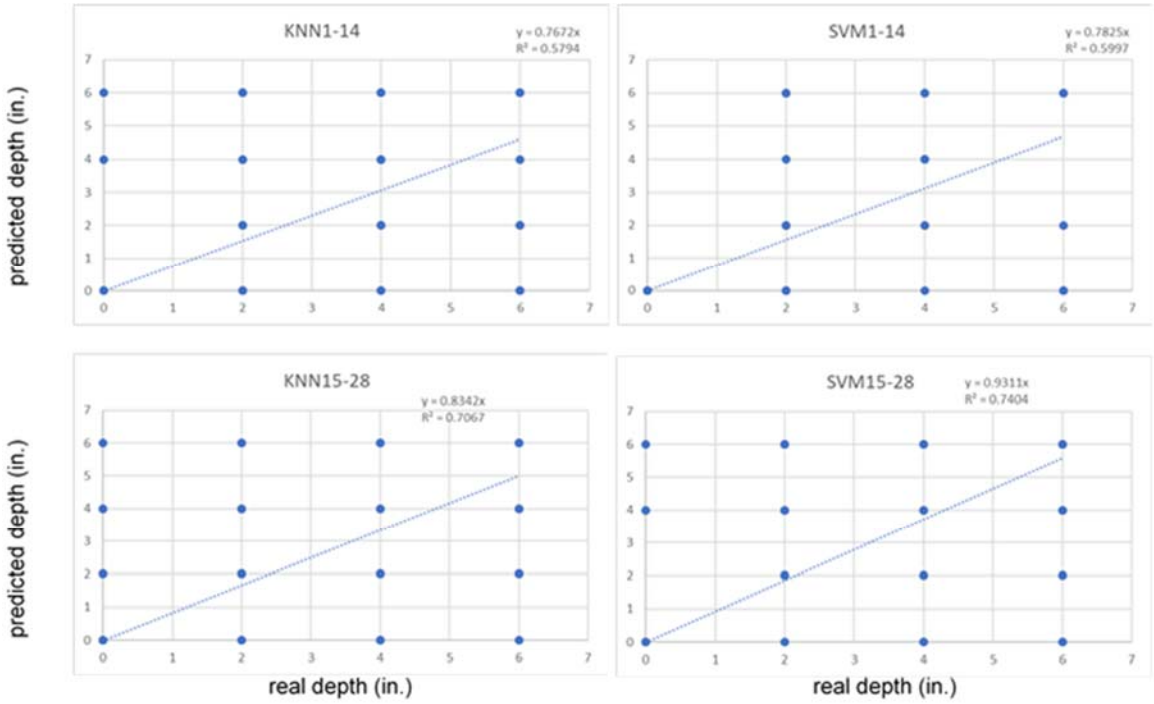

Figure A-1: Fitting diagrams for two-week training on two-week testing.

A-2 One-week Training on One-week Testing

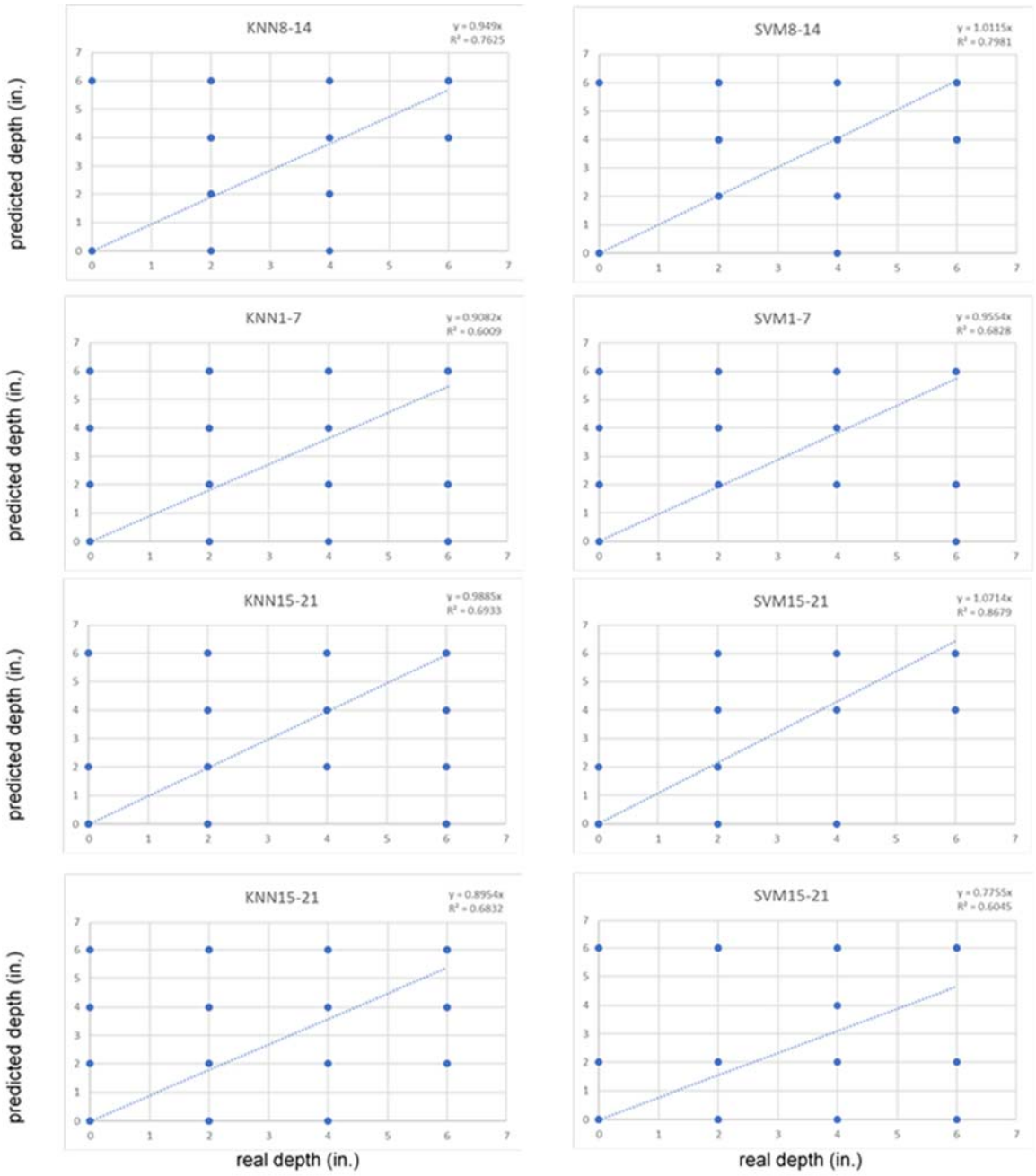

Figure A-2: Fitting diagrams for one-week training on one-week testing.

A-3 Three-day Training on Three-day Testing

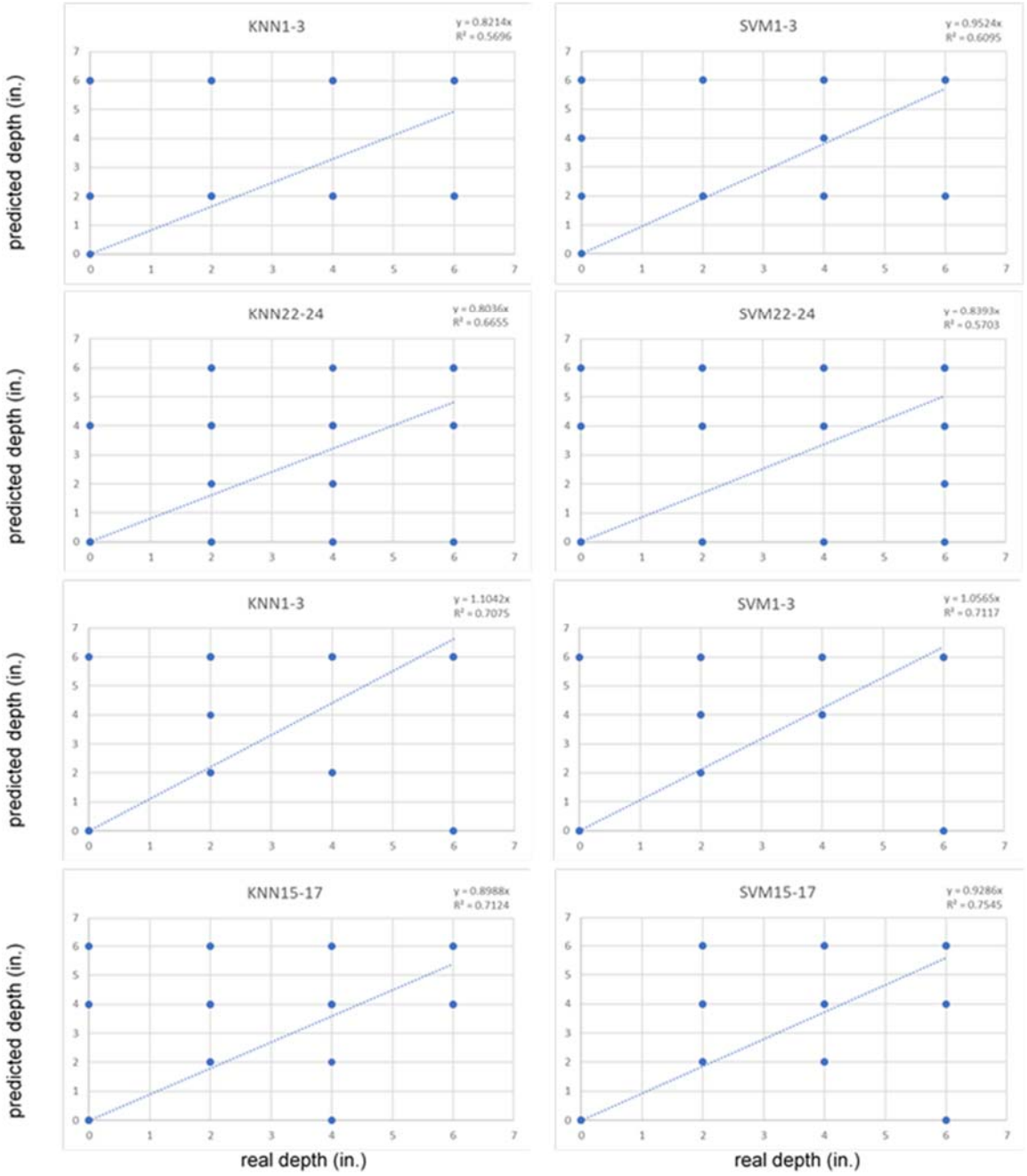

Figure A-3: Fitting diagrams for three-day training on three-day testing.

A-4 One-day Training on One-day Testing

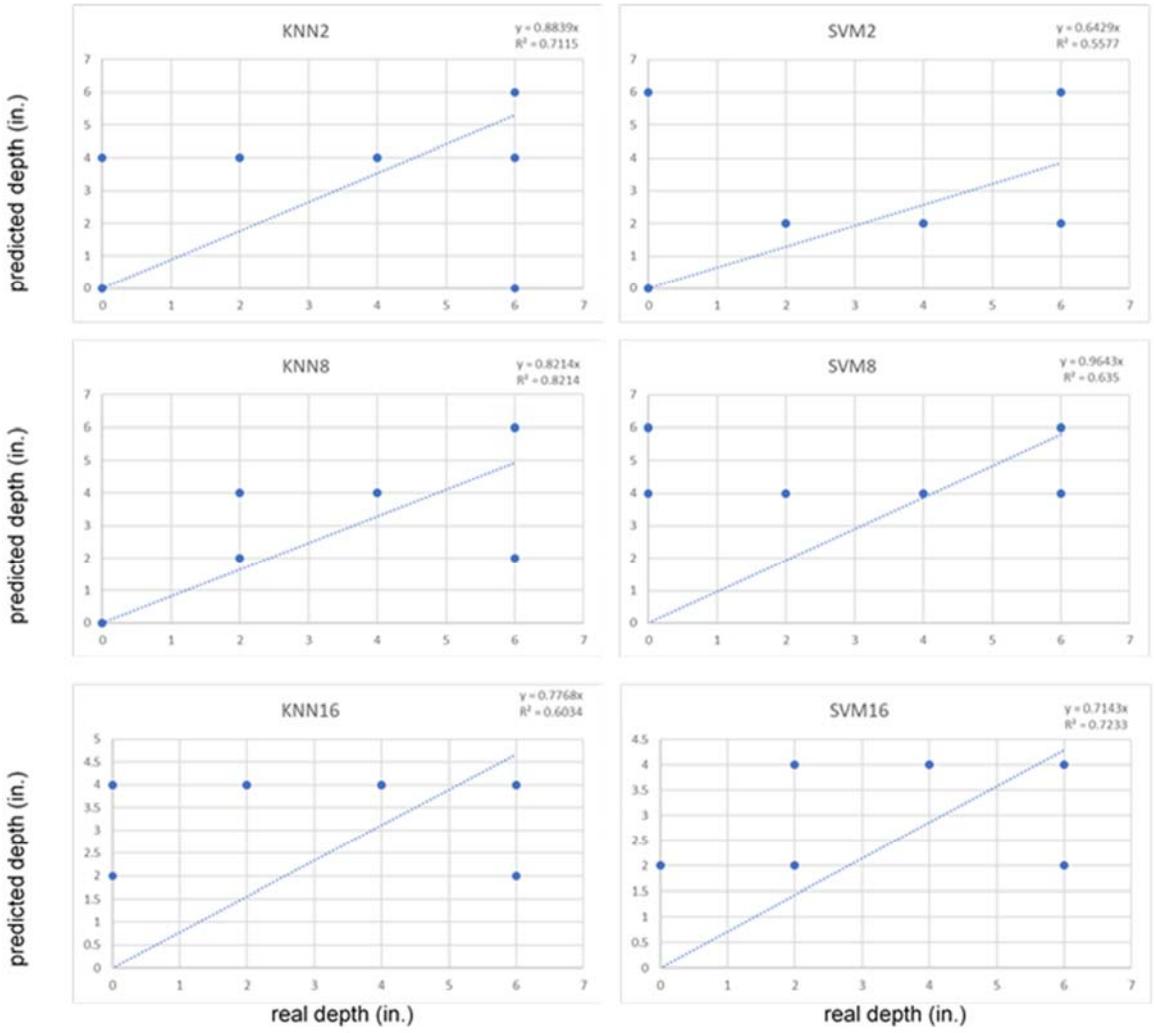

Figure A-4: Fitting diagrams for one-day training on one-day testing.

A-5 Three-week Training on One-week Testing

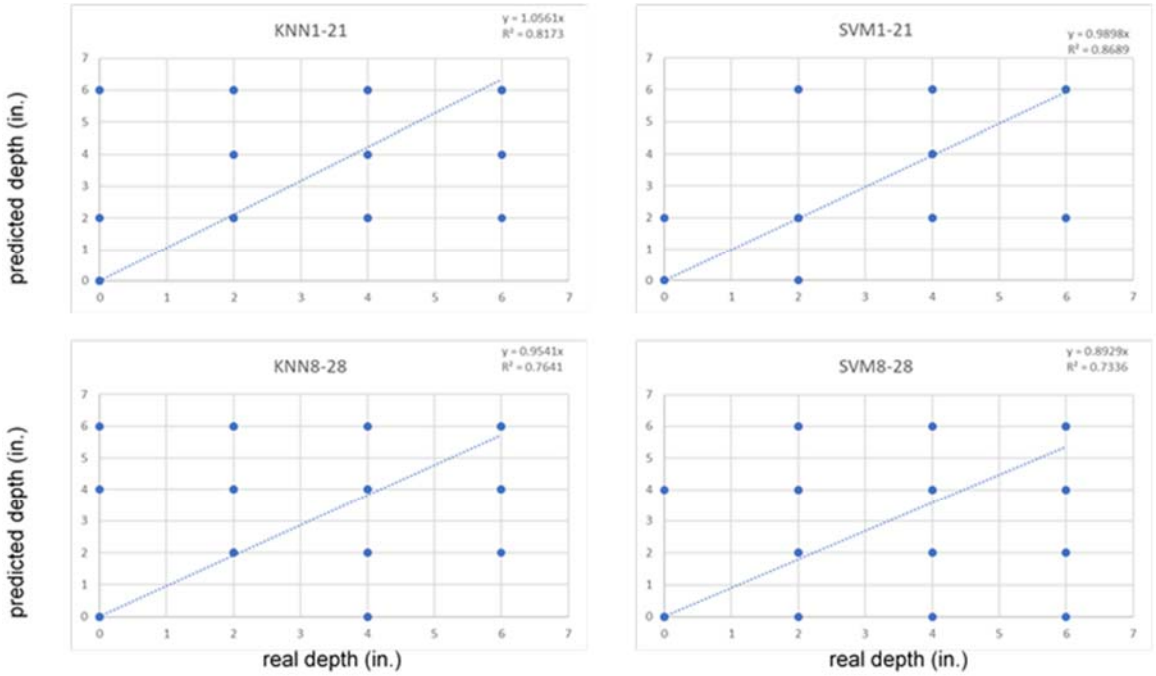

Figure A-5: Fitting diagrams for three-week training on one-week testing.

A-6 Two-week Training on One-week Testing

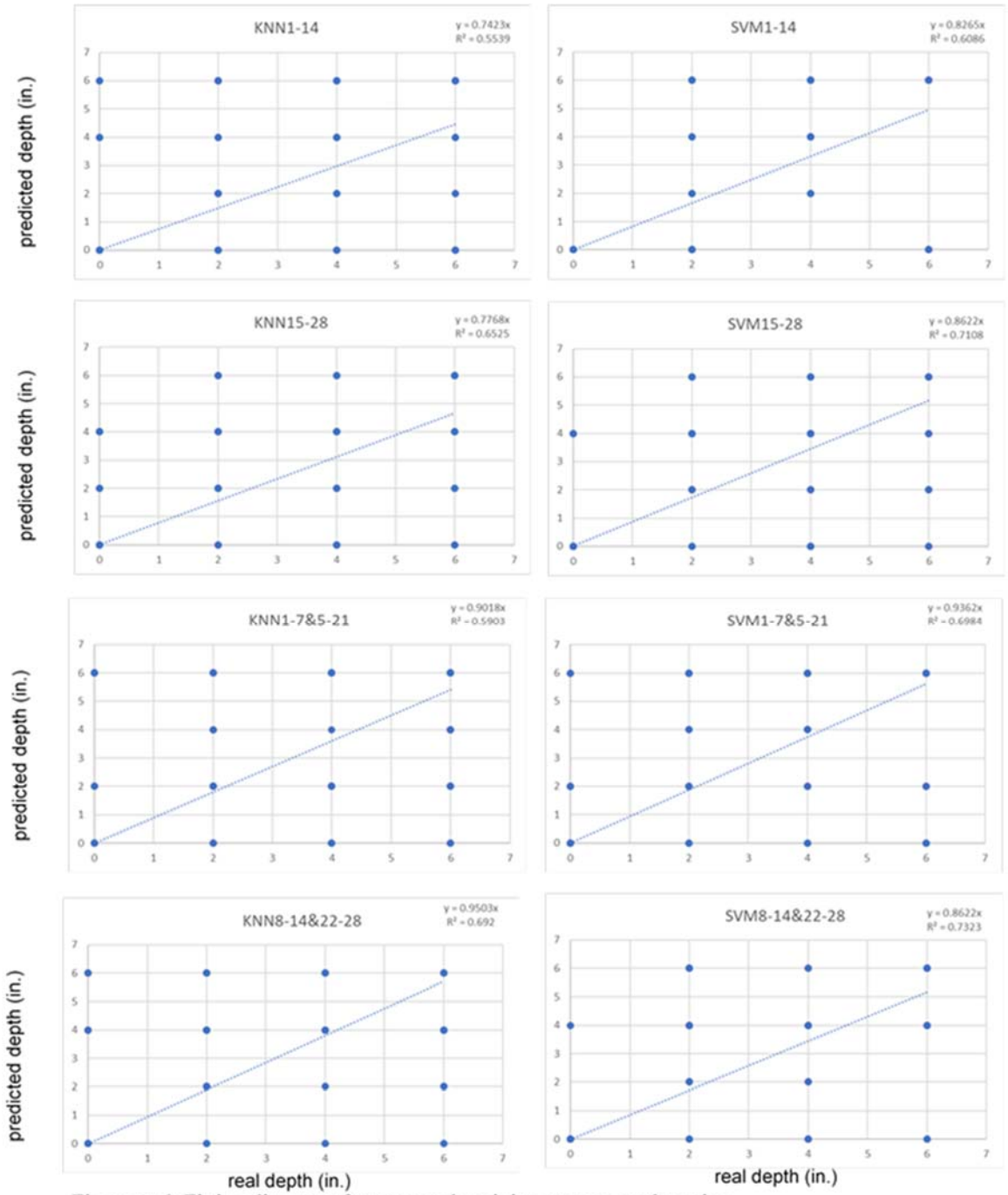

Figure A-6: Fitting diagrams for two-week training on one-week testing.

A-7 Three-week Training on Three-day and One-day Testing

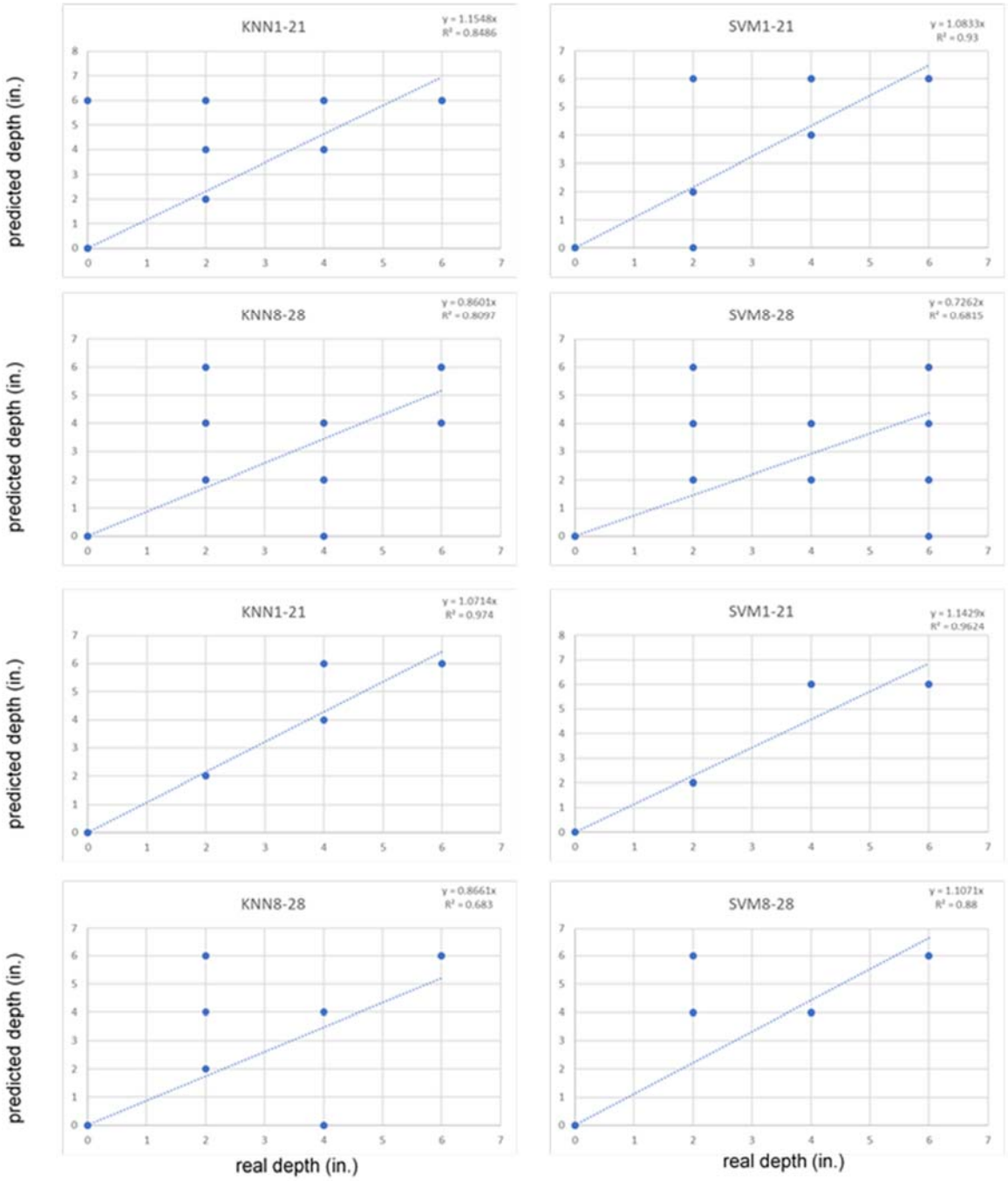

Figure A-7: Fitting diagrams for three-week training on three-day and one-day testing.

A-8 Two-week Training on Three-day Testing

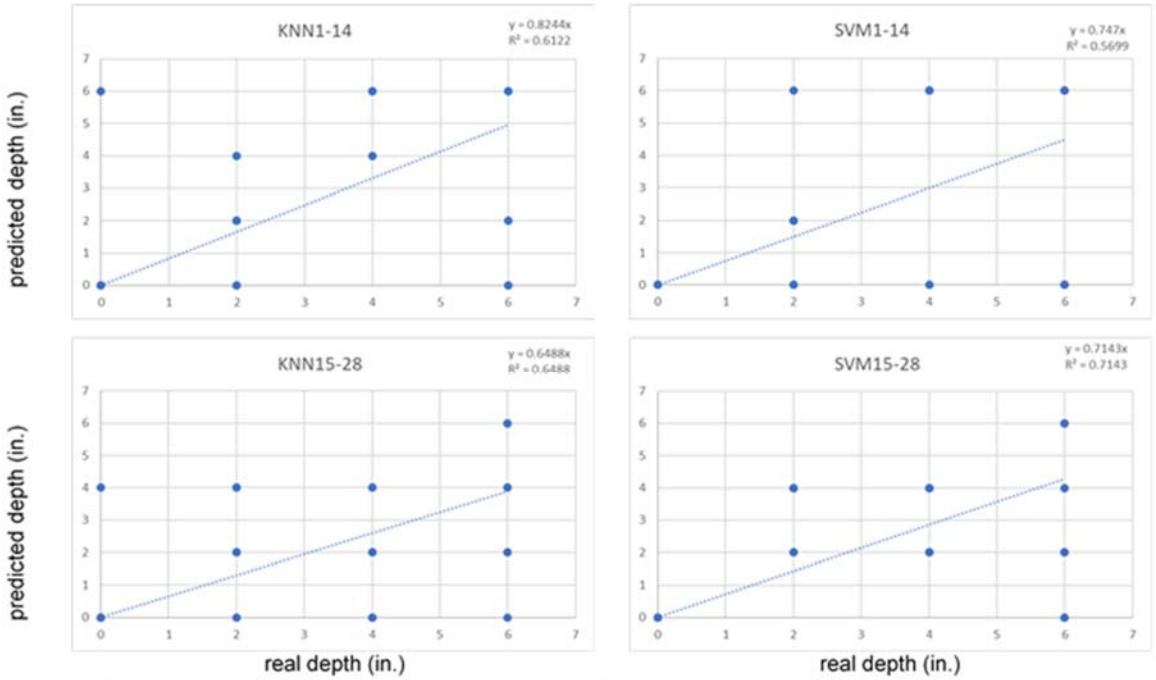

Figure A-8: Fitting diagrams for two-week training on three-day testing.

A-9 Two-week Training on One-day Testing

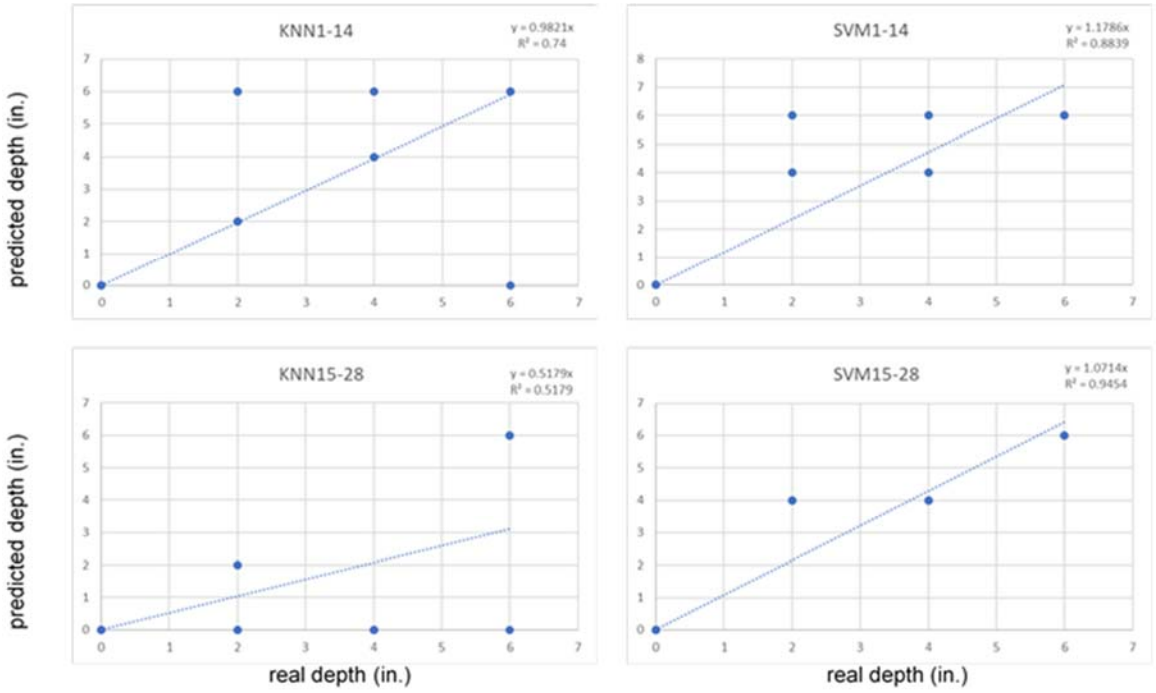

Figure A-9: Fitting diagrams for two-week training on one-day testing.

A-10 One-week Training on One-day Testing

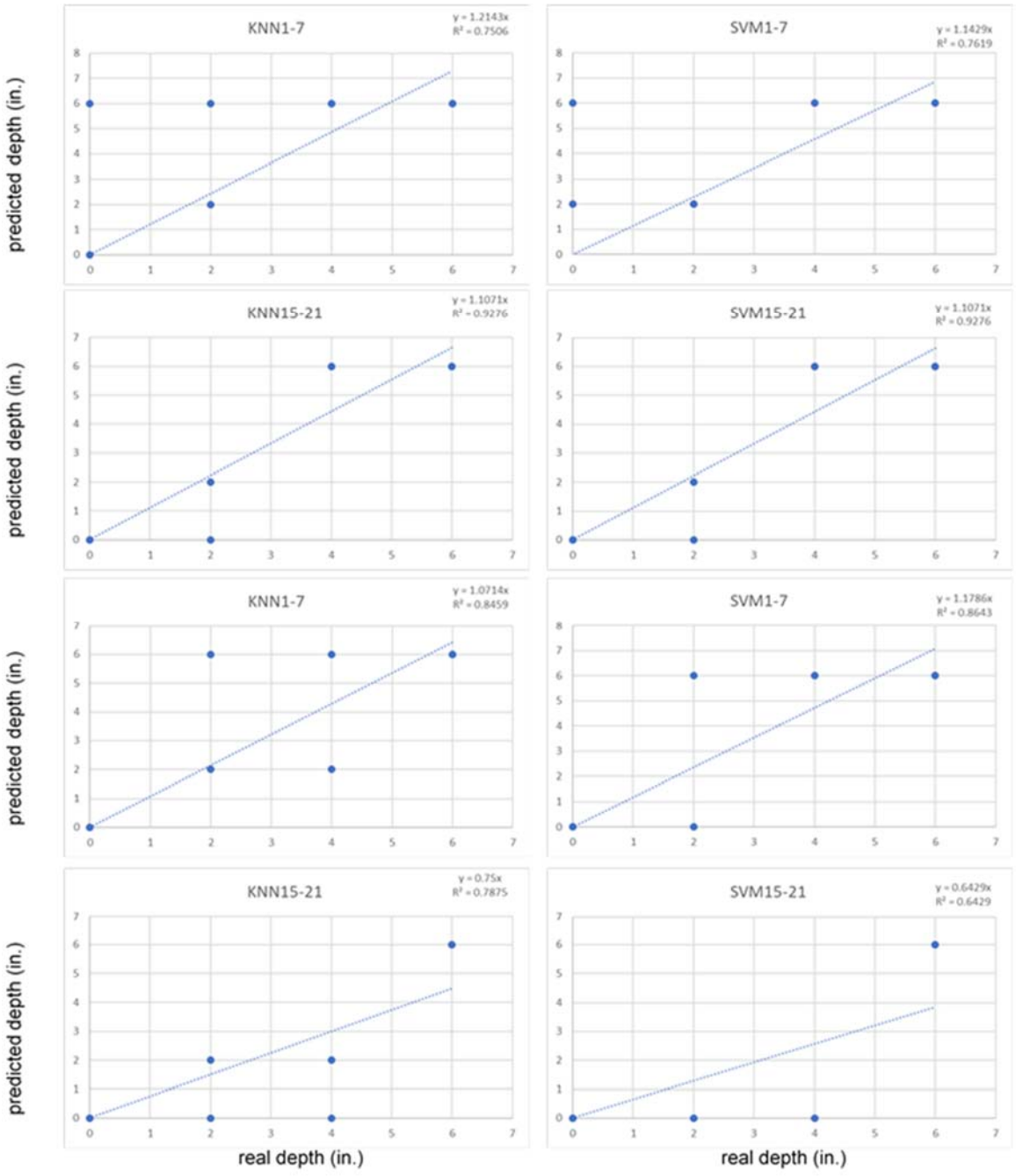

Figure A-10: Fitting diagrams for one-week training on one-day testing.

A-11 Three-day Training on One-day Testing

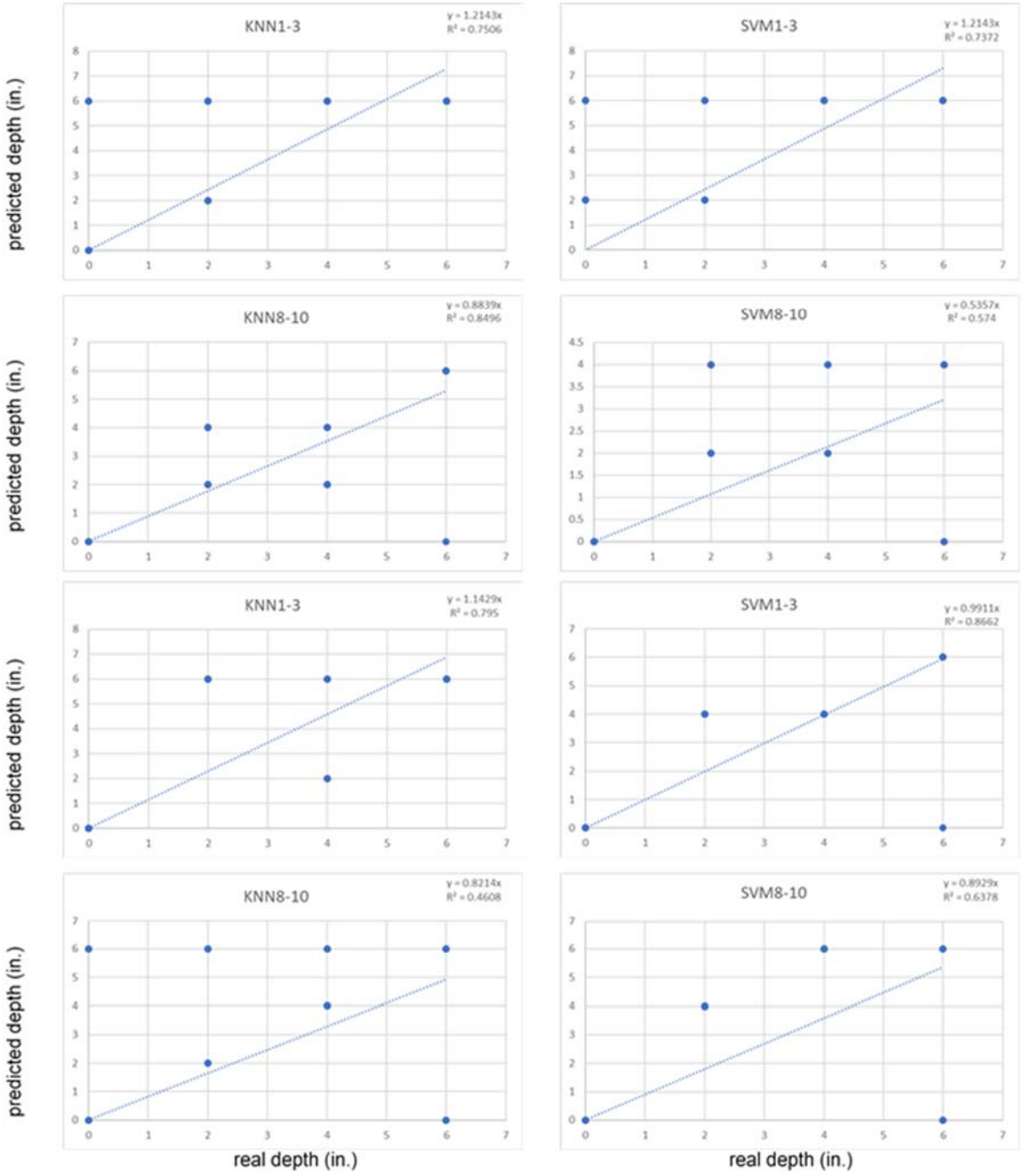

Figure A-11: Fitting diagrams for three-day training on one-day testing.

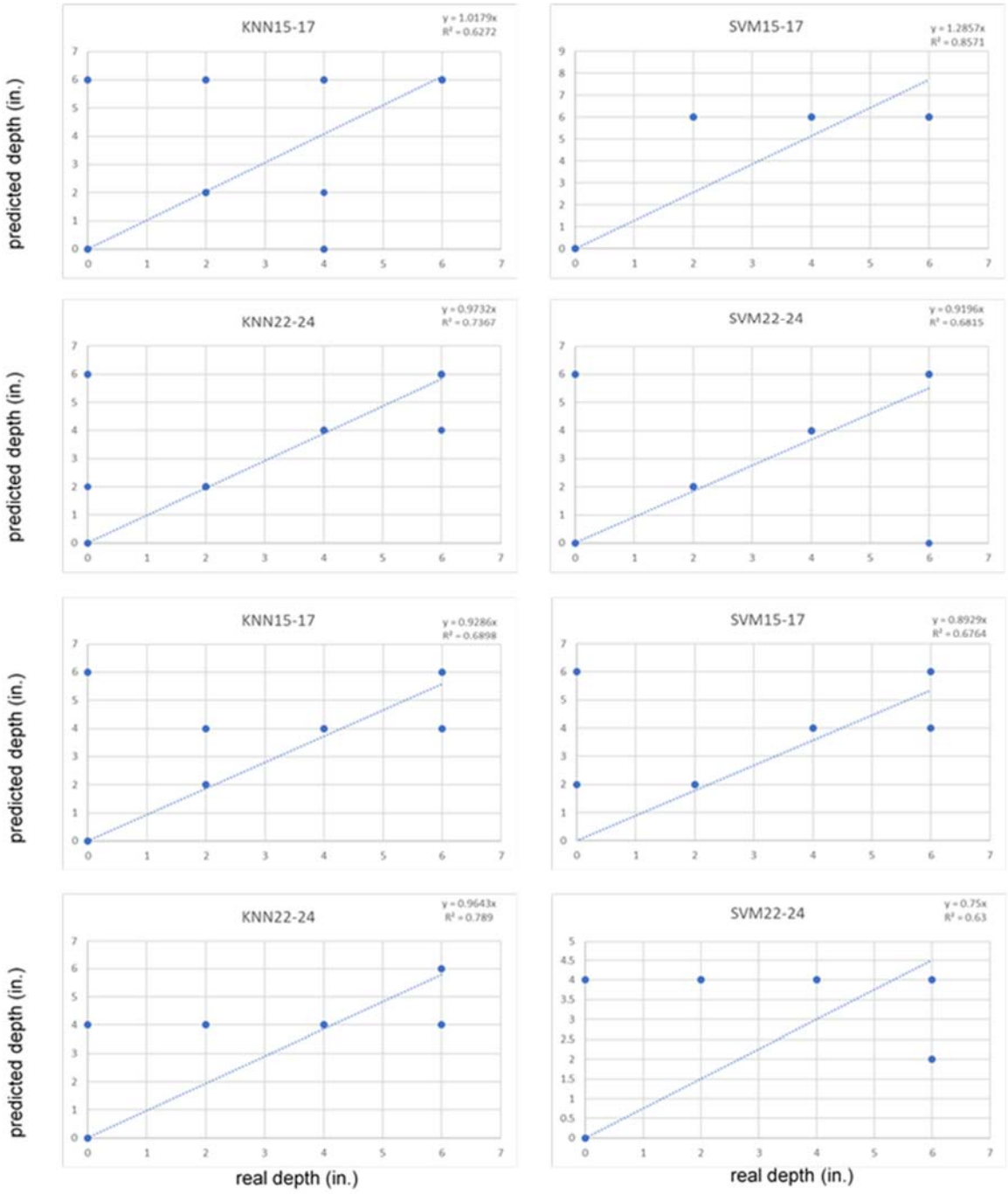

Figure A-11: Fitting diagrams for three-day training on one-day testing (continued).

Vita

Mohanned Al Gharawi was born in Baghdad, the capital of Iraq in 1978. He received his BSc. and MSc. degrees from University of Baghdad/Iraq in 2000 and 2004, respectively. In 2004, Al Gharawi started working as a structural engineer in the consulting engineering bureau (CEB) until 2014. In 2006, he joined University of Baghdad in Baghdad as one of the faculty members in the Department of Civil Engineering. Al Gharawi joined to the University of Missouri-Columbia in June 2014 for a PhD. program in Civil Engineering. He was a sponsored student by the Higher Committee of Education Development in Iraq (HCED).